

UCSF

UC San Francisco Electronic Theses and Dissertations

Title

Development of multi-parametric, high field magnetic resonance imaging techniques for improved characterization of prostate cancer

Permalink

<https://escholarship.org/uc/item/7f85799p>

Author

Chen, Albert

Publication Date

2006

Peer reviewed|Thesis/dissertation

**Development of multi-parametric, high field magnetic resonance imaging
techniques for improved characterization of prostate cancer**

by

Albert Chen

DISSERTATION

Submitted in partial satisfaction of the requirements for the degree of

DOCTOR OF PHILOSOPHY

in

Bioengineering

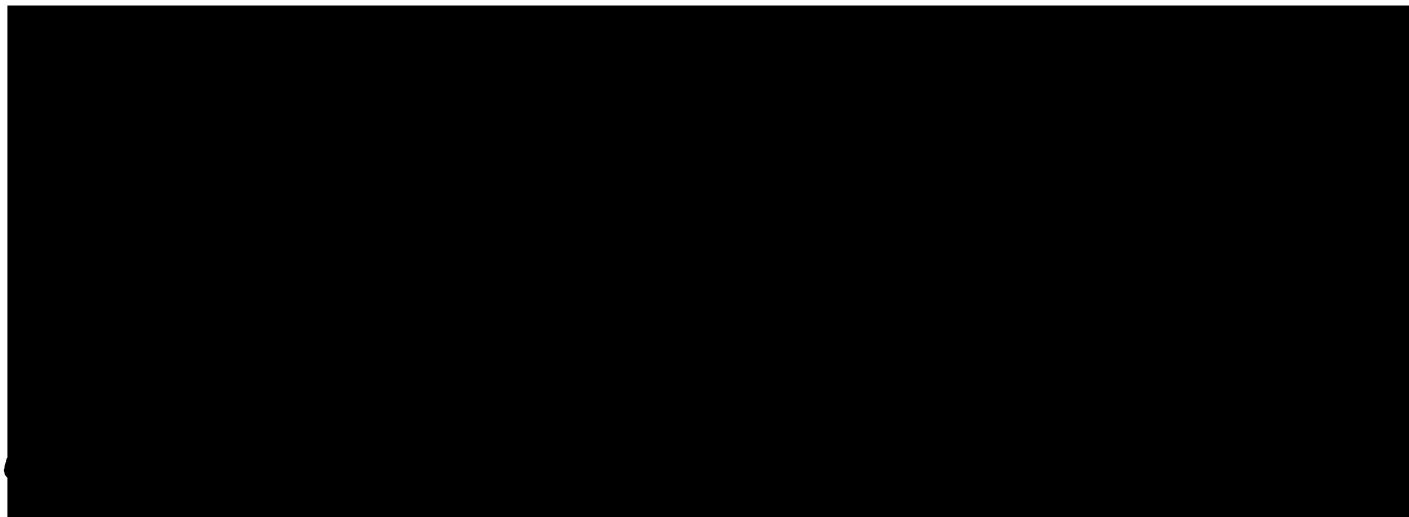
in the

GRADUATION DIVISION

of the

UNIVERSITY OF CALIFORNIA, SAN FRANCISCO

UCSF LIBRARY



Date

University Librarian

Degree Conferred:

This manuscript is dedicated to:

My grandmother.

I would like to acknowledge the following people for make this project possible:

Dr. Charles Cunningham for his work on pulse sequence design and sharing his unbounded knowledge and expertise in MR with me.

Dr. Duan Xu for hand holding me through basics of MR and his relentless support.

Dr. John Kurhanewicz and members his research group for supports on all the prostate cancer patient exams.

Dr. Sarah Nelson and members of her research group for make all the data processing and visualization performed in this project possible.

Niles Bruce for his help in patient data acquisition,

Past and present Members of the Vigneron group for their help on hardware and software development in this project and basically tolerating me over the years.

My advisor Dan Vigneron for letting be part of this research and his generous help and support through last five years.

UCSF LIBRARY

Development of multi-parametric, high field magnetic resonance imaging techniques for improved characterization of prostate cancer

by

Albert Chen

Abstract:

Management of prostate cancer is a difficult task for both patients and clinicians because of the broad range of biologic malignancy and the broad spectrum of treatment approaches. Accurate radiological assessments are required for therapeutic selection and guidance, following patients on watchful waiting, monitoring treatment response in individual patients and for clinical trials of emerging therapies. In this bioengineering study, magnetic resonance (MR) techniques for metabolic and morphological assessments were developed and optimized specifically for prostate cancer and higher field (3T) to improve the non-invasive characterization of the disease.

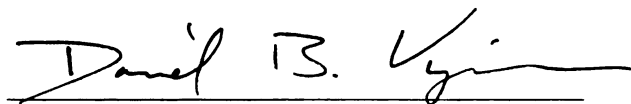
At 3T, issues such as the J-modulation changes for citrate resonance at higher field, more severe magnetic susceptibility induced magnetic field inhomogeneities, and increased chemical shift mis-registration make robust acquisition and analysis of multi-parametric prostate MR data challenging. In this work, 3T prostate MR coils were developed and MR imaging sequences were optimized for acquisition of high-resolution anatomical images of the prostate. A new MLEV-Point RESolved Spectroscopy (MLEV-PRESS) sequence was developed to allow acquisition of up-right citrate resonance at 3T. High

UCSF LIBRARY

resolution (0.157cc) MR spectroscopic imaging (MRSI) data were acquired at 3T and the theoretical 2-fold increase in SNR over 1.5T was demonstrated. To reduce the scan time of MRSI to allow acquisition of other MR modality during one clinical exam, a new, fast and robust MRSI acquisition utilizing flyback echo-planar readout trajectories was also developed. High quality data were demonstrated within half of the scan time required for conventional MRSI acquisition. For acquisition of prostate MR data based on movement of water and tissue micro-environment to reflect morphological changes in prostate cancer, single-shot fast spin-echo diffusion tensor imaging (SSFSE-DTI) sequence and magnetization prepared sequence with multi-slice spiral imaging for were optimized for prostate DTI and T2 relaxation parameter mapping. Significantly different diffusion and T2 relaxation parameters were observed in regions of prostate cancer as compared to normal prostate peripheral zone.

The multi-parametric approach of acquiring different and unique MR data to characterize prostate cancer developed in this work may increase the usefulness and significance of MR prostate exam for the clinical management of prostate cancer.

Dissertation Committee Chair

A handwritten signature in black ink, reading "Daniel B. Vigneron", is written over a horizontal line.

Dr. Daniel B. Vigneron

UICCT LIBRARY

Dedication and acknowledgement	iii
Abstract	iv
List of Tables	x
List of Figures	xi
Chapter 1: Introduction	1
A) Motivation	1
B) Aims	1
Chapter 2: Background	3
A) Prostate cancer and patient population	3
a. Anatomy of normal human prostate	3
b. Anatomy of pathological prostate	4
c. Patient population	6
B) Nuclear spin and magnetic resonance	6
C) Magnetic resonance imaging	7
a. Spin-Echo	8
b. Fast Spin-Echo	9
c. MRI of the prostate cancer at 1.5T	10
D) Magnetic resonance spectroscopy	10
a. Point RESolved Spectroscopy (PRESS)	11
b. Multi-Nuclear Spectroscopy (MNS)	12
c. MRSI studies of prostate cancer at 1.5T	12
E) Diffusion tensor imaging	16
a. Diffusion of water	16
b. MR signal and diffusion	17
c. Single Shot Fast Spin Echo diffusion	18
d. Echo-planar diffusion	19
F) Relaxation time measurements	20

IICSE LIBRARY

a. T1 relaxation time	20
b. T2 relaxation time	21
Chapter 3: 3T MRI of Prostate Cancer	23
A) 3T hardware development for prostate imaging	23
a. rigid coil	23
b. Pelvic phase array	25
c. Dual-tuned coil	26
B) Imaging of prostate cancer at 3T	28
a. High resolution T2-weighted FSE at 3T	28
Chapter 4: MRSI of prostate cancer at 3T	32
A) Challenges for prostate MRSI at 3T	33
a. J-modulation changes of citrate resonance	33
b. Other considerations	35
B) Sequence design for prostate MRSI at 3T	36
a. Theory and simulations	36
b. MLEV-PRESS sequence and spectral-spatial refocusing pulses ...	38
C) MRSI of prostate cancer at 3T	42
a. Patient population	42
b. 3T MRI/MRSI protocol	43
c. T1 measurements	45
d. Data analysis	45
e. Results	47
f. Discussions	51
Chapter 5: High Speed Prostate MRSI at 3T with Flyback Echo-Planar Encoding	56

IICSE LIBRARY

A) Considerations for fast prostate MRSI acquisition	56
B) Trajectories designs and SNR efficiency for 3T prostate MRSI	57
C) High speed MRSI of prostate with flyback echo-planar encoding	60
a. MRI/MRSI protocols	60
b. Data analysis	62
c. Results	63
d. Discussions	66
Chapter 6: Diffusion tensor imaging of prostate cancer	68
A) DTI of the prostate with DTI-SSFSE and DTI-EPI sequence	68
B) Diffusion tensor imaging studies of untreated prostate cancer patients.....	70
a. Hypothesis	70
b. MRI/MRSI/DTI protocol	71
c. Data analysis	72
d. Results and Discussions	73
C) Diffusion tensor imaging studies of post-therapy prostate cancer patients .	76
a. MRI/MRSI/DTI protocol	77
b. Results	78
c. Discussion	79
Chapter 7: T2 mapping of the prostate	81
A) Pulse sequence for accurate T2 mapping.....	81
B) Characterization of prostate cancer with T2 mapping	83
a. MRI/MRSI/DTI/T2-mapping protocol	83
b. Results	84
c. Discussion	86
Chapter 8: Summary	89

IICSE LIBRARY

List of Tables:

Table 1. SNR comparison between flyback echo-planar readout and conventional phase encoding. 65

Table 2. Diffusion and MRS data of Untreated Prostate Cancer Patients. 74

UICSE LIBRARY

List of Figures:

Figure 1. Sagittal view of the normal prostate and its zonal anatomy. 3

Figure 2. Dr. Gleason’s illustration of the five different grades of prostate cancer. ... 5

Figure 3. Spin echo schematic showing echo generation at TE after 90 and 180
RF pulse. 8

Figure 4. Axial T2-weighted MRI of the prostate. 9

Figure 5. Pulse sequence timing diagram for PRESS. 11

Figure 6. MRSI data from prostate at 1.5T. 14

Figure 7. Spin-echo diffusion preparation. 17

Figure 8. Sequence timing diagram for SSFSE diffusion sequence. 19

Figure 9. Pulse sequence timing diagram for EPI diffusion sequence. 20

Figure 10. T1 relaxation curve. 21

Figure 11. T2 relaxation curve. 22

Figure 12. Simulation used for design of the rigid coil for prostate MRI and the
finished single element probe. 24

Figure 13. Oblique axial (left) and oblique coronal (right) T2-weighted FSE images
acquired from a prostate cancer patient using the custom built single element
endorectal coil. 25

UICSE LIBRARY

Figure 14. The internal circuitry of the concentric coplanar dual-tuned prostate probe.	26
Figure 15. Oblique axial (left) and oblique coronal (right) T2-weighted fast spin-echo images of the human prostate acquired using the coplanar $^1\text{H}/^{31}\text{P}$ dual-tuned endorectal coil.	27
Figure 16. Non-localized ^{31}P spectra acquired from human prostate in vivo using the coplanar dual-tuned endorectal coil.	28
Figure 17. Prostate cancer patient imaged at both 3T and 1.5T using Medrad endorectal coil.	29
Figure 18. Oblique coronal T2-weighted FSE images acquired at 3T. Oblique axial T2-weighted FSE images acquired at 3T.	30
Figure 19. Chemical structure of the citrate molecule.	33
Figure 20. TE dependence of the phase and amplitude modulation of the citrate resonance at 3T.	34
Figure 21. The effect of J-modulation on the appearance of the citrate spectrum at 3T with the conventional PRESS sequence.	35
Figure 22. Pulse timing diagram of the new 3T prostate MRSI sequence.	38
Figure 23. Design of the short spectral-spatial refocusing pulses.	39
Figure 24. Results from phantom experiment using the new pulse sequence.	41

IICSE LIBRARY
 IICSE LIBRARY

Figure 25. MRSI data acquired at 3T with both a) conventional PRESS sequence and b) the MLEV-PRESS sequence. 46

Figure 26. MRSI data obtained from a sixty-eight years old prostate cancer patient with biopsy confirm cancer in right (3+3) and left (3+3) gland who underwent prostate MRI/MRSI exam at both 3T (a) and 1.5T (b). 47

Figure 27: MRSI data obtained from a seventy-one year old prostate cancer patient with biopsy proven cancer in the right gland (2+2) who underwent MRI/MRSI exams at both 3T (a) and 1.5T (b). 49

Figure 28. Sixty-five year old prostate cancer patient with biopsy confirmed prostate cancer (right lobe, G3+3). Elevated choline and reduced citrate were observed in the region of positive biopsy (b) for prostate cancer and that was suspicious for abnormality on the T2-weighted FSE images (a). 50

Figure 29. Flyback echo-planar readout trajectory designed for high speed prostate MRSI with high spatial and spectral resolution. The trajectory is designed for 976 spectral bandwidth, 4.9 mm minimum spatial resolution and SNR efficiency of 71%. 58

Figure 30. Flyback Echo-Planar gradient waveform designed for high speed MRSI acquisition with 5mm minimum spatial resolution and high efficiency (92%). 59

Figure 31. 3D-MRSI data were acquired with MLEV-PRESS sequence with both flyback echo-planar readout trajectory (b) and conventional phase encode (c) from a seventy-three year old prostate cancer patient with biopsy confirmed cancer at unspecified location (G3+3). 63

Figure 32. 3D MRSI data was acquired with MLEV-PRESS sequence with the flyback echo-planar trajectory shown in figure 30 from a sixty-one year old prostate cancer patient with biopsy confirmed cancer in the left gland (G2+3, 2mm). 64

IUCSF LIBRARY

Figure 33. Comparison of conventional FSE images (left) with $\langle D \rangle$ (mean diffusivity) images acquired with DTI-SSFSE (middle) and DTI-EPI (right). 69

Figure 34. H&E staining patterns of excised prostate tissue samples. 70

Figure 35. In this untreated patient, a large region of cancer was confirmed by biopsy and seen as an area of reduced $\langle D \rangle$ and elevated FA as compared to healthy peripheral zone. FA in stromal regions of the central gland was even higher than for the cancer. 75

Figure 36. Detection of reduced $\langle D \rangle$ in the region of biopsy-confirmed cancer corresponded with reduced FSE-T2 signal intensity and elevated choline, reduced citrate on MRSI. 76

Figure 37. T2-weighted MRI (left) and $\langle D \rangle$ map (right) following hormone ablation therapy. 78

Figure 38. T2-weighted MRI (left) and $\langle D \rangle$ map (right) following brachy therapy. . 79

Figure 39. Post radiation therapy patient with residual/recurrent cancer. MRSI and DTI demonstrated elevated choline and reduced $\langle D \rangle$ 80

Figure 40. The T2 preparation portion of the pulse sequence. 82

Figure 41. The spectral-spatial pulse (shown as rf4) and the 2D spiral readout implemented after the T2-preparation sequence. 83

Figure 42. T2-weighted MRI, MRSI, DTI and T2-mapping data obtained from Sixty-one year old prostate cancer patient with biopsy proven cancer (G3+3, Left lobe). 85

IUCSF LIBRARY

Figure 43. Scatterplot shows the distribution of the $\langle D \rangle$ values and T2 relaxation times 86

UICSF LIBRARY

Chapter 1: Introduction

A) Motivation:

According to the estimates done by American Cancer Society, 232,090 men were diagnosed with and 30,350 men died of cancer of the prostate in 2005 [1] . This made prostate cancer the most common cancer, excluding skin cancer, and the second leading cause of cancer related death in men in United States. Thousands of prostate cancer patients are being identified at an earlier stage of the disease due to increased screening using prostate specific antigen (PSA) and transrectal ultrasound (TRUS) guided biopsy [2]. Managing the disease has been a difficult task for both patients and clinicians because of the broad range of biologic malignancy and is treated with a broad spectrum of approaches from "watchful waiting" and hormone deprivation therapy to aggressive surgical, radiation, and cryosurgical therapies [3, 4]. Current diagnostic tools such as digital rectal exams (DRE), PSA and biopsy are limited in characterizing the location and the extent of the disease as well as in detecting metastases. Accurate radiological assessments are required for therapeutic selection, guidance of local therapies, following patients on watchful waiting and monitoring treatment response in individual patients and very importantly for clinical trials of emerging therapies.

B) Aims:

Recently, new MR metabolic, perfusion and diffusion techniques have been investigated to address this need [5-7]. Most of these studies have been limited by the performance of

UCSF LIBRARY

the conventional 1.5 Tesla (T) MR system and sub-optimal techniques for prostate cancer imaging. In addition to conventional anatomical images, metabolic, structural and morphological information may be acquired in a single exam to allow a more complete assessment of prostate cancer. By developing and optimizing these MR technique specifically for prostate cancer and the higher field system (3T) that are becoming available in the clinical settings, noninvasive characterization of prostate cancer may be dramatically improved. The goal of this bioengineering thesis project was to develop and apply new methods in each of the following areas:

- High field MR imaging of the prostate for better anatomical assessment.
- Development of high field, high resolution MR spectroscopic imaging (MRSI) of prostate cancer to improve signal to noise ratio (SNR) and robust quantitation of prostate metabolites.
- Development of fast k-space sampling technique to allow high speed MRSI of prostate cancer.
- Optimizing Diffusion tensor imaging technique for quantitative assessment of water micro-environment of prostate cancer.
- Optimizing fast transverse relaxation time (T2) measurement sequence for characterizing prostate cancer.

UICSE LIBRARY

Chapter 2: Background

A) Prostate cancer and patient population:

a. Anatomy of normal human prostate

The prostate is an exocrine gland shaped similarly to a chestnut that surrounds the urethra between the bladder neck and genitourinary membrane. The ejaculatory ducts pass through the gland to enter the prostatic urethra at the verumontanum (Figure 1) [8]. The normal adult gland is about the size of a walnut. It functions as an accessory sex gland and contributes approximately 0.5 ml to the normal ejaculate volume of 3.5 ml. The prostate secretions are related to semen gelation, coagulation and liquefaction.

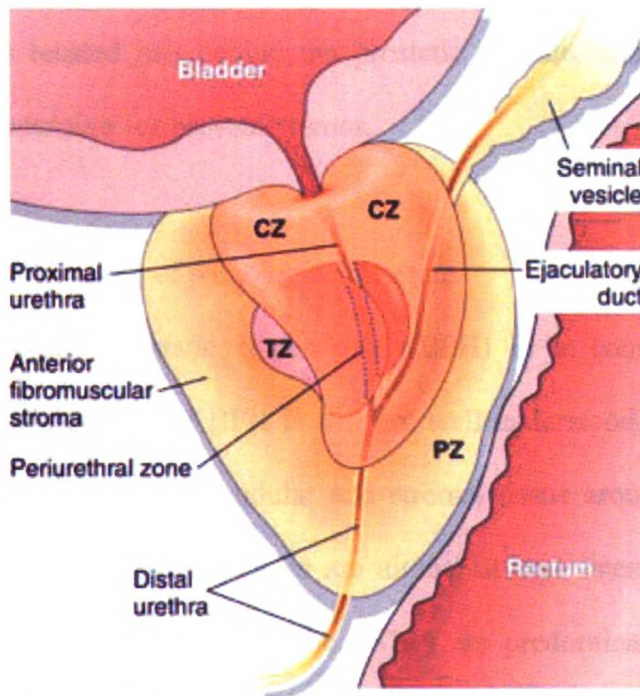


Figure 1. Sagittal view of the normal prostate and its zonal anatomy [8].

The prostate can be separated into glandular and non-glandular components. The non-glandular parts include the prostatic urethra and the anterior fibromuscular stroma. The glandular prostate includes periurethral zone, central zone, transition zone and the peripheral zone. These prostatic zones can be differentiated by their location as well as the morphology

of its glandular epithelial-covered ductal systems. It is in these ducts where the prostate secretions are collected. In peripheral zone and transition zone, the ducts are narrow and terminate in small round, simple, acini. In central zone the acini are larger and have irregular contours. The periurethral ducts arise along proximal urethra and are confined to periurethral stroma.

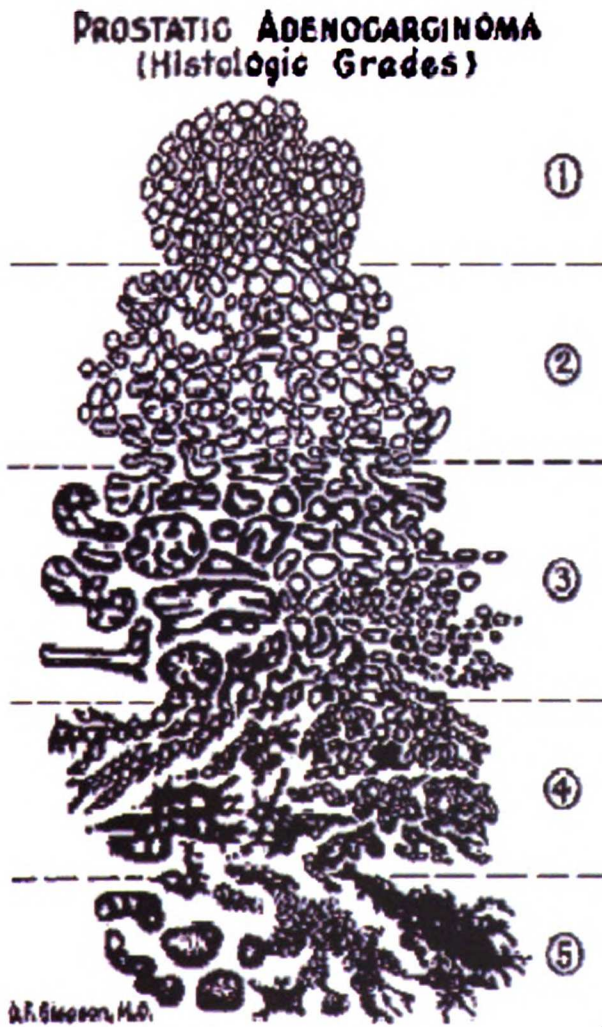
Surrounding the prostate is a thick layer of fibromuscular tissue. This prostatic capsule lies between the glandular prostate and connective tissues. And these connective tissues separate the prostate gland anteriorly from the symphysis pubis, posteriorly from the rectum, and inferiorly from the genitourinary membrane. The neurovascular bundles and the muscles of the pelvic floor border the prostate laterally. The neurovascular bundle is the combination of lateral venous plexus, arteries and nerves. The neurovascular bundle is located just behind the prostatic capsule, and is the common site of extracapsular extension for prostatic tumor.

b. Anatomy of pathological prostate

Benign prostatic hyperplasia (BPH) is a common condition as a man age. The pathogenesis of BPH is still not well understood. BPH is characterized by progressive hyperplasia of glandular and stromal tissue around the urethra. The largest and most numerous BPH nodules are almost always laterally situated and arise almost entirely within the transition zone. They are predominantly glandular and are responsible for most clinical cases of BPH. The nodules may cause lower urinary tract symptoms (LUTS) such as obstruction and irritations.

UICSE LIBRARY

The prostate peripheral zone is sometimes afflicted by chronic inflammatory process and may result in tissue atrophy and scarring. More importantly, prostate cancer almost always originated from the prostate peripheral zone. Prostate carcinomas are usually well differentiated architecturally and most remain small in size and are clinically indolent. As the cancer progresses in some cases to become clinically significant disease, it losses differentiation progressively, become larger in size, and is likely to metastasize and cause death.



The most commonly used system for prostate tumor grading is the Gleason grading system [9]. In this system, the glandular architecture of the prostatic tissue under the microscope is used for grading. The appearances of the five different grades are illustrated in Figure 2 [10]. Pathologists assign a primary grade to the pattern of the cancer that is most commonly observed and a secondary grade to a pattern of the cancer that is second most commonly observed grade in the specimen. The Gleason score is obtained by adding the primary and

Figure 2. Dr. Gleason's illustration of the five different grades of prostate cancer.

secondary grades together. Since the Gleason grade range from 1 to 5, Gleason score thus range from 2 to 10. Well differentiated tumors have a Gleason score of 2 to 4, moderately differentiated tumors have a Gleason score of 5 to 6 and poorly differentiated tumors have a Gleason score of 8 to 10. Tumors with Gleason score of 7 are sometimes grouped with moderately differentiated tumor and are sometimes grouped with poorly differentiated tumors.

c. Patient population

All patient studies in this thesis project were conducted with CHR (Committee on Human Research, UCSF) approval. The prostate cancer patients had either biopsy proven prostate cancer or are suspected to have prostate cancer based on elevated PSA. Each subject was asked to sign the UCSF research subject informed consent explaining the study design, procedures, risks and benefits and received a copy of the patients bill of rights. The data handling in all studies followed the health insurance portability and accountability act (HIPAA) and UCSF guidelines.

B) Nuclear spin and magnetic resonance

MRI uses the properties of the atom in its chemical and magnetic environment to offer information of the increasingly larger components such as molecules, tissues, and organs. The nuclear species with multiple of $\frac{1}{2}$ nuclear spin, which means nuclei with unpaired protons, can be imaged when placed in a larger static magnetic field B. These nuclei have a net spin and mostly aligned in the direction of the static magnetic field. The

UCSF LIBRARY

nuclei precession frequency is given by $\omega = \gamma B$. γ is the gyromagnetic ratio, and it is unique for different nuclei. For hydrogen, $\gamma = 42.58 \text{ MHz / T}$.

Most of the nuclear spins are aligned with the field in a lower energy states; in comparison, some of the spins exist naturally in the higher energy states, opposing the field. The nuclei can undergo a transition between the two energy states by absorbing a photon. The photon energy must match exactly the energy difference between the two states. The energy is related to the frequency of the photon, by Planck's constant (h): $E = h\omega$ ($h = 6.626 \times 10^{-34} \text{ J s}$). In magnetic resonance, ω is called the resonance frequency or Larmor frequency.

C) Magnetic resonance imaging

In the presence of static magnetic field B_0 , the magnetization of the spins in the sample is under equilibrium condition. The magnetization vector aligns along the direction of B_0 , usually this direction is called the z-axis. To obtain magnetic resonance signal, a radiofrequency (RF) magnetic pulse B_1 tuned to the resonance frequency of the spins is applied in the x-y (transverse) plane to excite these spins out of equilibrium. Effectively, B_1 applies a torque that rotates the magnetization vectors out of z-axis and into x-y plane. The rotating magnetization vectors induce an electromotive force (EMF) in an RF receive coil oriented to detect changes of magnetization in the x-y plane. This signal is called a free induction decay (FID). Usually a set of FID are acquired and processed to reconstruct an MR image. There is a number of different RF pulse sequences used

UCSF LIBRARY

currently on a human imaging system. Spin echo (SE) and its variant fast spin echo (FSE) are described here.

a. Spin Echo

Spin echo plays an important role in MRI, It is critical for several important imaging and spectroscopy methods. The basic RF pulse sequence is illustrated in figure 3. Following the 90° excitation pulse, the net magnetization vector is rotated into the transverse plane. Once in the transverse plane, the coherent magnetization will start to dephase due to the different magnetic and chemical environments of the spins. After some time τ or $TE/2$,

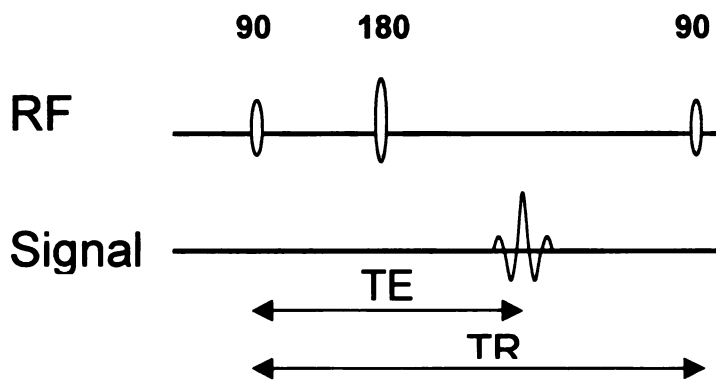


Figure 3. Spin echo schematic showing echo generation at TE after 90 and 180 RF pulse. TR is also demonstrated when the experiment repeats.

an 180° refocusing RF pulse is applied in either the y or the x-axis. The 180° RF pulse reverse the dephasing thus an echo is achieved at the same time τ or $TE/2$ after the application of the pulse. Typically selective excitation is utilized for the

90° and 180° RF pulses to spatially encode the signal acquired (a linear gradient magnetic field is applied during the rf pulses). The experiment is repeated every repetition time (TR) until sufficient number of data points has been acquired to reconstruct the image at the prescribed location.

IJCSE LIBRARY

The spin echo method allows for the refocusing of the spins with minimal affects from tissue magnetic susceptibility variation and other inhomogeneous factors (such as B_0). It is used extensively for imaging organs and tissues where dephasing due to magnetic susceptibility become problematic. Spin echo is also used in diffusion preparation and spectroscopy acquisitions, which will be discussed later.

b. Fast spin echo

Similar to spin echo, fast spin echo employs an RF excitation follow by refocusing pulse. But instead of a single refocusing RF pulse, a train of pulses is used to produce multiple RF spin echoes during one repetition period [11]. Each one of the spin echo is distinctively spatially encoded so multiple data points can be sampled following each excitation pulses.

The primary advantage of FSE is the dramatic reduction in scan time compared to conventional spin echo sequences, especially for T2-weighted imaging that requires longer TR. FSE has the advantage over other fast imaging techniques such as echo planar imaging (EPI) because like spin echo, it is less sensitive to off-resonance effect.

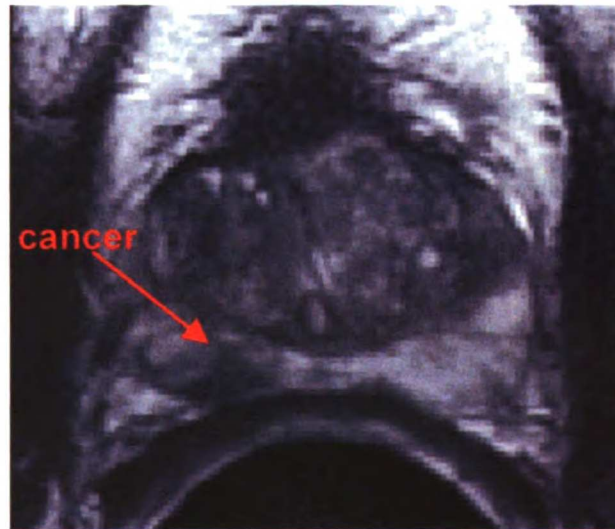


Figure 4. Axial T2-weighted MRI of the prostate. Regions of prostate cancer demonstrate reduced signal intensity compared to benign prostate peripheral zone.

The major drawbacks of FSE include RF power deposition, blurring, ghosting and altered image contrast due to increased lipid signal intensities and magnetization transfer effects.

c. MRI of the prostate cancer at 1.5T

MR images, especially high resolution endorectal T2-weighted images, provide an excellent depiction of prostatic zonal anatomy with the peripheral zone demonstrating higher signal intensity than the central gland (transition, periurethral and central zones). On T2-weighted MRI, regions of prostate cancer demonstrate reduced signal intensity relative to normal prostate peripheral zone tissue due to increase cell density and a loss of prostatic ducts [12, 13]. The role of MRI in prostatic carcinoma has chiefly been the staging of disease rather than the primary diagnosis of carcinoma. And almost all current clinical prostate exams in the United States and Europe are conducted on 1.5T MR scanners. Knowledge of the spread of the cancer outside is critical for determining whether local, systemic or a combination of both therapies is required. With the use of T2-weighted fast spin echo and the use of pelvic phase array coil in conjunction of endorectal coil, the evaluation of extracapsular extension and seminal vesicle invasion can be markedly improved, thereby improving the staging of prostate cancer [12, 14].

D) Magnetic Resonance Spectroscopy

In the presence of the external magnetic field, the electrons will interact with the field. The negative charge of the electronic spin generates a magnetic field that opposes or shields the nucleus from the external field. The extent of shielding depends on the local

UCSF LIBRARY

electron density. The local electron density around each nucleus in a molecule varies according to the type of nuclei and the chemical bonds on the molecule. The difference in energy between the energy states for a nucleus is affected by this chemical shield. Thus the resonance frequency of a spin depends on not only the external magnetic field but also on its molecular environment. This frequency shift is termed the “chemical shift”. Magnetic resonance spectroscopy (MRS) utilizes Fourier transformation of the time domain FID to produce spectrum in frequency domain allowing a way to examine the spins experiencing different molecular environments.

a. Point RESolved Spectroscopy

Point resolved spectroscopy (PRESS) is a technique to localize a volume of interest in three dimensions. For proton spectroscopy, chemical shift selective saturation (CHESS) pulses are used before the 90° excitation pulse. The PRESS sequence is illustrated in

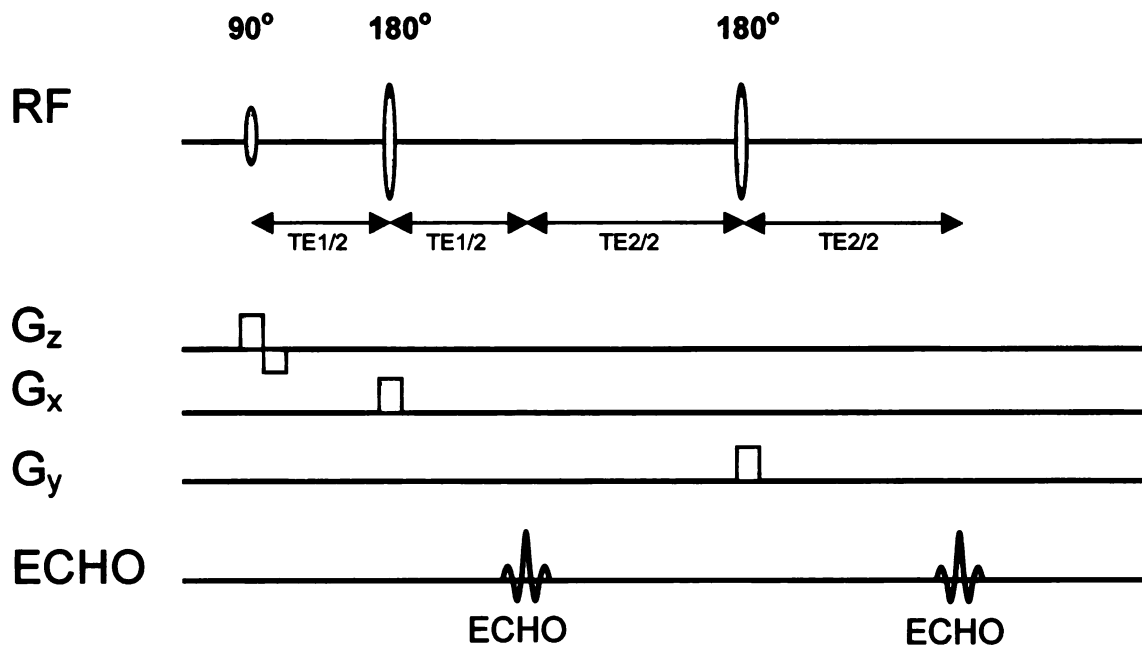


Figure 5. Pulse sequence timing diagram for PRESS. The localized volume is the intersection of the three slice selective pulses. Typically only the second echo is acquired.

IICSE LIBRARY

figure 5. The three slice selective pulses excite (90° pulse) and refocus (two 180° pulse) three orthogonal planes. The spin-echo between the two 180° pulses is not sampled. This technique can be used for single voxel acquisition as well as 2D or 3D acquisition. When used for chemical shift imaging (CSI), phase encoding method is used to yield spatially resolved spectra within the volume of interest. Total acquisition time for the CSI study is then proportional to the repetition time and the number of phase encode in each of the spatial direction.

b. Multi-Nuclear Spectroscopy

In vivo MRS with nuclei other than proton is mostly used for research and animal model. These nuclei include phosphorus, carbon, fluorine, lithium, sodium and nitrogen. To perform MRS with non-proton nuclei on clinical whole body MR system requires addition hardware and software such as dedicated RF transmit/receive coils and pulse sequences. One of the advantages of performing non-proton MRS is that nuclei such as phosphorus and carbon have much larger chemical shift ranges. Water and lipid suppression is not necessary for non-proton MRS and Phosphorus-31 and Carbon-13 spectroscopy provide potential for investigating cellular energy metabolism. But one of the disadvantages for non-proton MRS is its relative low MR sensitivity compared to proton and the low natural abundance for isotopes such as C-13. Thus to achieve adequate SNR, lower spatial resolution and/or longer scan time are often required.

c. MRSI studies of prostate cancer at 1.5T

UIC LIBRARY
UIC LIBRARY

Magnetic resonance spectroscopy imaging (MRSI) in the prostate provides a non-invasive way to detect metabolic markers such as choline, creatine, spermine and citrate within the prostate tissue. Almost all current prostate MRSI studies focus on proton spectroscopy and are performed on 1.5T systems. To perform MRSI of the prostate, accurate volume selection and robust suppression of lipid surrounding the prostate is critical and prostate MRSI packages have recently become commercially available [15, 16]. The resonances of choline, creatine, spermine and citrate occur at distinct frequency, although 1.5T, choline, creatine and spermine overlap considerably. The changes in concentration of these metabolites can be use to identify cancer with high specificity. Specifically, in spectra taken from region of prostate cancer, citrate and spermine are significantly reduced or absent while choline is elevated relative to spectra taken from region of normal prostatic tissue (Figure 6).

One of the strength of prostate MRSI is that many of the biochemical mechanisms that result in the observed metabolic changes are now known. Healthy prostate epithelial cells posses the unique ability to synthesize and secrete large amount of citrate [17]. The decrease in citrate with prostate cancer is due to changes in both cellular function and the organization of the tissue, resulting in the loss of its characteristic ductal morphology. Biochemically, the loss of citrate is linked to changes in zinc levels that are extraordinary high in healthy prostate epithelial cells [18]. Zinc levels are dramatically reduced in prostate cancer and the malignant cells demonstrate a diminished capacity for net citrate production and secretion.

UNIVERSITY
LIBRARY

As in other cancers, the elevation of choline peak is associated with changes in cell membrane synthesis and degradation that occurs with evolution and progression of cancer. Additionally, changes in cell density can also contribute to the observed choline increase in prostate cancer, since densely packed malignant cells replace normal prostatic ductal morphology, forming prostate cancer nodules.

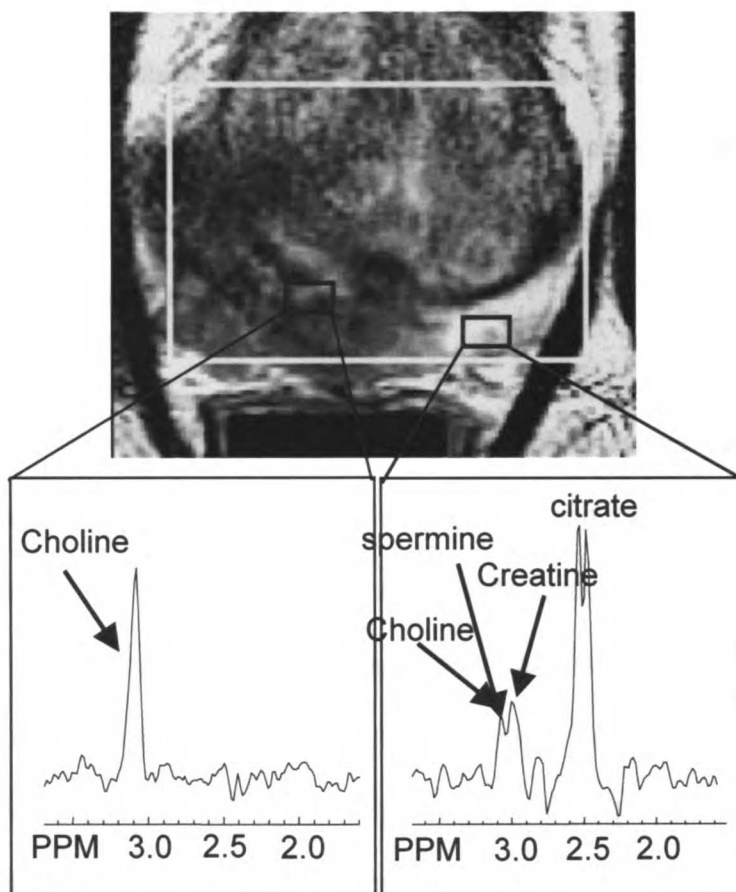


Figure 6. MRSI data from prostate at 1.5T. Note that spermine resonance occurs in between the choline and creatine resonances and the three resonances are overlapped. In the voxel taken from the region of cancer (left), citrate, spermine and creatine were dramatically reduced to baseline level, while choline was significantly elevated.

In recent years combined MRI/MRSI has been shown to improve staging of prostate cancer, localization of intraglandular disease, and assessment of prostate cancer aggressiveness [14, 19-21]. The assessment of cancer spread through the capsule is becoming more difficult as fewer men demonstrate gross cancer spread due to earlier cancer detection. The addition of a MRSI-based estimate of tumor extent to high specificity MRI findings for ECE [22] improved the diagnostic accuracy and decreased the inter-observer variability of MRI in the diagnosis of extracapsular extension of prostate cancer [14]. However, with the spatial resolution currently employed at 1.5T for MRSI (0.34 cc) and measurement variability still limits accurate tumor volume estimates, especially for small tumors (< 0.5 cc) [23].

The high specificity of MRSI to metabolically identify cancer can also be used to improve the ability of MRI to identify the location and extent of cancer within the prostate. A study of 53 biopsy proven prostate cancer patients prior to radical prostatectomy and step-section pathologic examination demonstrated a significant improvement in cancer localization to a prostatic sextant (left and right – base, midgland, and apex) using combined MRI/MRSI versus MRI alone [24]. A combined positive result from both MRI and MRSI indicated the presence of tumor with high specificity (91%) while high sensitivity (95%) was attained when either test alone indicated the presence of cancer.

In addition to the characterization of prostate cancer prior to therapy, MRSI may be particularly valuable for detection of recurrent/residual diseases in post therapy patients

[25, 26]. After therapy the prostate is often significantly decreased in size and in most cases the distinction of normal prostatic zonal anatomy and pathology on T2 weighted images is lost [27, 28], thus the ability of MRI to depict cancer in prostate gland post therapy is very limited. In a study of 65 patients who underwent hormone deprivation therapy, the potential value of MRSI to identify residual cancer and to provide a time course response during hormone deprivation therapy was demonstrated [29]. In a recent study of 21 patients with detectable or rising PSA after external beam radiation therapy [25], using the number of suspicious voxels in MRSI to define different diagnostic thresholds, the area under the receiver operating characteristic curve for MRSI (0.81) was significantly higher than that of MRI (0.51). More specifically, the finding of three or more suspicious voxels in a hemiprostate had a sensitivity and specificity of 89 % and 82 % respectively, for diagnosis of locally recurrent cancer.

These studies have shown good evidence that MRSI can improve the *in vivo* characterization of prostate cancer prior to therapy and can provide information about its response to therapy. However, it is desirable to further improve MRSI techniques to provide higher spatial/spectral resolution, to obtain additional metabolic information based on new markers, and to combine MRI/MRSI with other functional/morphological MR modalities in order to increase the usefulness and scope of applications for prostate MR exams.

E) Diffusion tensor imaging

a. Diffusion of water

Water diffusivity is a measure of the random motion of water molecule due to thermal motion or Brownian motion. Any particle with non-zero mass in an environment of non-zero temperature will have a mean velocity of $\sqrt{\frac{8kT}{\pi m}}$ following the Maxwell-Boltzmann distribution. The phenomenon was first observed by Jan Ingenhousz in 1785 and rediscovered by Brown in 1828. In 1926, Einstein used kinetic theory to derive the diffusion constant, which is proportional to the root mean square of the diffusion distance.

b. MR signal and diffusion

One of the most widely used techniques to produce a MR signal that is sensitive to the motion of water molecule is the spin-echo diffusion preparation method (Figure 7). After the initial excitation RF pulse, two gradients that have equal size are applied around a 180° refocusing pulse.

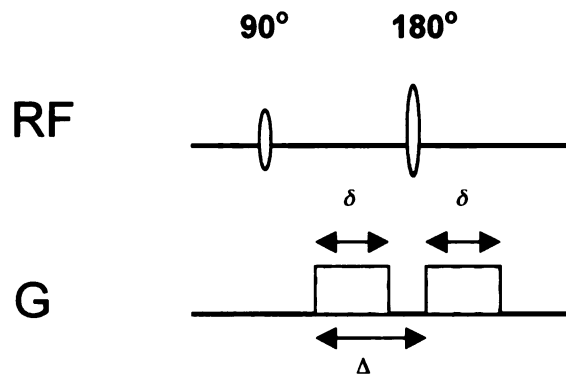


Figure 7. Spin-echo diffusion preparation. Assuming trapezoidal gradients are used, the gradient factor b is related to the diffusion gradients by:

$$b = \gamma^2 G^2 \left[\delta^2 \left(\Delta - \frac{\delta}{3} \right) + \frac{\epsilon^3}{30} - \frac{\delta \epsilon^2}{6} \right]$$

, where ϵ is the ramp of the gradient.

Once the spins are rotated into the transverse plane by the 90° excitation pulse, the spins accumulate a certain amount of phase due to the first gradient. This phase accumulation is exactly reversed by the second gradient after the spins are refocused by the refocusing RF pulse and returned to its original coherent state. However, if some amount of net diffusion occurred during or

between the gradient pulses, the spins affected by the diffusion will not be perfectly refocused and a certain degree of coherence of these spins is lost. This loss of the coherence leads to a decrease in the signal observed.

The measurement of diffusion in MR is determined by the relationship between the loss of the signal and the gradients applied. This relationship is expressed by $S = S_0 \exp(-bD)$, where S_0 is the signal intensity when no diffusion gradients are applied, b is the gradient factor, and D is the diffusion coefficient. Usually the gradients are applied along several specific directions so motion can be measured along different orientations. In diffusion MR studies *in vivo*, the diffusion parameters measured can be related to tissue microstructure, since water mobility differs due to morphological environment (open versus restricted).

c. Single shot fast spin echo diffusion sequence

The timing diagram of the single shot fast spin-echo (SSFSE) diffusion sequence is shown in figure 8. The sequence is a basic SSFSE sequence with the spin-echo diffusion preparation at the beginning of the acquisition. After the initial spin-echo diffusion preparation, a second 90° RF pulse and an additional gradient prior to the pulse is added. This extra pulse-gradient pair destroys half of the magnetization in the transverse plane created by the spin-echo diffusion preparation. This eliminates some of the stimulated echo pathways and allows CPMG condition to be reached in the fast spin-echo echo train [30]. Ignoring relaxation and other imaging related artifacts, SSFSE diffusion sequence will yield about half of the SNR compared to the echo planar diffusion sequence.

However, SSFSE diffusion is insensitive to the distortion and susceptibility artifacts associated with EPI.

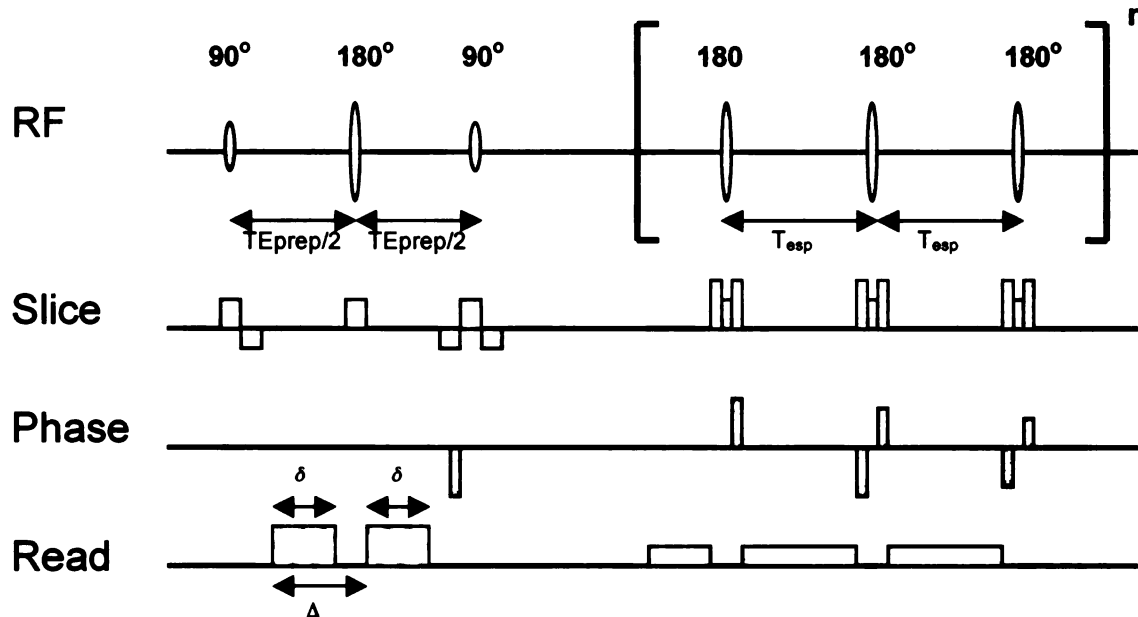


Figure 8. Sequence timing diagram for SSFSE diffusion sequence.

d. Echo-planar diffusion sequence

Similar to SSFSE diffusion sequence, echo-planar imaging (EPI) diffusion sequence begin with a spin-echo diffusion preparation (figure 9). But instead of using an FSE sequence for acquiring the k-space points, fast gradient reversal is utilizing during the readout to traverse k-space. Images can be acquired very rapidly since no additional refocusing pulses are needed. EPI diffusion sequence is used extensively in brain studies. But for body application, the spatial distortion artifact related to magnetic susceptibility effects can be severe and prevent direction comparison or correlation of the diffusion

parameters to anatomical or metabolic information obtained by MRI/MRSI. Parallel imaging [31] can reduce these effects but not totally remove them.

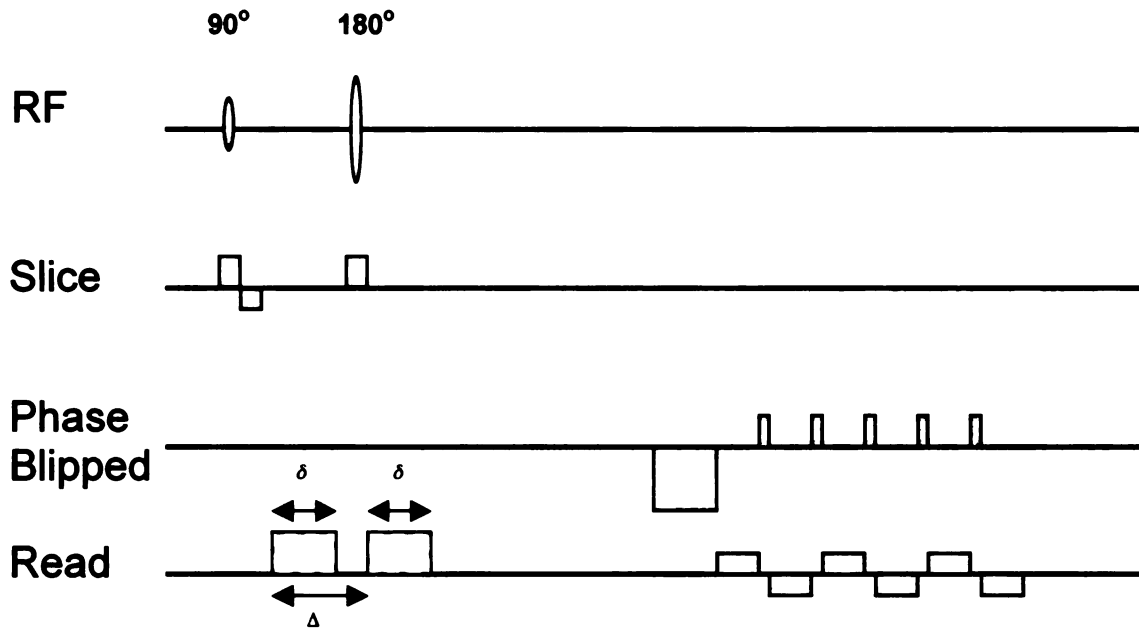


Figure 9. Pulse sequence timing diagram for EPI diffusion sequence.

E) Relaxation time measurements

Ignoring diffusion effects, signal changes in MR after excitation or perturbation of the system are affected by two time constants T1 and T2. These time constants are inherent properties of the environments that the spins reside.

a. T1 relaxation time

T1 relaxation time, or spin-lattice time constant, is the time required for the spins to return to 63% of its original thermal equilibrium energy state following a 90° excitation RF pulse. Physically, T1 involves the exchange of energy between the nuclei and the

surrounding lattice. This relationship is illustrated in figure 10 and is also described by

$$\frac{dM_z}{dt} = \frac{(M_0 - M_z)}{T_1}$$

T1 will be dependent on field-strength because greater energy

exchange is required at higher frequencies, this relaxation effect will take longer at higher fields. Therefore T1 values lengthen with increasing B₀.

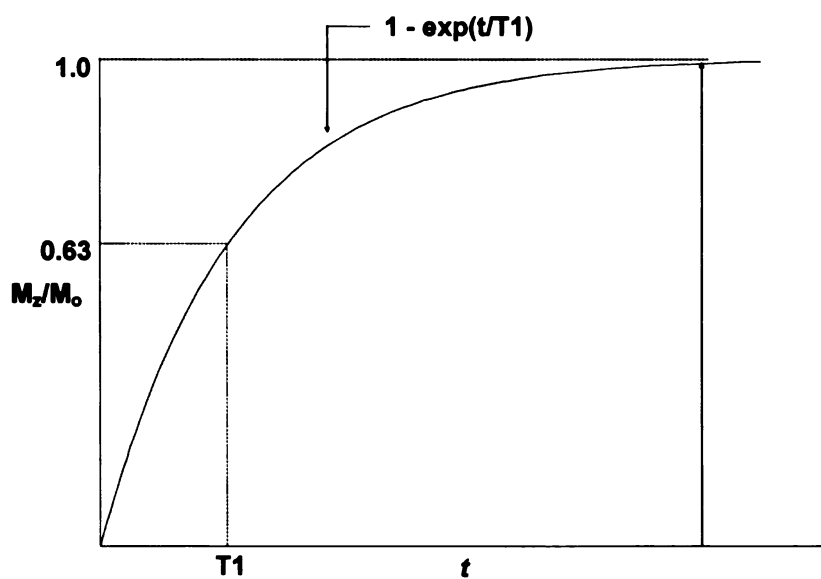


Figure 10. T1 relaxation curve.

T1 relaxation time is most often measured by saturation recovery techniques. In the saturation recovery method, 90° RF pulse is used to rotate the magnetization into the transverse plane. The spins are saturated

because now M_z is zero. The spins are allowed to recover during the TR. If this experiment is repeated, the amount of the signal observed in the following experiment will depend on the amount of recovery. The amount of recovery will depend on the T1 of the spins as well as the TR. By obtaining data from experiments with various TR, data points can be fitted to construct the relationship in figure 10, then T1 can be estimated. Inversion recovery techniques can also be used to measure T1.

b. T2 relaxation time

T2 relaxation time, or spin-spin time constant, is the time required for transverse magnetization to decay to 37% of its initial value. The fluctuations in magnetic field cause spins in the transverse plane to lose their coherence, thus resulted in decay of the net magnetization. This decay is described by $\frac{dM_{x,y}}{dt} = -\frac{M_{x,y}}{T_2}$ and also illustrated in figure 11. T2 relaxation is not field dependent because these fluctuations of energy (magnetic field) are very small compared to B_0 .

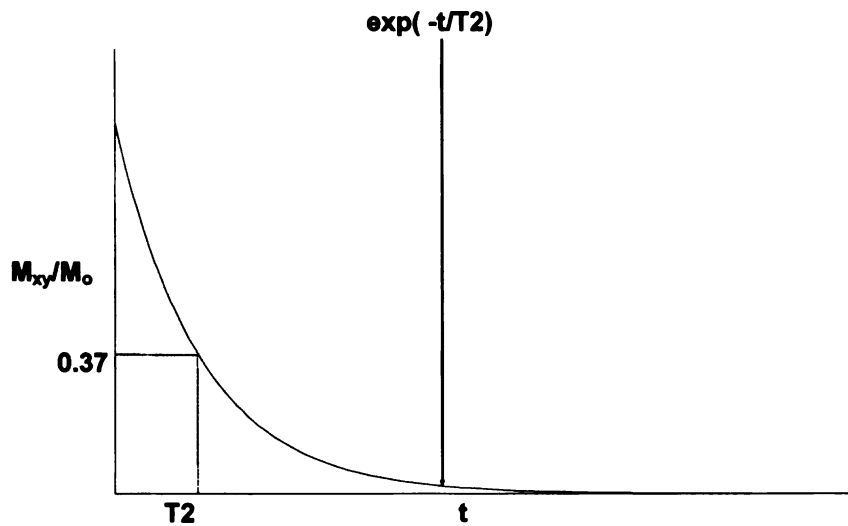


Figure 11. T2 relaxation curve.

The T2 relaxation time is typically measured by using spin-echo experiments with varying echo time and fixed TR. The signal decay at TE in a spin-echo sequence

depends on both T1 and T2. But since $T1 \gg T2$, as long as the TE's used are much less than T1, the signal decay in spin-echo experiments can be attributed primarily to T2 relaxation. T2 decay curves such as figure 11 can be constructed and T2 can be estimated. More sophisticated and more accurate preparation sequences can be developed for more robust T2 measurements.

Chapter 3: 3T MRI of Prostate Cancer

In this dissertation project, I developed, applied and tested new methods for high field (3 Tesla) Magnetic Resonance imaging of prostate cancer. Initially the focus was on improved MR coils and improved anatomic MR imaging.

In recent years, 1.5T endorectal/pelvic phase array coils for prostate imaging have become commercially available as prostate MRI/MRSI has become a routine clinical exam. For 3T however, endorectal coils are not yet available from manufactures. An integrated setup also does not exist for using custom build/prototype 3T endorectal in conjunction with available 3T pelvic phase array coils. In order to take advantage of the potential gain in SNR for prostate imaging at 3T, new hardware needed to be developed.

A) 3T hardware development for prostate imaging

a. Rigid endorectal coil

For imaging of prostate, an endorectal coil provides up to ten fold increase in sensitivity over external body/pelvic coils because of the coil size and its close proximity to the region of interest. Almost all clinical studies conducted at 1.5T utilize the inflatable Medrad (Medrad, Pittsburgh, PA) endorectal coil due to its good coverage and FDA approval. However, with a smaller size and higher Q of a rigid endorectal coil, it is possible to acquire MR data with improved spatial resolution. In addition, the rigid endorectal coil eliminates the air tissue interface of the inflatable balloon coil. This

allows better homogeneity and reduced magnetic susceptibility artifacts in the region of interest. A recent study demonstrated some of the advantage of the rigid coil over the

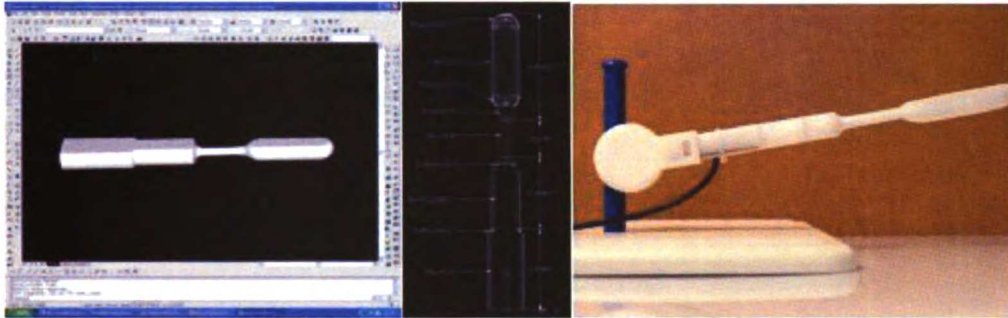


Figure 12. Simulation used for design of the rigid coil for prostate MRI (left) and the finished single element probe (right) attached to a holder for stabilization during imaging.

Medrad coil [32]. In addition, the rigid coil design may allow construction of a phased-array endorectal coil to provide improved parallel imaging capability. It is also possible to construct dual-tuned probes for multi-nuclear MRS studies.

In this study, a single element rigid endorectal coil was constructed based on prior designs. The probe size was approximately 3.9 inches x 1 inch for adequate coverage of the prostate while maximizing patient tolerance. The coil was tuned to 127.7 MHz. The probe was constructed using Delrin plastic. This material exhibits excellent chemical resistance, required for sterilization purpose, and electrical insulating properties, with a dielectric strength of 500 volts/mil and a volume resistivity of 10^{15} ohm-cm. It also has good mechanical properties with ultimate tensile strain of 60%, which is critical to eliminate brittle fractures and to produce a smooth well-tolerated probe. The coil performance was evaluated by MR imaging with phantom and in prostate patient/volunteers (figure 13).

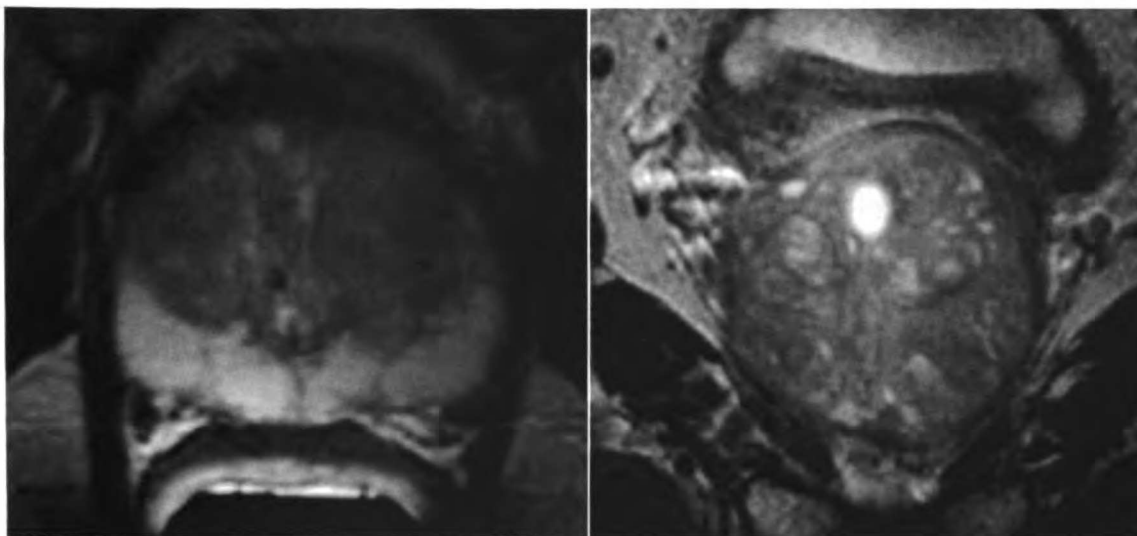


Figure 13. Oblique axial (left) and oblique coronal (right) T2-weighted FSE images acquired from a prostate cancer patient using the custom built single element endorectal coil. Excellent tissue contrast and SNR were obtained.

b. Pelvic phased-array coils

In addition to the endorectal coil, a multi-channel pelvic phased-array coil is required for clinical prostate MRI/MRSI exams for its coverage of lymph nodes in the lower abdominal area. Two different pelvic phase-arrayed coils compatible with GE MR scanners are used at our institution. One is the 4-channel GE pelvic phased-array coil and the other is the 8 channel USAI pelvic phased-array coil. A custom build connector was constructed to allow the prototype endorectal to be used in conjunction with the pelvic phased-array coils. Software that controls the interface between the coils and the MR system was modified as well. In addition to the coverage up to bifurcation, pelvic phase-array coils provide parallel imaging capability, which is especially helpful in reducing susceptibility induced spatial distortion for EPI-DTI. This will be demonstrated in later chapters.

c. Dual-tuned probe

At lower field, ^{31}P MRS has been shown to have the ability to characterize the phosphorylated metabolites of normal, hyperplastic and malignant tissues in human prostate[33]. But limitation in spatial resolution (1.5cc ~ 3cc) hinders its usefulness. At 3T, ^{31}P MRSI is promising due to the potential for increased SNR, making it possible to increase the spatial resolution. But the lack of double-tuned 3T prostate coils has prevented the development of this technique.



Figure 14. The internal circuitry of the concentric coplanar dual-tuned prostate probe.

The dual-tuned prostate probe developed in this study uses the identical rigid endorectal housing as the single element endorectal coil described before, with the same size and material. Two different designs of the coil were constructed: a coplanar design and a concentric dual layer design. In both designs, the two coil elements (^1H and ^{31}P) were built from solid copper wire into oval shape. Four capacitors were distributed symmetrically around each oval element on the major and minor axes. This minimized the downfield shift of the resonance frequency during coil loading. In both designs, the ^1H coil was designed for use in receive only mode, with tuning and matching circuitry as well as an active PIN diode trap for ^1H coil detuning during body coil transmit, built into the handle of the probe (figure 14).

The ^{31}P portion of the coil was designed for use in both transmit and receive modes. The objective of both design was to maximize ^{31}P sensitivity. For the concentric coplanar design, the inner coil was tuned to 51.7 MHz (^{31}P) while the outer coil was tuned to 127.7 MHz (^1H). This maximized the coverage of ^1H coil while reducing the volume covered by the ^{31}P coil, thus maximizing the ^{31}P coil sensitivity. For the dual layer design, both ^1H and ^{31}P coils have the same size, therefore the ^{31}P coil was placed nearest to the prostate to maximizing the SNR for the less sensitive nuclei. This design however, reduces the proton sensitivity slightly since an additional 3mm distance was added between the proton coil and the prostate gland. The coils were tuned and matched to 50 ohms and decoupled from one another while loaded on the laboratory bench.

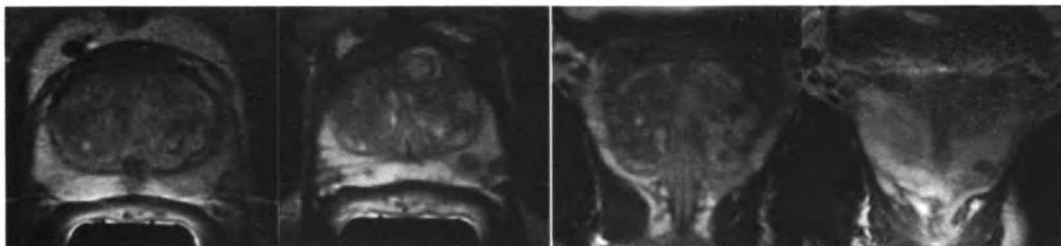


Figure 15. Oblique axial (left) and oblique coronal (right) T2-weighted fast spin-echo images of the human prostate acquired using the coplanar $^1\text{H}/^{31}\text{P}$ dual-tuned endorectal coil.

The performance of the coil was evaluated by imaging in phantoms, volunteers and prostate cancer patients. Non-localized phosphorus spectra was also acquired in prostate cancer patients (figure 16). Further testing is required to define the SNR and spatial coverage for ^{31}P MRS studies in vivo at 3T.

Similar designs were also used to construct dual-tuned $^{13}\text{C}/^1\text{H}$ probe for ^{13}C MRS studies of human prostate in vivo. With the possibility of injecting hyperpolarize ^{13}C compounds into human to increase the MR sensitivity for ^{13}C molecules by $>10,000$ fold, ^{13}C MRS of prostate could provide valuable additional metabolic information [34].

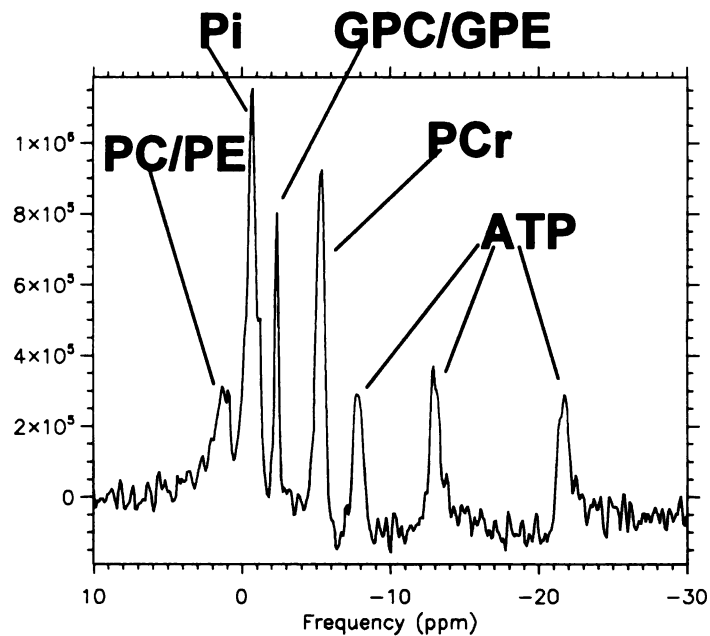


Figure 16. Non-localized ^{31}P spectra acquired from human prostate in vivo using the coplanar dual-tuned endorectal coil. Data was acquired with 1.0s TR, 5000Hz / 1024 pts filter and 64 averages.

B) Imaging of Prostate Cancer at 3T

a. High resolution T2-weighted FSE

With the potential two-fold SNR increase in SNR at 3T over 1.5T, it should be possible to acquire MRI from prostate at a higher spatial resolution without compromising the imaging quality. Currently at 1.5T, axial T2-weighted FSE images are acquired with 14 cm FOV (16 cm for coronal images), 256 x 192 spatial encoding matrix, 3mm thick

slices, and TR/TE of 6s/102ms. Typically three averages are performed to obtain good SNR and total scan time required is approximately 3.5 minutes. The preliminary goal for improving the anatomical imaging of prostate was to increase the spatial resolution without any degradation in imaging quality/contrast and increase in scan time while maintaining the spatial coverage. 3T axial FSE images were acquired with 12 cm FOV (14 cm FOV for cononal images) with the same spatial encoding matrix and sequence timing as compared 1.5T. By using the same encoding matrix and a smaller FOV, the spatial resolution is increased. Initial 3T-1.5T comparison studies were performed using 3T prototype Medrad inflatable balloon coil and commercial 1.5T Medrad coil. A total of ten patients were scanned at both 1.5T and 3T. Each patient was scanned at both 3T and 1.5T within at most two weeks and often on the same day. Oblique axial T2

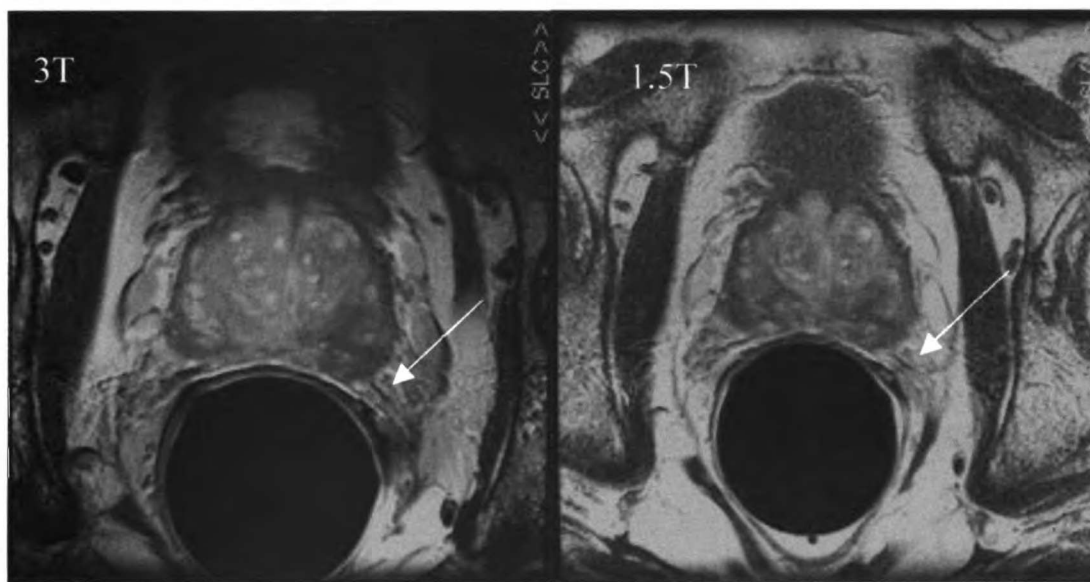


Figure 17. Prostate cancer patient imaged at both 3T and 1.5T using Medrad endorectal coil. Oblique axial T2-weighted FSE images acquired at 3T in 3:42 using 256x192 encoding matrix, 6000s/102ms TR/TE, 3mm thick slices and 12 cm FOV (14 cm for 1.5T). Improved image quality was observed at 3T. Finer structures such as the neurovascular bundles (arrow) were better depicted at 3T due to higher spatial resolution and increased susceptibility weighting.

weighted FSE images acquired at 3T demonstrated excellent tissue contrast and improved depiction of smaller structures probably due to the increase in spatial resolution used at 3T as well as the increase in susceptibility at higher field (figure 17). Oblique coronal FSE images also showed similar improvement at 3T over 1.5T (figure 18). Increased signal-to-noise ratio (SNR) was also observed in the 3T images over 1.5T images. This is most likely due to the fact that the increase in spatial resolution (~26% smaller voxels at 3T) utilized only part of the possible 2-fold SNR increase at 3T over 1.5T.

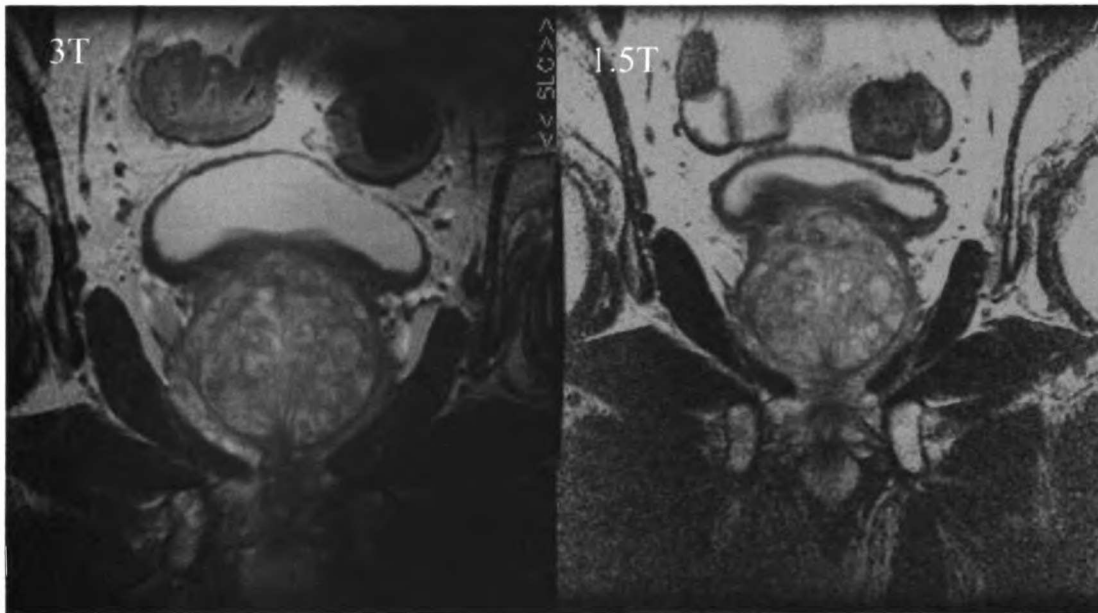


Figure 18. Oblique coronal T2-weighted FSE images acquired at 3T in 3:42 using 256x192 encoding matrix, 6000x/102ms TR/TE, 3mm thick slices and 14 cm FOV (16 cm for 1.5T). Note the SNR increase of the 3T images over the 1.5T images.

Although further studies with correlations to “gold standard” histopathology are needed to demonstrate the benefits of anatomical MR imaging at 3T over 1.5T. It is reasonable to speculate that the increased image quality, resolution and SNR at 3T may improve the

staging of prostate cancer using MRI. It may also increase the sensitivity of MRI for localization of small foci of disease.

Chapter 4: Prostate MRSI at 3T

The goal of this part of the dissertation project was to develop and test new techniques for obtaining metabolic MR spectroscopic imaging at 3 Tesla. To date, virtually all prostate MRI/MRSI studies have been acquired using 1.5 Tesla MR systems. The typical spatial resolution of MRSI at 1.5T has been ~0.3 cc or a voxel with 7mm on a side [29, 35, 36]. Due to the complex zonal anatomy of the prostate and the often small, multi-focal nature of prostate cancer, partial volume effects remain a problem in some MRSI studies even at 0.3 cc spatial resolution. With the recent availability of 3T whole body systems, the potential exists for improving spectral signal-to-noise and resolution for prostate MRSI using these high field MR scanners. An aim of this project was to determine if the theoretical two-fold increase in signal-to-noise ratio (SNR) from 1.5T to 3T could be realized thus allowing the MRSI data to be acquired with half the voxel size at 3T without compromising spectral quality. The increase in spectral resolution at 3T also may offer better separation of the choline, polyamine and creatine resonances that overlap considerably at 1.5T.

There have been a few recent studies investigating prostate MRSI at 3T [37-44], however, none have demonstrated the theoretical doubling in signal-to-noise ratio (SNR) possible at 3T as compared to 1.5T. In addition, these studies have reported major challenges in obtaining and quantifying 3T prostate MRSI data due to differences in J-modulation of the citrate resonance, magnetic susceptibility induced magnetic field inhomogeneities, and chemical shift misregistration as compared to 1.5T studies. In this

chapter, I describe in detail the technical challenges and the methods I developed to address them.

A) Challenges for prostate MRSI at 3T

a. J-modulation of the citrate resonance

One of the challenges for prostate MRSI at 3T is the accurate quantification of citrate at a

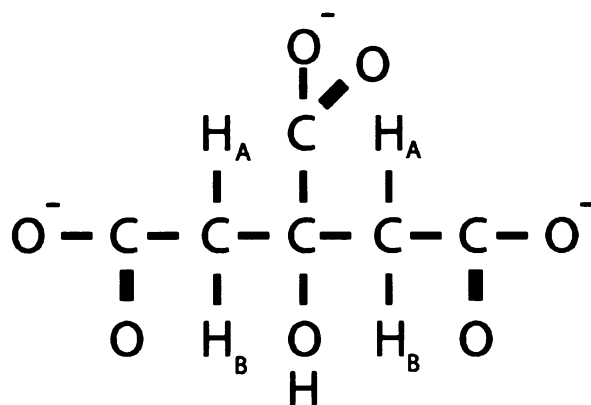


Figure 19. Chemical structure of the citrate molecule. The AB methylene proton coupling partners are indicated.

reasonable echo time to allow the decay of macromolecule signals and to avoid T2 signal loss (60~130 ms). At both 1.5T and 3T, the methylene protons of citrate molecule (figure 19) are considered to be a strongly coupled AB spin system resulting in changes in the appearance of the citrate doublet of doublets and a complex modulation of the citrate resonances with increasing

echo time[45, 46]. It has been shown that with the conventional Point-RESolved Spectroscopy (PRESS) pulse sequence at 1.5T, the outer resonances of the citrate doublet of doublets represents only a small percentage of the inner resonances and the inner resonances of the citrate doublet of doublets are maximally upright at an echo time of between 120 and 130 ms [45].

At 3T, the outer resonances of the citrate doublet of doublets become significantly larger and, within the range of acceptable echo times for in vivo prostate MRSI using PRESS sequence, an inverted citrate with the outer lines out of phase is observed at the TE of 90 ms [37, 41]. This spectral pattern is undesirable because the inverted lines may result in cancellation with neighboring spectral component in inhomogeneous or poorly shimmed voxels. The out of phase components also make accurate quantification difficult. Our initial J-resolved MRS studies have shown completely upright citrate at an echo time (TE) of 250-260 ms (figure 20), but acquiring prostate MRSI data at this long TE would result in substantial signal loss due to T2 decay especially for the choline resonance. Investigators utilizing the J-PRESS sequence demonstrated an upright citrate at a TE of 180 ms, which is still impractically long [40]. Other studies have shown that

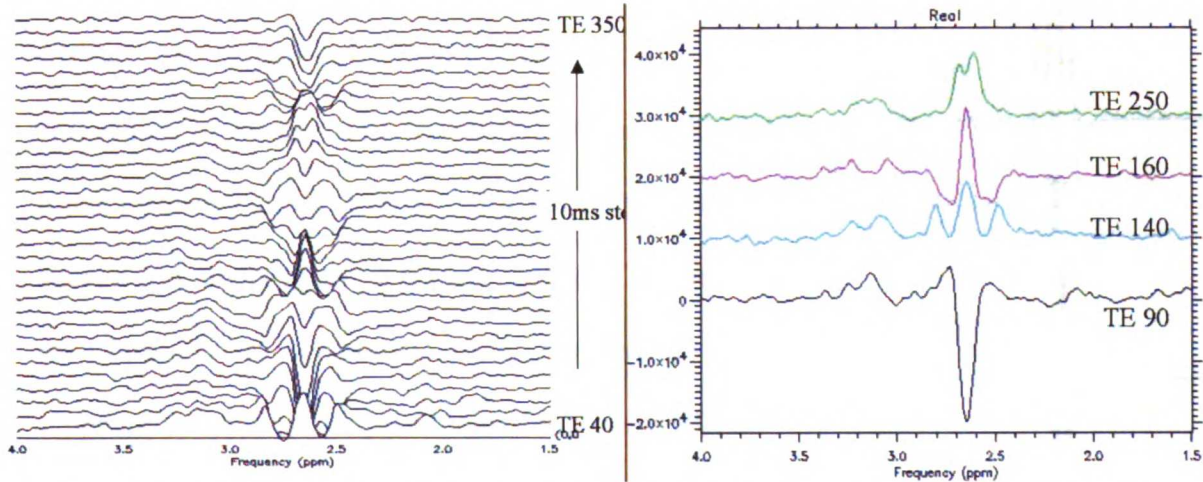


Figure 20. TE dependence of the phase and amplitude modulation of the citrate resonance at 3T. This data was acquired in-vivo with J-resolved PRESS sequence, with minimum TE of 40 ms, 10 ms steps and maximum TE of 360 ms.

short echo time (30-35 ms) acquisitions provided favorable behavior for citrate (upright), but suffer from spectral contamination of macro-molecules, lipids and polyamines obscuring metabolites of interest such as choline and creatine [39, 42].

Thus, the ideal 3T MRSI technique must allow acquisition of fully upright citrate resonance for robust and accurate quantification at an echo time that avoids both contamination of macromolecules and T2-decay of the metabolites of interest.

b. Other considerations for 3T prostate MRSI

In addition to the J-modulation changes, several other challenges exist for performing prostate MRSI at 3T. The increase in magnetic susceptibility with the field strength increases the magnetic inhomogeneity in and around the region of interest, which can cause broadening of peaks. The broadening of the lipid and water resonances may overlap with the metabolites of interest and rendering the spectra unusable. Thus despite the increase in chemical shift dispersion, lipid suppression remains a major concern for prostate MRSI.

Another important consideration for 3T prostate MRSI is relaxation effects. The theoretical increase in T1 relaxation time at 3T over 1.5T would cause the signal to saturate more if the same repetition time used at 1.5T is

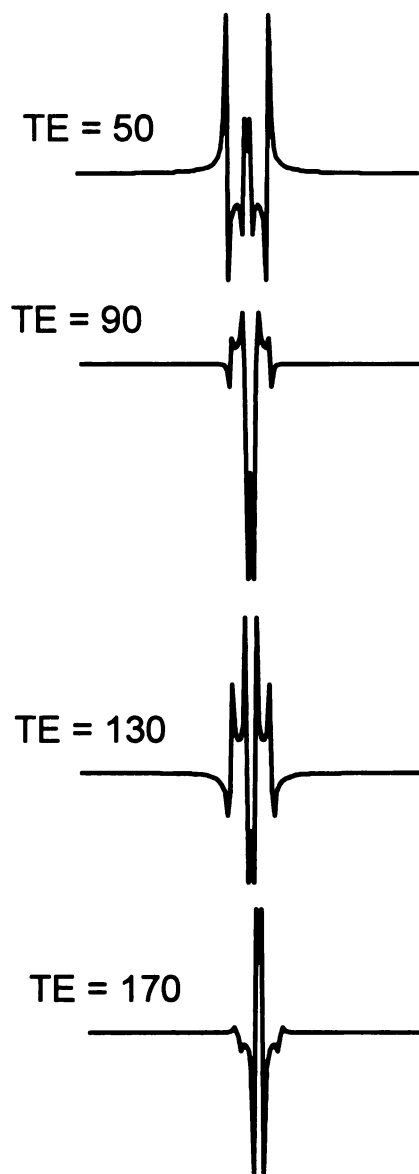


Figure 21. The effect of J-modulation on the appearance of the citrate spectrum at 3T with the conventional PRESS sequence.

used at 3T. This signal saturation would negate at least some of the SNR gain at 3T. Another important factor for in-vivo MR is the increase of energy deposition by RF pulses into the tissues required at increased field strength. The RF pulse and sequence parameters must be designed to keep specific absorption rate (SAR) below the FDA approved limit and peak power below the RF amplifier limits. Also increased with field strength is the chemical shift misregistration, which can result in errors in metabolic assessment of the prostatic tissue. Design of higher bandwidth or optimized spectral-spatial RF excitation and refocusing pulses along with robust outer volume suppression are necessary to reduce the artifact.

B) Sequence Design for Prostate MRSI at 3T

a. Theory and simulations

The behavior of the strongly coupled citrate AB spin system is not readily described in classical terms and requires a quantum mechanical description. The most convenient expression for calculating citrate behavior is obtained through the density matrix formalism. These matrix expression can be implemented as numerical simulation.

The density matrix, ρ , holds all of the information about the spin system at any point in time, with the evolution of the system as a function of time governed by the Hamiltonian

$$H: \rho = e^{-iHt/\hbar} \rho e^{iHt/\hbar}.$$

The Hamiltonian for an AB spin system can be written as follows:

$$H = (\omega_A I_z + \omega_B S_z) + 2\pi J(I_x S_x + I_y S_y + I_z S_z).$$

Where I and S are the angular momentum operator for the spins A and B, respectively, ω_A and ω_B are the chemical shifts of spins A and B, respectively. And the subscripts denote the direction along which operators act. The first bracketed expression: $(\omega_A I_z + \omega_B S_z)$ is the conventional Zeeman Hamiltonian, and the second term: $2\pi J(I_x S_x + I_y S_y + I_z S_z)$ is a dot product between the operators for spins A and B, governing the coupling behavior. With the Hamiltonian of the AB system written in matrix form and a matrix expression for the effect of an RF pulses [47], the behavior of $H: \rho = e^{-iHt/\hbar} \rho e^{iHt/\hbar}$ was investigated in MATLAB™.

The behavior of the AB spin system with the conventional PRESS sequence and echo times typically used in *in vivo* application (70 ms – 140 ms) was simulated by this method (figure 21). At these echo times with conventional PRESS sequence, there is enough evolution time that J-coupling significantly changes the citrate spectrum. The result of the simulation was consistent with what we observed in the J-resolved human study (figure 20). The best condition that can be found at a practical echo time is maximally inverted citrate at TE of 90 ms. But as mentioned in the previous section, the outer lines of the doublet of doublet are out of phase, which results in difficulties in quantifying the citrate resonances.

It has long been known that [48] a train of closely spaced refocusing pulses could inhibit J-modulation, even in strongly coupled systems such as that described above. The reason for this, as given analytically in [48], is that the frequency of the echo train modulation depends on a factor Rt_{cp} , where t_{cp} is the time between refocusing pulses. The variable R

is given by: $R = (\delta^2 + J^2)^{0.5}$, where J is the coupling constant and δ is the chemical shift difference between spins A and B (both values in Hz). The dependence of the modulation on Rt_{cp} is complex, but the modulation can be shown to be negligible when $Rt_{cp} \ll 1$ [49, 50]. For citrate at 3T, δ and J are approximately 16 Hz and 15 Hz [51]; thus the limit for t_{cp} for negligible citrate modulation is $t_{cp} \ll 46\text{ms}$.

b. MLEV-PRESS sequence and spectral-spatial refocusing pulses

The goal of the pulse sequence design was then to incorporate the J-refocusing properties

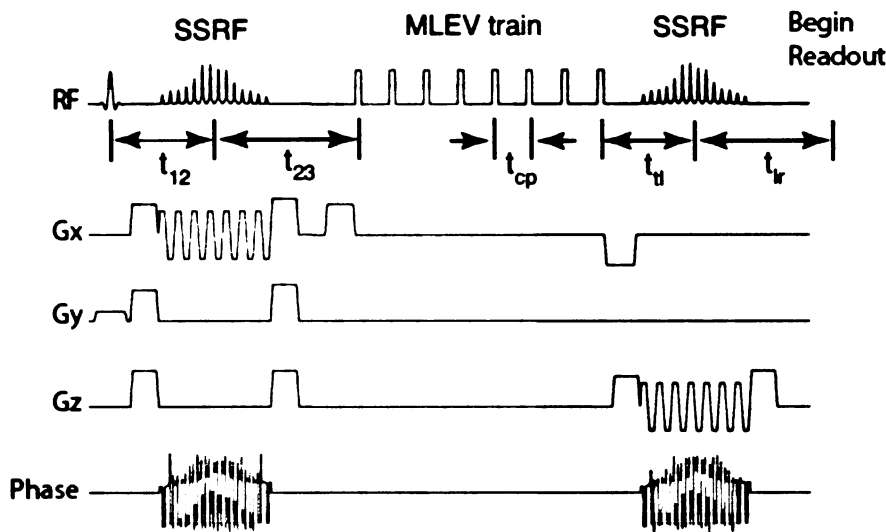


Figure 22. Pulse timing diagram of the new 3T prostate MRSI sequence. Spatial selection is similar to that of conventional PRESS sequence, with spatially selective 90° pulse and two spectral-spatial 180° refocusing pulses selecting three dimension of the volume. The train of non-selective pulses with MLEV phase cycling provides J-refocusing.

of a train of closely spaced refocusing pulses (short t_{cp}) into a pulse sequence that has the other necessary properties for *in vivo* prostate MRSI. Robust water and lipid suppression accomplished by

using spectral-spatial RF (SSRF) refocusing pulses within the PRESS sequence has been shown to be a reliable approach [16]. A significant advantage of SSRF pulses is that the

short duration of the sup-pulses (e.g., 1 ms) provides high bandwidth in the spatial dimension (e.g., 8 kHz). This property limits the chemical-shift mis-registration that becomes problematic at high field. The new sequence design for 3T prostate MRSI is shown in figure 22.

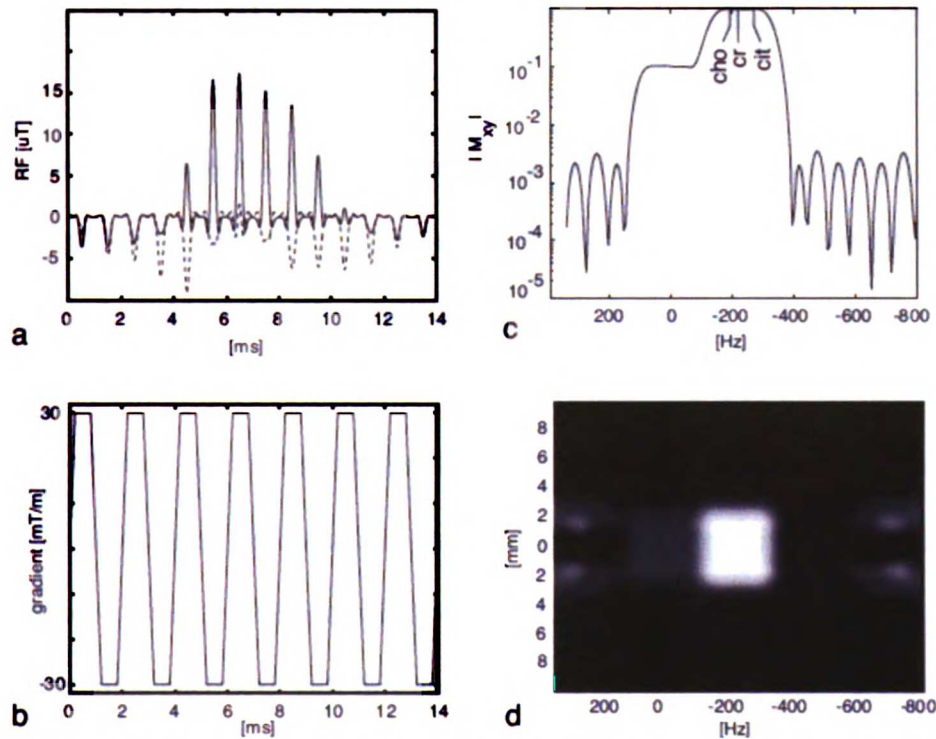


Figure 23. Design of the short spectral-spatial refocusing pulses. The RF (a) and the gradient (b) waveform are shown. The net pulse duration is 14 ms, with each sub-lobe 1 ms long. The spectral response (c) of the pulse shows a passband for the metabolites of interest from -162 Hz (3.43 ppm) to -297 Hz (2.37 ppm), the frequencies relative to water. With two of these SSRF pulses (as in figure 22), the spectral profile will be the square of the profile shown, given 100-fold suppression of water in the attenuated passband and 120 dB (million fold) suppression of lipids in the stop band beginning at -390 Hz (1.65 ppm). The 2D spatial vs. spectral profile (d) is plotted at the minimum slice thickness of 4.8 mm (FWHM).

To limit the J-modulation during the RF pulses, new dualband spectral-spatial RF pulses were designed to be as short as possible yet retain adequate tolerance to main-field inhomogeneity [16]. The B-polynomial for the spectral dimension (one of the input to the Shinnar-Le Roux transform [52]) was designed using the complex-valued version of the Remez exchange algorithm, as implemented in MATLAB™. To reduce the peak RF amplitude, non-linear phase was created across the spectral passband using the “root flipping” method [53, 54]. This B-polynomial, together with B-polynomial for the spatial dimension (time-bandwidth = 7.2), was passed through the inverse 2-dimensional Shinnar-Le Roux transform [55] to generate the SSRF pulses used in the sequence (figure 23). The gradient waveform was designed to meet the constraint that the peak amplitude of the pulse be within the RF amplifier limits for body-coil transmission (16 μ T). In order to keep the amplitude down, a fairly long (1ms) sub-lobe duration was used, and the length of each gradient ramp was limited to 200 μ s, giving a longer plateau. This caused the maximum gradient amplitude to be 30 mT/m, giving a minimum voxel thickness of 4.8 mm. The bandwidth of the pulse in the spatial dimension is 6.1 kHz, giving a nominal chemical-shift misregistration of 0.5 mm for citrate relative to choline, assuming a 40 mm profile. However due to the use of the 2-dimensional design method [55], the chemical-shift misregistration over the passband (choline to citrate) is zero. The spectral response of the pulse accommodates a +28/-30 Hz tolerance to main field inhomogeneity (5% attenuation of citrate and choline).

These new SSRF pulses were implemented in the modified version of the PRESS sequence shown in figure 22. A train of eight non-selective refocusing pulses was used,

with an 8-step MLEV [56] phase cycle to provide some tolerance to RF inhomogeneity

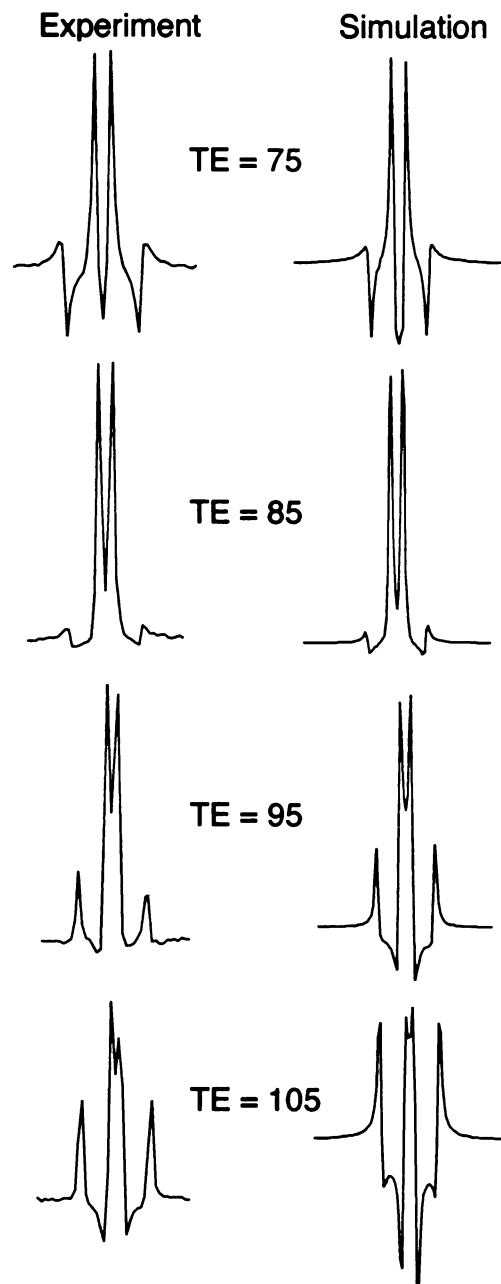


Figure 24. Results from phantom experiment using the new pulse sequence. The citrate spectrum is shown at various echo times, with corresponding simulation results for comparison.

and transmit gain variations. For comparison with experimental results, the J-modulation of citrate within this pulse sequence was simulated using the density matrix method described above, with $H = (\omega_A I_z + \omega_B S_z) + 2\pi J(I_x S_x + I_y S_y + I_z S_z)$ written in matrix form, and a matrix expression for the effect of an RF pulse [47], the behavior of H : $\rho = e^{-iHt/\hbar} \rho e^{iHt/\hbar}$ was investigated in MATLAB™. Each spectral-spatial pulse was represented by a series of hard pulses (14 for each SSRF) separated by the sub-lobe duration (1 ms), with each hard pulse having the same flip angle as the corresponding sub-pulse and free evolution between the hard pulses.

The sequence was implemented on a whole-body GE 3 T scanner (GE Healthcare Technologies, Waukesha, WI). Phantom data was acquired from a spherical phantom containing metabolite of interest (choline, creatine and citrate) in solution. A prototype 3T

Medrad inflatable endorectal coil (Medrad Inc., Pittsburgh, PA) was used for signal reception and body coil was used for excitation. 3D MRSI data were acquired from the phantom with 12 x 8 x 8 phase encoding matrix and nominal resolution of 0.157 cc (5.4 mm per side); TR was 1.3s. The echo time was varied from 75 ms to 105 ms to investigate the J-modulation (figure 24). Good agreement between simulation and experimental can be seen. However, there are some slight discrepancies that are likely due to the approximate representation of the SSRF sub-pulses with hard pulses in the simulation. The citrate resonance at TE of 85 ms appears to meet the desired criteria with almost completely upright and high amplitude citrate central peaks and reduced outer lines. However, citrate J-modulation is not completely suppressed, instead, the J-modulation has been manipulated such a useful spectral pattern for citrate is achieved at a reasonable echo time for prostate MRSI.

C) MRSI of prostate cancer at 3T

The new MLEV-PRESS sequence incorporating the dualband SSRF and the refocusing pulse train was applied in twenty-five 3T MRI/MRSI prostate cancer exams to investigate its ability to provide high spatial and spectral resolution 3D-MRSI data at 3T. A preliminary comparison study between 3T and 1.5T MRSI data on ten of patients was also conducted to investigate differences in SNR, spectral resolution and the detection of abnormal metabolite levels.

a. Patient population

Thirty-five MRI/MRSI exams were performed on twenty-five men who ranged in age from 52 to 73 years old with a mean age of 63.8. All twenty-five patients had one exam at 3T and ten of the patients had prostate MRSI exams at both 3T and 1.5T. In all cases the 1.5T exam was acquired within 2 weeks of the 3T exam, with the average time between exams being 1.5 day, and eight of the ten 3T/1.5T exams were performed on the same day. Twenty of the twenty-five patients had biopsy proven prostate cancer; three age-matched subjects had negative biopsy results, and two other subjects were scanned due to a rising PSA without biopsy proven prostate cancer. For the twenty-three patients who had prior biopsy, the MRI/MRSI exams were performed with a minimum of 54 days and an average of two years and 349 days after biopsy. Twenty-two patients had no prior therapy, one patient had external beam radiation therapy, and two patients had combined androgen deprivation therapy (anti-androgen + LHRH agonist).

b. 3T MRI/MRSI protocol

All 3T examinations were performed on a 3T GE Signa scanner (GE HealthCare Technologies, Waukesha, WI) using the body coil for excitation and a 3T Medrad prototype inflatable endorectal coil (Medrad, Pittsburgh, PA) filled with Flutech_T14™ (F2 Chemicals, UK) or a custom designed rigid coil in conjunction with a pelvic phase array coil for signal reception. All 1.5T examinations were performed on a 1.5T GE Signa scanner, using body coil for excitation and a Medrad inflatable endorectal coil filled with Flutech_T14™ (F2 Chemicals, UK) or a USA Instrument rigid coil (USA Instrument, Aurora, OH). Flutech_T14 is a fully fluorinated, colorless, odorless, non-toxic fluid with a magnetic permeability similar to tissue and thus is an ideal substitute

for air to inflate the endorectal coil. Twenty of the twenty-five 3T exams were performed using the custom designed rigid coil and five were performed using the Medrad coil. The same type of the coil (rigid or inflatable) were used at both 3T and 1.5T for each of the 10 patients who underwent both 3T and 1.5T exams.

Both 1.5 and 3T MRI/MRSI exams included the following imaging sequences. Sagittal fast spin echo (FSE) localizer images were acquired to check coil placement and to prescribe the subsequent imaging series. Oblique axial T2-weighted FSE images (TR/TE = 6000/102ms, 3mm slice thickness, no inter-slice skip, 12 cm FOV at 3T and 14cm FOV at 1.5T, 256 x 192 matrix, and no phase wrap) were obtained next. Oblique coronal T2-Weighted FSE images (TR/TE = 6000/102ms, 3mm slice thickness, no inter-slice skip, 14 cm FOV at 3T and 16 cm FOV at 1.5T, 256 x 192 matrix, and no phase wrap) were acquired following the oblique axial FSE images. Axial T1-weighted SE images (TR/TE = 950/9ms, 5mm slice thickness, 1mm inter-slice skip, 24 cm FOV and 256 x 192 matrix) were also obtained.

The MLEV PRESS-MRSI volume was selected from the axial T2-weighted FSE images to include as much of the prostate as possible but to exclude periprostatic lipid and seminal vesicles. For the exams at 3T, 12 x 8 x 8 phase-encoding steps were used to yield spectra with 0.157 cc nominal spatial resolution (5.4 mm per side) with the larger FOV in the right-left orientation. The 3T 3D-MRSI acquisition parameters were: TR = 1.3s -1.5s; TE = 85ms; spectral width = 2000 Hz; 1024 complex points; 1 acquisition per phase-encode step; and a scan time of 16 to 18 min. For the exams at 1.5T, 16 x 8 x 8

phase-encoding steps were used to yield spectra with 0.343 nominal spatial resolution (7 mm per side). The standard pre-scan routine provided by the manufacturer was performed just prior to the MRSI acquisition at both 1.5T and 3T. The pre-scan routine included the setting of center frequency on water resonance, setting transmit gain and automatic shimming of the MRSI volume with linear shim correction. A PRESS sequence with spectral-spatial refocusing pulses was used for all 1.5T MRSI acquisitions [16]. The 1.5T 3D-MRSI acquisition parameters were the same as used routinely for patient studies [35, 36, 57] and they were: TR = 1s; TE = 130ms; spectral width = 1000 Hz; and 512 complex points; and a scan time = 17 min. For one 3T exam conventional PRESS with the 3T spectral spatial pulses were acquired with the same parameters as the MLEV acquisitions except TE=90ms.

c. T1 measurements

In five subjects, additional 3T single voxel MRS acquisitions with varying repetition times were obtained to estimate the T1 of the prostate metabolites at 3T. Single voxel spectra were acquired from a ~15cc volume within the prostate that contains both peripheral zone central gland with four (n = 2) to six (n = 3) different repetition times ranging from 650ms to 5s for these five patients. Single voxel spectra at varying echo times were acquired with 32 averages. The other MRS acquisition parameters were the same as for the 3D MRSI series.

d. Data analysis

Custom software interfaced with IDL was developed to analyze and display the spectroscopy data. The reconstruction began with apodization with a 3 Hz gaussian in the time domain and followed by Fourier transform in the time and three spatial domains to produce the spectral arrays. Then, the spectra were corrected for phase and frequency variations utilizing the residual water peak. The resultant spectra were baseline corrected

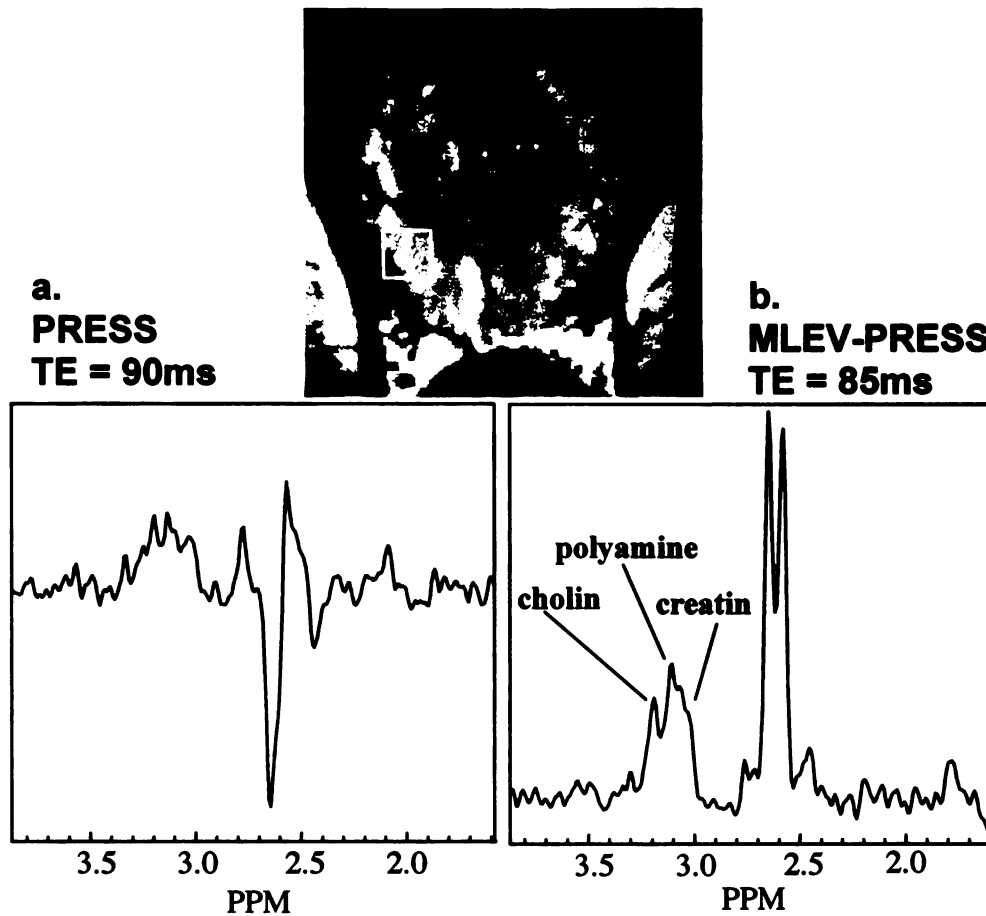


Figure 25. MRSI data acquired at 3T with both a) conventional PRESS sequence and b) the MLEV-PRESS sequence from a fifty-nine year old prostate cancer patient. At an echo time of 90ms using the conventional PRESS sequence, the citrate peak is inverted but with considerable upright side-bands that make quantification of citrate difficult (a). Using the new MLEV-PRESS sequence at an echo time of 85ms, citrate was completely upright with a flat baseline which facilitates measurement of its peak height and area. Other imaging parameters used in the 3T PRESS acquisition was identical to that of MLEV-PRESS acquisition at 3T.

and then peak heights were calculated. The noise was estimated from a region in the right of the spectrum that does not contain any proton resonances [58, 59].

A Marquardt non-linear parameter search algorithm was used to fit the data to calculate T1 relaxation times for the citrate and choline resonances [60, 61].

e. Results

As demonstrated in the representative data shown in figures 25-28, high quality T2-weighted images and 3D MRSI data were obtained from the 3T patient studies. At 3T

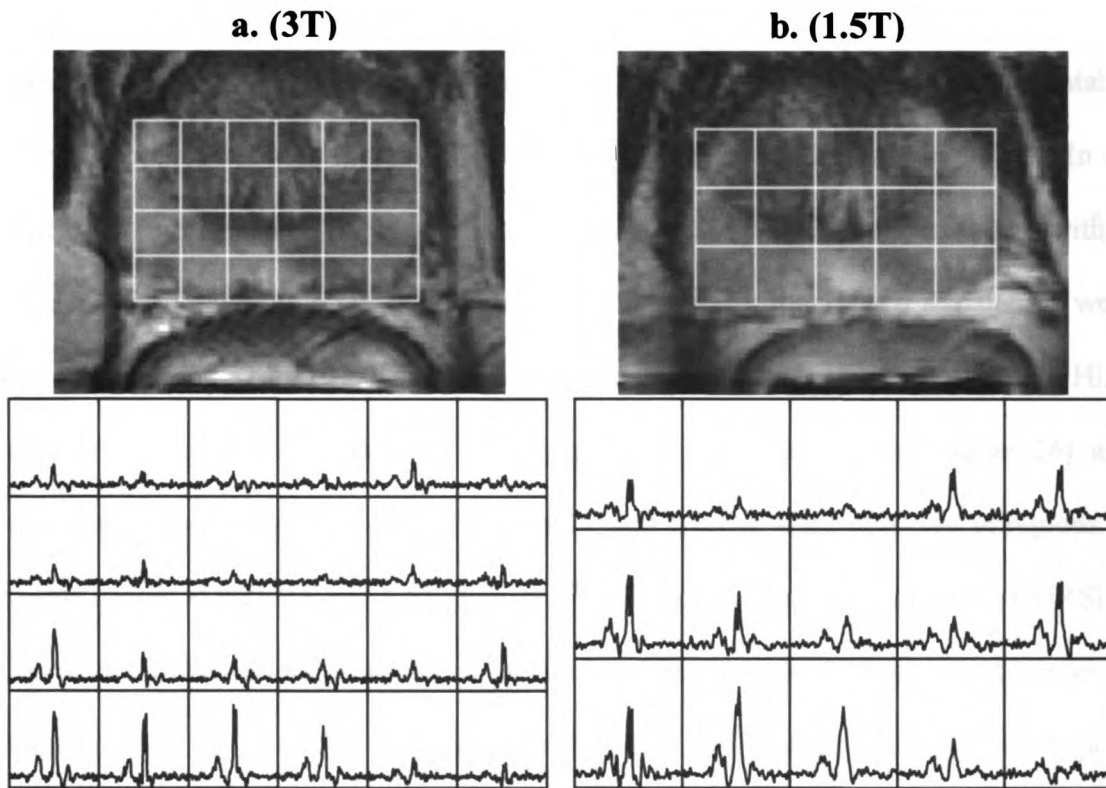


Figure 26. Sixty-eight years old prostate cancer patient with biopsy confirm cancer in right (3+3) and left (3+3) gland who underwent prostate MRI/MRSI exam at both 3T (a) and 1.5T (b). High levels of citrate were observed in the region of healthy prostate peripheral zone selected based on the lack of abnormalities on T2-weighted FSE images at both 3T and 1.5T. Note that higher spatial resolution was used for the 3T MRSI (0.157cc vs. 0.343cc) as compared to the 1.5T acquisition.

using a conventional PRESS sequence with dualband spectral spatial 180° pulses and an echo time of 90 ms selected to invert the citrate inner resonances, the outer resonances were out of phase and are significant (Figure 25a). However, using the MLEV-PRESS sequence at the minimum echo time of 85ms, the inner citrate resonances were maximally upright and the outer resonances were also upright and had minimum intensity (Figure 25b). Sufficient magnetic field homogeneity was attained to resolve the inner and outer lines of the citrate doublet of doublets. Average linewidth for water resonance was 12.5 Hz for the 3T MRSI studies. In all 3T studies acquired, spectral baselines were very flat due to the upright citrate peak, the robust attenuation of water, and the suppression of lipid resonances. No significant differences in spectral quality were observed between studies performed with rigid endorectal coils and studies performed with inflatable endorectal coil filled with Flutech_T14™. No patient discomfort was reported. In all studies, no biopsy changes were observed since the exams were performed with a sufficient time interval after the biopsies in all cases. Similar spectral patterns were observed from the 3T and 1.5T exams for the same patient see Figure(s) 26 and 27. High levels of citrate were observed in healthy prostatic peripheral zone (Figure 26) and elevated choline and reduced citrate, polyamine and creatine were observed in regions of prostate cancer at both 3T and 1.5T (Figure 27). The higher spatial resolution of MRSI at 3T provided improved delineation and metabolic characterization of individual tumors as compared to 1.5T. For the ten patients studied at both 3T at 1.5T, the 3T citrate peak height SNR with correction for the difference in voxel resolution was calculated to be 2.08 ± 0.34 (S.E.) fold higher than that of 1.5T. The gain in SNR from 1.5T to 3T was significant ($p = 0.04$). In addition to the SNR increase at 3T, the increase in resolution

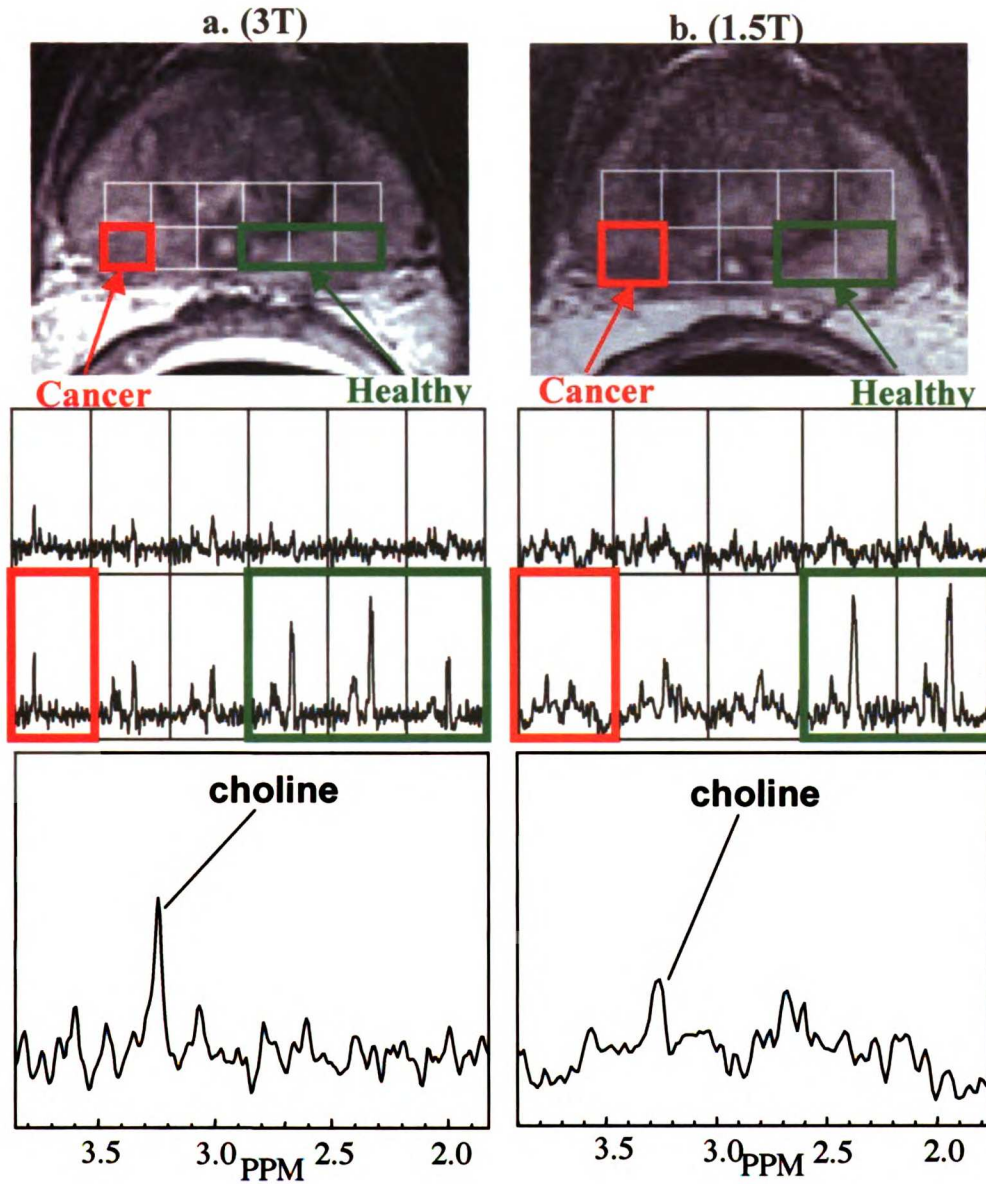


Figure 27: Seventy-one year old prostate cancer patient with biopsy proven cancer in the right gland (2+2) underwent MRI/MRSI exams at both 3T (a) and 1.5T (b). In concordance with the biopsy result, MRSI found voxels of elevated choline and reduced citrate in the right prostatic peripheral zone while citrate levels in the left peripheral zone remained high. The higher spatial resolution of MRSI at 3T (0.157cc vs 0.343cc) allowed better metabolic delineation of the small area of disease. The observed SNR of the elevated choline resonance is higher within a malignant voxel at 3T as compared to 1.5T due presumably to reduced partial volume effects.

from 1.5T to 3T was also evident in the MRSI data. The citrate doublet of doublets were

readily resolved at 3T with the separation of the central doublet often to 50% of the amplitude, and distinct peaks were observed for the overlapped resonances of choline,

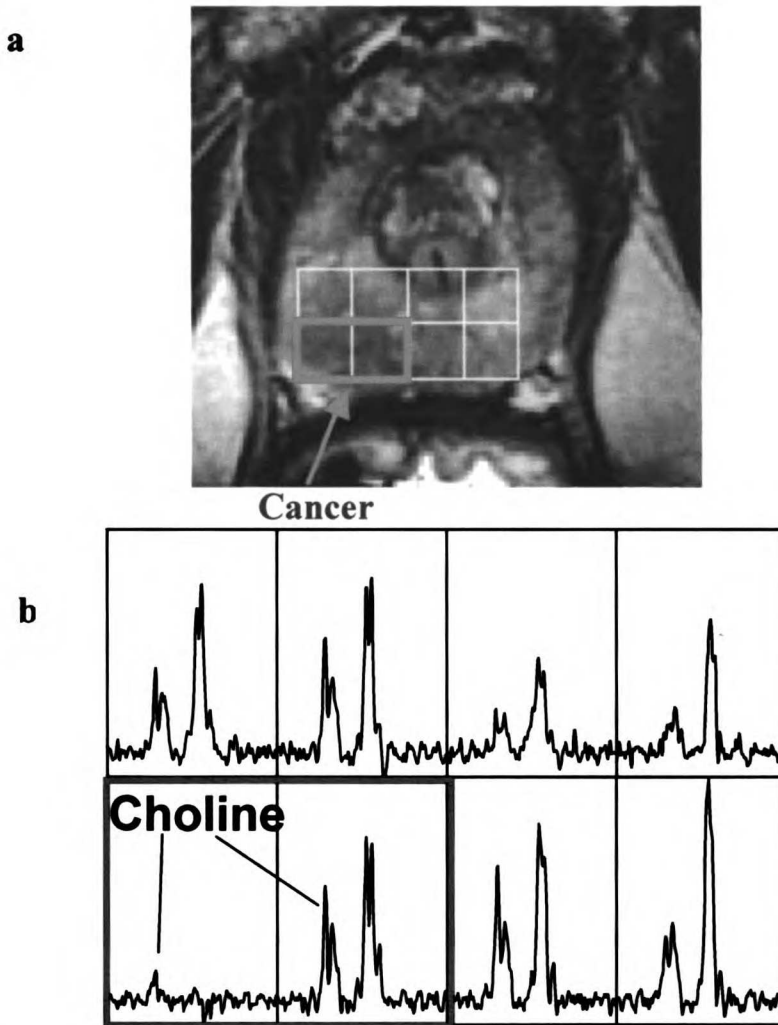


Figure 28. Sixty-five year old prostate cancer patient with biopsy confirmed prostate cancer (right lobe, G3+3). Elevated choline and reduced citrate were observed in the region of positive biopsy (b) for prostate cancer and that was suspicious for abnormality on the T2-weighted FSE images (a). High level of citrate was observed in the healthy prostate peripheral zone. With increased chemical shift dispersion and thus spectral resolution at 3T, changes in choline resonance were observed independently from changes in polyamine and creatine, allowing more accurate assessment of cancer extent and providing potentially more accurate metabolic information.

polyamine and creatine between 2.9 and 3.3 ppm (Figure 25 and 28). Due to the increased spectral resolution, the choline resonance could often be observed with minimal overlap from polyamine resonances (Figure 28).

The calculated T1 relaxation times of citrate and choline at 3T were 540 ± 140 ms and $961 \text{ms} \pm 250$ ms respectively. Due to the large voxel size used for the T1 studies, the B0 variation within the volume caused substantial line broadening, thus the polyamine resonance and creatine resonance were not sufficiently resolved for the measurement of their peak amplitude. Thus, the T1 relaxation times for these two metabolites were not calculated.

f. Discussions

The extension of MRSI methods to higher field strength poses a number of problems related to the design of RF pulses. The energy deposited by a given RF pulse is an order of magnitude higher at 3.0T compared with 1.5T [62], and the RF field is more inhomogeneous [63]. Another problem is that the resonant frequency of metabolites is twice that at 1.5T, so RF pulses with twice the spectral bandwidth are required, which typically have higher peak amplitude. This is of particular concern for MRSI of the prostate, where the whole-body RF coil is typically fully loaded and peak powers currently implemented at 1.5T are already at the limitations of the RF amplifier. Despite the afore-mentioned limitations, there are also great advantages for new RF pulse designs at 3T. With the higher resonance frequency, the time-bandwidth product (TB) available during excitation of a particular set of metabolites is doubled. Essentially the capital of

RF pulse design, the higher TB can be spent on spectral profiles with sharper edges, as well as the ability to control the spectral profile during the excitation process. Another important aspect in prostate MRSI localization is pre-saturating the tissue surrounding the region of interest to suppress contaminating signals, such as periprostatic lipid in prostate MRSI. The design of Very Selective Suppression (VSS) pulses uses quadratic phase across the excitation profile [64] to spread energy evenly across the RF pulse. This approach allows much sharper profiles than would be practical with conventional, linear-phase RF pulses. In addition to saturation, localization is further provided using the refocusing pulses of the PRESS sequence. Using multidimensional RF pulse design methods [55, 65-67], specialized RF pulses were used that refocus a slice, but only over a specified range of resonant frequencies[55, 68]. The use of these spectral-spatial pulses in MRSI has a number of advantages. Because water and/or lipid is simply not refocused, the suppression does not degrade with RF inhomogeneity, and is not effected by T1 and T2 relaxation [69]. Also, the spatial profile is not a function of frequency, unlike conventional slice selective pulses. That means that the spatial profile is identical for all metabolites and negates chemical shift misregistration effects which are major limitations for conventional excitation pulses especially at higher magnetic field.

Another major issue facing high field prostate MRSI is that the response of the strongly coupled AB spin system of citrate to conventional MRSI localization sequence such as PRESS changes with magnetic field strength. Thus the same modulation behavior at 1.5T does not occur at 3T. For fast and accurate quantification of citrate, it is beneficial for the doublet of doublets to have a completely positive absorptive pattern. However,

obtaining upright citrate resonances by going to longer echo times dramatically affects spectral SNR. For example, if the MRSI data were acquired with an echo time of 260 ms using the conventional PRESS sequence, the T2 relaxation signal loss would negate the SNR gain at 3T compared to 1.5T [37, 40]. Although inverted citrate peaks can be observed at a shorter echo time of 90 ms, the outer lines were out of phase with the inner lines making accurate quantification of the citrate difficult (Figure 25). With the MLEV-PRESS sequence, not only did citrate have a fully upright pattern at the echo time of 85 ms, but outer lines were also drastically reduced and the baseline was flat. Incorporation of the spectral-spatial pulses in the MLEV-PRESS sequence provided robust lipid suppression in all exams, which also facilitated quantitation of citrate resonances at 3T.

The SNR increase at 3T compared to 1.5T enabled the use of 2-fold higher spatial resolution for MRSI data acquisition at 3T in this study. The SNR comparison in this study did take into account the differences in resolution used at 3T and 1.5T and demonstrated a doubling in SNR at 3T. The 2.08 improvement in SNR calculated in this study is presumably due not only to the increase in field strength but also from several factors including the MLEV PRESS sequence, reduction in TE, increase in TR, optimized 3T coils and potentially reduced intravoxel dephasing and point-spread function differences due to the higher spatial resolution sampling used at 3T. The higher spatial resolution of the 3T MRSI data also provided better metabolic delineation of individual tumors and zonal anatomy compared to 1.5T. Reduction of partial volume effects provided clearer observation of elevated choline and thus improved metabolic characterization of smaller volumes of cancer (Figure 27).

There remain several obstacles to the acquisition of prostate MRSI data at 3T that need to be addressed. The longer T1 relaxation time of choline at 3T as compared to 1.5T indicates that longer repetition times may be required to reduce saturation effects. With the choline T1 being approximately 1s, at the TR of 1.3s used in this study, 27% of choline signal was lost due to saturation. With the increase in spatial resolution at 3T, a larger spatial encoding matrix may be required for sufficient coverage of larger prostate. The further increase in repetition time and phase encode matrix may result in prohibitively long scan times. There are a number of fast sampling strategies that could be used to acquire larger phase encode matrices using longer repetition times in a reasonable acquisition time [70-73], and these methods need to be considered for future studies.

In regions of healthy tissue at 1.5T, the choline, polyamine and creatine resonances typically overlap and are therefore quantified as a single peak. The ratio of [choline + polyamine + creatine] / citrate (cc/c) has commonly been used as a marker for prostate cancer, since it has been shown to be significantly higher in regions of prostate cancer relative to healthy peripheral zone tissues [35, 36, 57, 74]. This change is due both to increases in the choline resonance and decreases in citrate with cancer evolution and progression. It is also known that polyamines decrease in regions of cancer [75]. Due to the loss of polyamines in cancer, the choline resonance can often be resolved from creatine even at 1.5 T. However, since polyamines contribute to the numerator of the CC/C ratio, their reduction reduces the magnitude of change in the CC/C ratio with

cancer. At 3T, the choline and polyamine resonances show less overlap in healthy tissues and can often be baseline resolved from the creatine in regions of cancer (Figure 28). Based on the improved detection of elevated choline and the higher spatial resolution of the 3D MRSI data at 3T, this study suggests that the spatial extent of cancers could potentially be more accurately assessed as compared to 1.5T

In summary, the feasibility of acquiring high spatial and spectral resolution 3D MRSI data at 3T was demonstrated. By using an MLEV-PRESS sequence, completely upright citrate doublet of doublets with a flat baseline can be acquired at a reasonably short echo time of 85ms. Dualband spectral-spatial pulses provided robust lipid suppression in all studies. Approximately a two-fold increase in SNR was calculated at 3T compared to 1.5T in this study. By taking advantage of the SNR increase to acquire 3D MRSI data at a higher spatial resolution and the increase in spectral resolution, initial patient studies suggest that the accuracy of metabolic characterization by MRSI may be substantially improved at 3T.

Chapter 5: High Speed Prostate MRSI at 3T with Flyback Echo-Planar Encoding

One limitation of MR spectroscopic imaging is the time needed to acquire large volume 3D MRSI datasets when using conventional phase encoding in three directions to traverse k-space. With higher field MR systems such as 3T scanners becoming widely available and improved coil arrays providing increased SNR, MRSI data can be acquired with higher spatial resolution, as demonstrated in the last chapter. However, the scan time required for the acquisition of 3D high resolution MRSI data with adequate spatial coverage may be prohibitively long for clinical exams. Also, with increased SAR and longer T1 relaxation times at higher field, scan time may be further increased by the necessity of using longer repetition time (TR). New methods are required to overcome these challenges to reduce the scan time to the order of 10 minutes or less which would further improve the clinical utility of this technique. Also, the scan time saved may be used to incorporate other MR imaging techniques into the prostate MR exam such as T2-mapping, diffusion tensor imaging (DTI), dynamic contrast enhanced imaging (DCE). This chapter describes the research I conducted to develop new fast prostate MRSI methods and the initial testing that I carried out in prostate cancer patient studies.

A) Considerations for fast prostate MRSI acquisition

Approaches such as echo planar spectroscopic imaging (EPSI) and spiral SI have been applied to provide higher speed MRSI data acquisition[70, 73]. However, limitations such as timing error, eddy currents, susceptibility artifacts, low spectral bandwidth, and

difficult data reconstruction reduce the applicability of these techniques in the clinical setting. The flyback k -space trajectory has been shown to provide robust data acquisition with reduced flow and off resonance artifacts in cardiac imaging and insensitivities to timing errors and eddy currents in spectroscopic imaging [76, 77]. Flyback trajectories were designed and tested for high speed 3T prostate MRSI acquisition.

B) Trajectories designs and SNR efficiency for 3T prostate MRSI

The readout gradient for a flyback echo-planar trajectory consists of a flat segment during which data are acquired, followed by a rewind lobe that retraces across the desired portion of k -space as quickly as possible. The most efficient form of such a gradient consists of rewind lobes using the maximum slew rate of the gradient hardware, interleaved with flat portions that exactly cover the desired extent in k -space. The duration (and thus amplitude) of this flat part is determined by the desired spectral bandwidth (B_s), with $B_s = (T_f + T_r)^{-1}$, where T_f is the duration of the flat segment of the gradient, and T_r is the duration of the rewinder. Since data are not acquired during the rewind lobe of the flyback gradient, a penalty in SNR is incurred relative to the usual continuous sampling during the readout window. This reduced SNR efficiency, E_{snr} , expressed as the fraction of the full SNR that could be achieved during the same readout time, is given by $E_{\text{snr}} = (T_f / (T_f + T_r))^{1/2}$. Higher spatial resolution (longer T_r) and higher spectral bandwidth (shorter T_f) both imply a reduction in E_{snr} . For high spatial resolution scans, where signal averaging is often used to increase the SNR, interleaving of k -space trajectories can be used to boost the SNR efficiency [71]. For example, if two signal

averages are to be used, then the flyback trajectory can be designed for half of the desired B_s , increasing the SNR efficiency by increasing Tf . Then, during the second of the two data acquisitions, the readout gradient is shifted in time by $1/(2B_s)$, and the two acquisitions can be combined to regain the full B_s in the reconstructed data. For higher spatial resolution waveforms, interleaved acquisitions can have significant benefit.

Gradient waveforms were designed in MATLAB™. The gradient waveforms were designed to be optimal in the sense that the gradient is either flat (time during which data are acquired) or ramping at maximum at slew rate, 150 mT/m/ms.

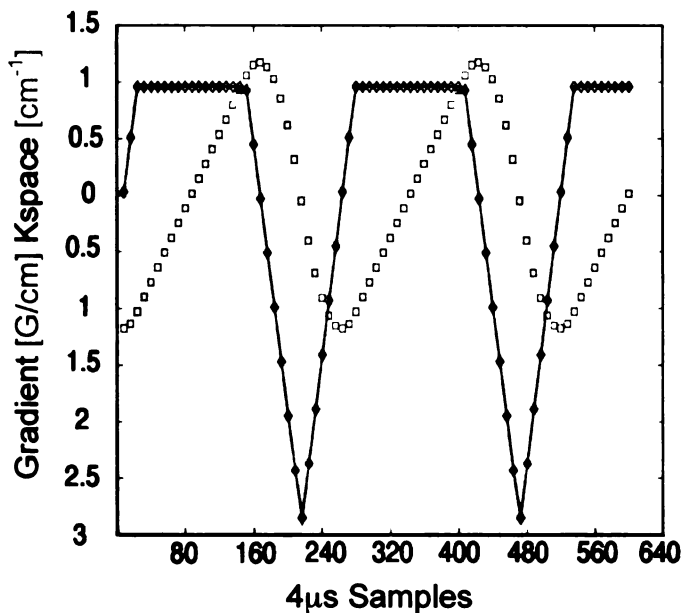


Figure 29. Flyback echo-planar readout trajectory designed for high speed prostate MRSI with high spatial and spectral resolution. The trajectory is designed for 976 spectral bandwidth, 4.9 mm minimum spatial resolution and SNR efficiency of 71%. With 16384 samples and 31250 Hz sampling rate per readout, sixteen spatial encoding steps are achieved.

Two flyback echo planar trajectories were designed specifically for 3T prostate MRSI and implemented on a 3T GE MR scanner. They were developed to provide up to 16-fold acceleration in k-space sampling. The first trajectory was designed for 976 Hz spectral bandwidth and 4.9 mm minimum spatial resolution (Figure 29). The gradient waveform uses maximum slew rate allowable by the system (150

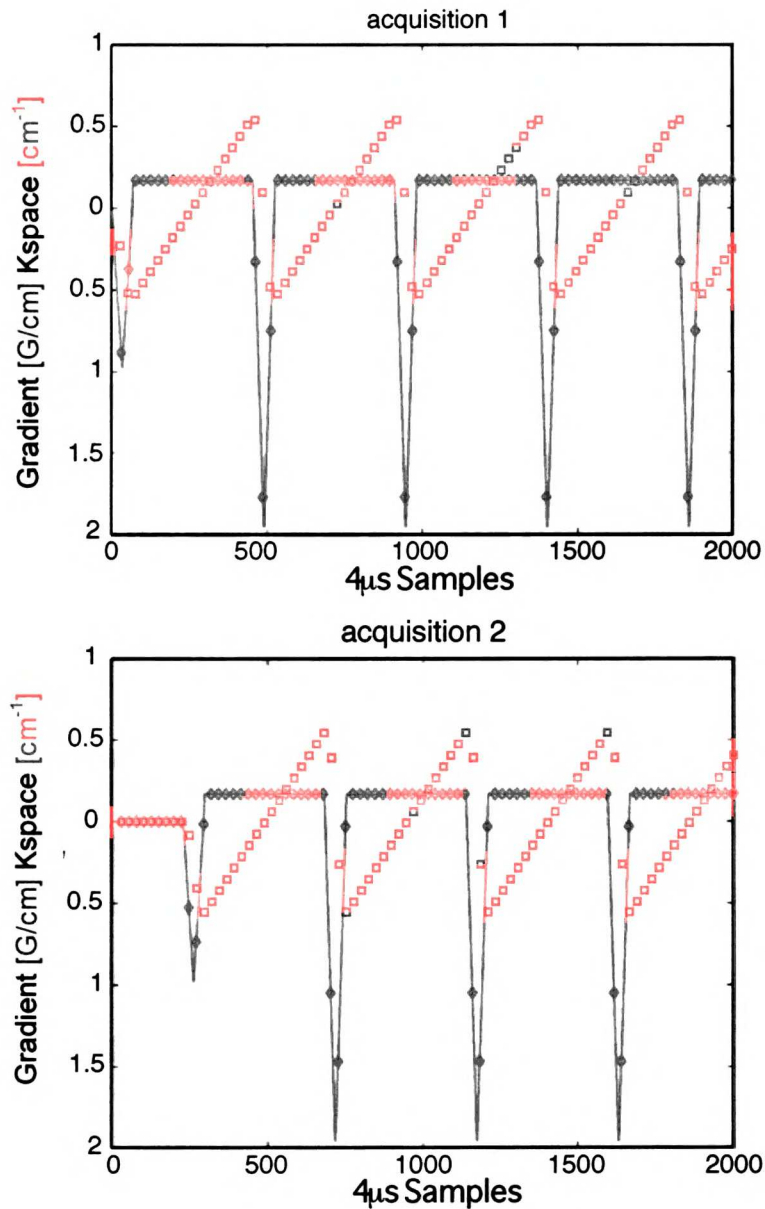


Figure 30. Flyback Echo-Planar gradient waveform designed for high speed MRSI acquisition with 5mm minimum spatial resolution and high efficiency (92%). Spectral bandwidth of the waveform is 506 Hz. With a two-acquisition scheme that involves a temporal interleave that shifts the gradient by $1/(2 \times \text{SBW})$ in the second acquisition as shown above, the two acquisitions can be combined to regain SBW of 1012 Hz. With 8208 samples and 9615 Hz sampling rate per readout, sixteen spatial encodes are achieved during readout.

mT/m/ms) at minimum spatial resolution. In this design, the readout lobe and the rewind

lobe have the same duration. Since data is not acquired during the rewind lobe, this

trajectory has a theoretical signal to noise efficiency of 71% [SNR efficiency = (time of readout lobe)/ (time of readout lobe + time of rewind lobe)]. With 16384 data samples at 31250 Hz sampling rate, sixteen spatial encoding is achieved per readout.

The second trajectory was designed for interleaved acquisition with 506 Hz spectral bandwidth and 5 mm minimum spatial resolution (Figure 30). The gradient waveform uses maximum slew rate allowable by the system (150 mT/m/ms) at minimum spatial resolution. In this design, the theoretical SNR efficiency is 92%. A two-acquisition scheme is employed for this trajectory, with the second acquisition shifted temporally by $1/(2B_s)$. Thus, when the two acquisitions are combined, the reconstructed data would have twice the spectral bandwidth (1012 Hz). With 8208 data samples at 9615 Hz sampling rate, sixteen spatial encodings are achieved per readout.

C) High speed MRSI of prostate with flyback echo-planar encoding

The two flyback echo-planar readout trajectories were incorporated into the new prostate MLEV-PRESS MRSI sequence described in the prior chapter and was applied in nine prostate cancer patient 3T research exams to acquire large array, high spatial and spectral resolution MRSI data in 8.5 minutes.

a. MRI/MRSI protocol

All studies were performed on a 3T GE Signa scanner (GE Healthcare Technologies, Waukesha, WI) using the body coil for excitation and a 3T Medrad prototype inflatable endorectal coil (Medrad, Pittsburgh, PA) filled with Flutech-T14TM (F2 Chemicals, UK) or a custom designed rigid coil in conjunction with pelvic phase array coil for signal reception. Flutech-T14 is a fully fluorinated, colorless, odorless, non-toxic fluid with a magnetic susceptibility similar to tissue and thus is an ideal substitute for air to inflate the endorectal coil.

All MRI/MRSI exams included the following imaging sequences. Sagittal fast spin echo (FSE) localizer images were acquired to check coil placement and to prescribe the subsequent imaging series. Oblique axial T2-weighted FSE images (TR/TE = 6000/102ms, 3mm slice thickness, no inter-slice skip, 12 cm FOV, 256 x 192 matrix, and no phase wrap) were obtained next. Oblique coronal T2-Weighted FSE images (TR/TE = 6000/102ms, 3mm slice thickness, no inter-slice skip, 14 cm FOV, 256 x 192 matrix, and no phase wrap) were acquired following the oblique axial FSE images. Axial T1-weighted SE images (TR/TE = 950/9ms, 5mm slice thickness, 1mm inter-slice skip, 24 cm FOV and 256 x 192 matrix) were also obtained.

A modified MLEV-PRESS sequence incorporating the first trajectory was applied in four prostate cancer patient exams. MRSI data was acquired with 16 x 16 x 8 phase encoding matrix using flyback echo planar readout in the Y-gradient direction (effective matrix: 16 x 16 x 8) and a nominal spatial resolution of 0.157 cc (5.4 mm per side). TE was 85 ms and TR was 2 s. Data acquisition time was 8.5 min with 2 NEX (8-fold acceleration).

The MLEV-PRESS sequence incorporating the second trajectory was applied in five prostate cancer patient exams. MRSI data was acquired with the same encoding matrix, spatial resolution, TE and TR as above. Data acquisition time was also 8.5 min for the two acquisition scheme with a temporal interleave in the second acquisition. MRSI data was also acquired using the MLEV-PRESS sequence with conventional phase encoding in all three gradient directions in all exams. A $12 \times 8 \times 8$ phase encoding matrix was used with the same TE, spatial resolution as described above except for a shorter TR of 1.3 s. Total acquisition time was 17 minutes.

b. Data analysis

All MRSI data were processed using custom processing software. The raw data acquired with the modified PRESS sequence incorporating the flyback echo planar readout trajectory were ordered as a 4D array with the first dimension being k-space values in the flyback direction, the second being time decay, the third being one phase encoding direction and the fourth being the other phase encoding direction. The k-space points in the flyback dimension corresponding to the constant gradient portion of the trajectory were selected out and the data set was reordered so that the time decay was the first dimension. The reordered dataset was then processed in the same manner as the conventional 4D MRSI dataset with the exception that the k-space points in the flyback dimension were each acquired at a slightly different time point [58]. This was then corrected during the standard 4D Fourier reconstruction using the fact that an origin shift in k-space is equivalent to a phase shift in the transformed domain. The total

reconstruction time on a standard UNIX workstation (Sun Microsystems Inc. Santa Clara, CA) was ~25 s for 3D MRSI data sets acquired with flyback echo planar trajectory.

c. Results

High quality, artifact free MRSI data were obtained from the prostate using a modified MLEV-PRESS sequence incorporating the flyback echo planar readout trajectories as

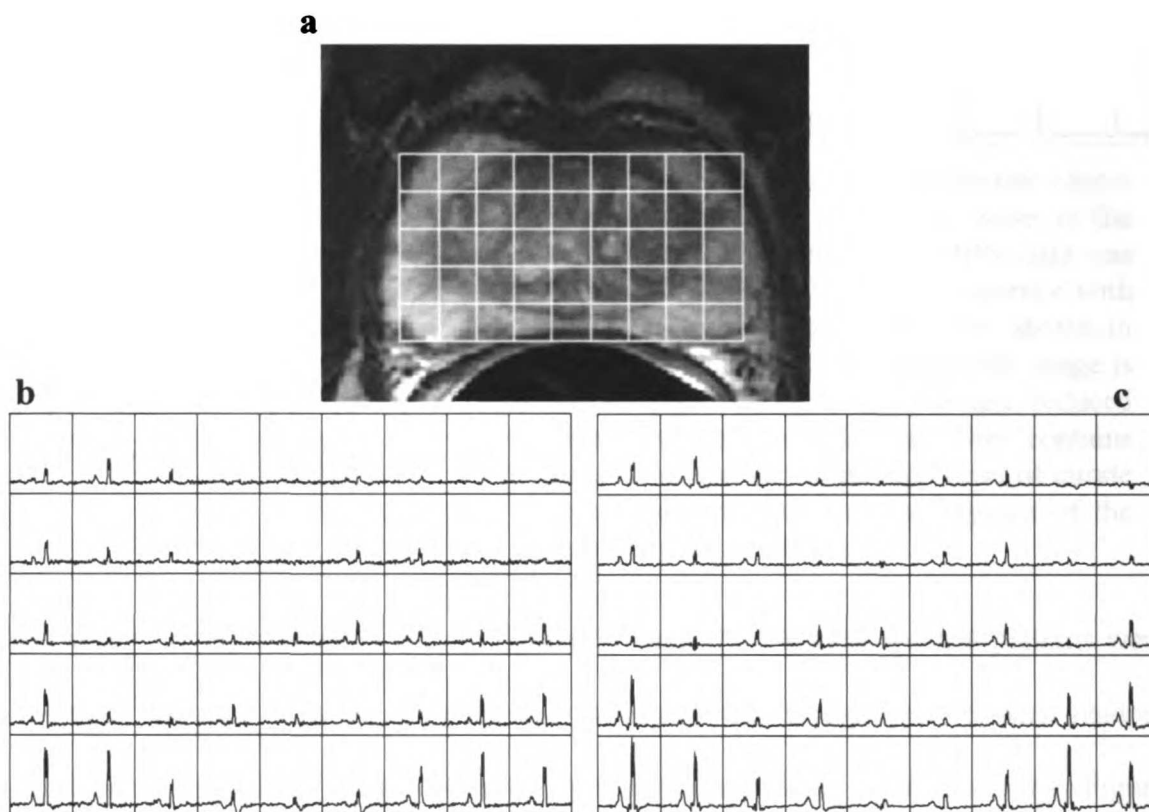


Figure 31. Seventy-three year old prostate cancer patient with biopsy confirmed cancer at unspecified location (G3+3). 3D-MRSI data were acquired with MLEV-PRESS sequence with both flyback echo-planar readout trajectory (b) and conventional phase encode (c). The flyback trajectory shown in Figure 29 was used with an effective matrix of $16 \times 16 \times 8$ (with flyback encoding on the second axis), 2s TR, 2 NEX and acquisition time of 8.5 min. A $12 \times 8 \times 8$ matrix was used for the conventional phase encode method with 1.3s TR, and acquisition time of 17.5 min. High quality, artifact free MRSI data were acquired with flyback echo-planar readout trajectory with identical spectral patterns as compared to data acquired with conventional phase encoding.

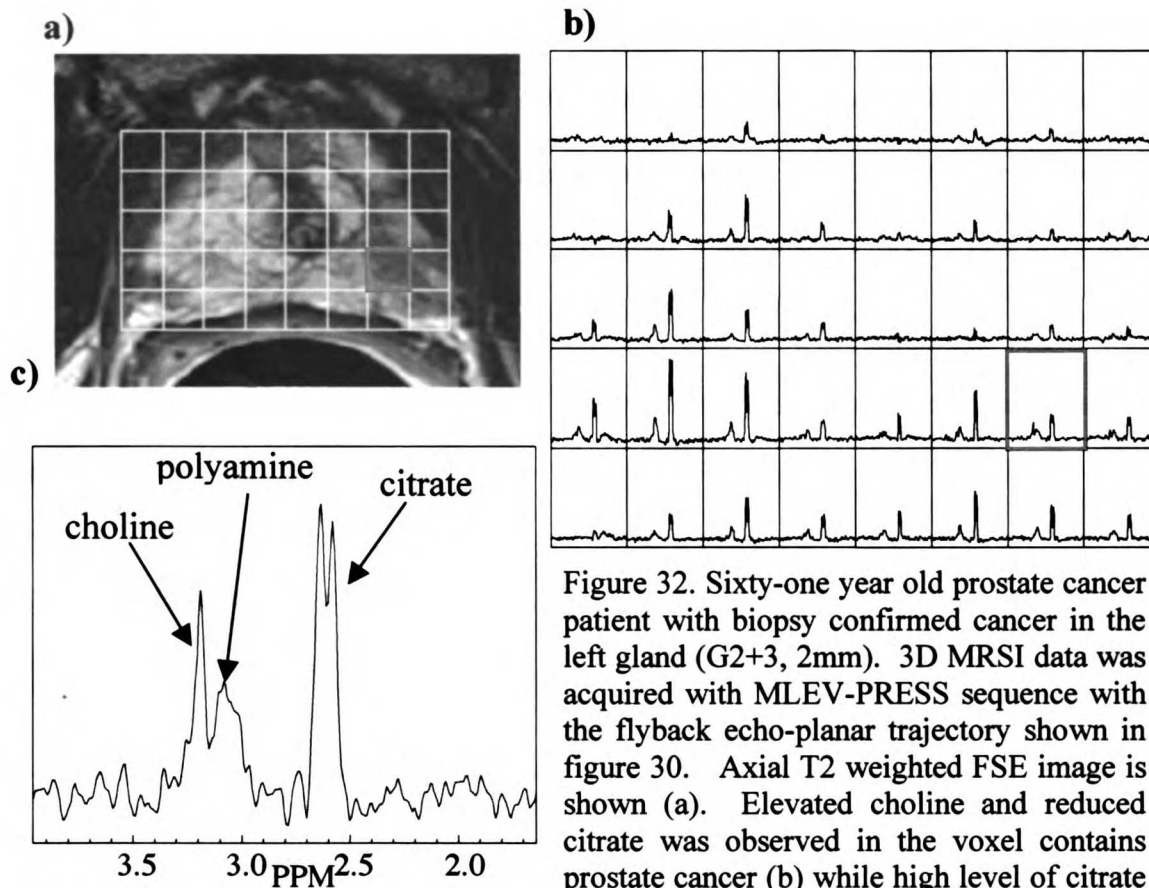


Figure 32. Sixty-one year old prostate cancer patient with biopsy confirmed cancer in the left gland (G2+3, 2mm). 3D MRSI data was acquired with MLEV-PRESS sequence with the flyback echo-planar trajectory shown in figure 30. Axial T2 weighted FSE image is shown (a). Elevated choline and reduced citrate was observed in the voxel contains prostate cancer (b) while high level of citrate was observed in the healthy regions of the prostate peripheral zone (c).

shown by the representative data in figures 31 and 32. Identical spectral patterns were observed for data acquired with the new sequence that incorporated flyback readout trajectory as compared to data acquired by using conventional phase encoding (Figure 31). The SNR lost due to data not being acquired during the rewind portion of the flyback trajectory and the shortened acquisition time did not affect the interpretability of the spectra. High levels of citrate and polyamines were observed in regions of normal prostate peripheral zone and reduced citrate and polyamine and elevated choline were found in regions of prostate cancer (Figure 32).

Table 1a summarized the SNR comparison between MRSI data acquired with the flyback echo planar readout trajectory shown in figure 29 and conventional phase encoding. The average SNR efficiency was 11% lower than that predicted in theory, based on the design of the trajectory (59% vs 71%). Table 1b summarized the SNR comparison between MRSI data acquired with the flyback echo planar readout trajectory shown in figure 30

Table 1
SNR comparison between flyback echo-planar readout and conventional phase encoding

1a. First flyback trajectory (Figure 29.)

Patient	phase encoding SNR	Flyback Echo Planar SNR	Apparent Efficiency	SNR
1	17.07	5.52	0.56	
2	33.55	10.63	0.55	
3	22.29	8.54	0.66	
4	9.79	3.50	0.62	

1b. Second flyback trajectory with interleaved acquisition (Figure 30.)

Patient	phase encoding SNR	Flyback Echo Planar SNR	Apparent Efficiency	SNR
1	11.08	5.18	0.81	
2	34.41	16.53	0.83	
3	16.55	6.96	0.73	
4	18.19	7.37	0.70	
5	35.76	16.71	0.81	

and conventional phase encoding. The average SNR efficiency was 11% lower than the theoretical SNR efficiency for this trajectory (80% vs 91%).

d. Discussions

One of the major obstacles of incorporating MRSI in a clinical prostate MRI exam is the acquisition time required to acquire large volume 3D spectral data sets using conventional phase encoding in all three dimensions especially at the high spatial resolutions offered by 3T. With a $12 \times 8 \times 8$ phase encoding matrix and a repetition time of 1.3 s, the acquisition of a prostate 3D MRSI data set requires 17.5 minutes [78]. At a nominal spatial resolution of 1.57 cc (5.4 mm isotropic voxels), the field of view (FOV) for this acquisition is only 64.8 mm x 43.2 mm x 43.2 mm. For larger prostates, either a larger voxel size or larger phase encoding matrix needs to be used. Increased voxel size is not desirable since it would increase partial volume effects and decrease the sensitivity of this technique for detecting small cancers. Increased phase encoding matrix sizes may cause the scan time for the exam to be undesirably long. In addition, as shown by prior studies, the T1 relaxation time of prostatic choline is approximately 1 s at 3T [44, 78]. Repetition times of 0.65 s - 1.3 s typically employed at 3T are not sufficiently long to avoid saturation of the choline signal and thus may reduce the ability of MRSI to detect increased choline levels in regions of cancer [43, 44, 78]. Therefore, faster k-space sampling is clearly needed to further improve the robustness and usefulness of 3T prostate MRSI without making compromises in spatial resolution, sensitivity, or patient tolerance.

Although the utilization of time varying gradients during readout to encode spatial information for high speed MRSI acquisition has been demonstrated previously, routine use of this approach has not been realized in clinical settings due to limitations such as timing error, eddy currents, susceptibility artifacts, low spectral bandwidth, and difficult data reconstruction. One of the advantages of flyback echo-planar trajectory is the insensitivity to time error and eddy currents effects [76, 77]. With the improvement of the gradient hardware, high spectral bandwidth flyback readout is now achievable on clinical scanners. The simple reconstruction process also makes it suitable as a routine clinical tool.

High quality prostate MRSI data was demonstrated in this study with the implementation of both readout trajectories. However, the SNR penalty observed was 10% more than theoretically expected, but was consistent with previous publications using flyback echo-planar acquisition. This small additional loss is not fully understood but may be due to imperfect gradient coils and/or gradient instabilities near the maximum slew rates used.

Chapter 6: Diffusion tensor imaging of prostate cancer

With the advent of hardware and software capable of acquiring single shot images, diffusion-weighted MR imaging has become not only feasible but also a widely-used and powerful research and clinical imaging technique [6, 79-82]. Diffusion-weighted imaging is sensitive to the motion of water molecules at microscopic spatial scales within biological tissues. Diffusion tensor imaging involves making diffusion measurements in at least six non-collinear directions, which allows for a more complete description of the 3-dimensional spatial distribution of water diffusion than was possible with older diffusion-weighted imaging techniques [79]. From the diffusion tensor, rotationally-invariant measures of the apparent diffusion coefficient ($\langle D \rangle$) and fractional anisotropy (FA) can be derived at each MR imaging voxel. These scalar parameters derived from DTI are sensitive to microstructural properties of biological tissues. In this research described in this chapter, I applied novel DTI methods for the study of prostate cancer microstructure.

A) DTI of the prostate with DTI-SSFSE and DTI-EPI sequences

Diffusion tensor imaging has been applied extensively in the human brain to study cellular swelling, axonal organization and other aspects of tissue microstructure which can change in a variety of brain pathologies. Recent studies have also demonstrated the benefit of DTI in the study of human brain tumors and other cancers [80, 83-86]. Although the vast majority of studies have focused on the brain, changes in tissue

organization and microstructure occur in other organ systems as well. One of the main reasons that diffusion MRI has not been widely applied outside of the brain is that echo-planar imaging (EPI) typically used in diffusion weighted imaging, provides poor quality images for body applications due to susceptibility-induced spatial distortions and poor lipid suppression. Even when the spatial distortions are relatively minor, they can prevent accurate correlations of DTI values with anatomic locations depicted on other imaging methods or the location of tissue biopsies etc. To address this problem, diffusion MRI sequence based on single-shot fast spin echo (SSFSE also known as HASTE) which utilizes rf refocusing in its echo-train and thus is resistant to the spatial distortions, eddy current effects and lipid artifacts that hinder EPI, has been investigated [30, 87-89]. Our

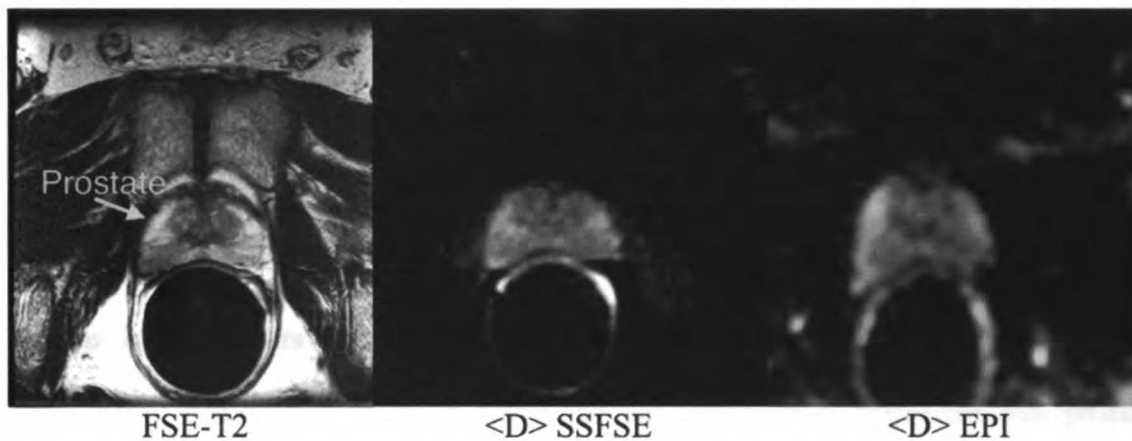


Figure 33. Comparison of conventional FSE images (left) with $\langle D \rangle$ (mean diffusivity) images acquired with DTI-SSFSE (middle) and DTI-EPI (right). The SSFSE-DTI images were acquired approximately the same image location as the FSE and with the following parameters: FOV=24cm, 256x128, slice thickness=4mm, 62KHz bandwidth, $b=0 + 600$, 6-gradient directions, single-shot (sub-second), with 4 repetitions. The DTI-EPI images were acquired from the same slice locations as the DTI-SSFSE with FOV=24cm, 256x128, slice thickness=4mm, 200KHz bandwidth, $b=0 + 600$, 6-gradient directions, single-shot (sub-second), with 4 repetitions. Note the negligible spatial distortions and excellent image quality in the SSFSE-DTI that permit accurate spatial correlations with the MR images.

initial studies in the brain and phantoms demonstrate virtually no spatial distortions and that the DTI parameter measurements were accurate with the variance as a percentage of the mean equal to or lower than for EPI [87]. The signal-to-noise ratio for DW-SSFSE is somewhat less than for EPI and, due to longer echo-spacings, is more susceptible to T2-blurring, but these effects can potentially be reduced by utilizing non-CPMG [89] and parallel imaging acquisitions such as SENSE [31, 90-92].

The initial feasibility study showed DTI-EPI to be extremely problematic compared to DTI-SSFSE (figure 33). Data acquired with DTI-SSFSE demonstrated negligible spatial distortions and excellent image quality providing accurate spatial correlations with the anatomical MR images and MRSI data (not shown).

B) Diffusion tensor imaging studies of untreated prostate cancer patients

a. Hypothesis

Unlike other tumors that demonstrate increased diffusivity ($\langle D \rangle$) compared to surrounding benign tissues, prior study and our initial study suggested that prostate

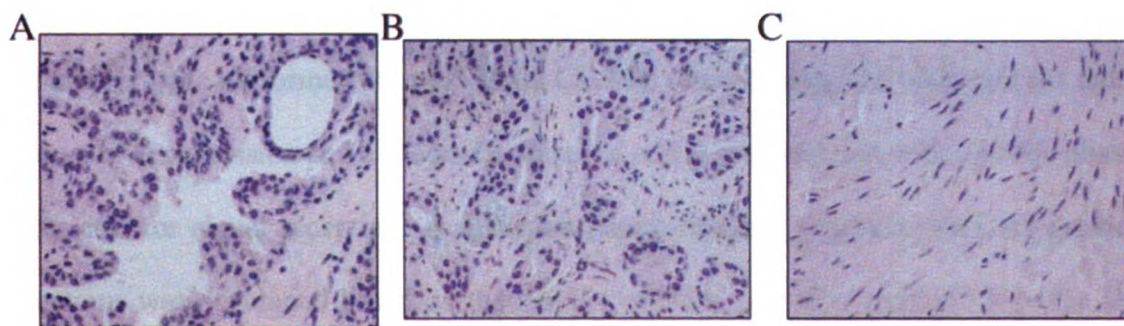


Figure 34. H&E staining patterns of excised prostate tissue samples containing predominantly healthy glandular tissue (A), Gleason 3+3 prostate cancer (B) and predominantly benign stromal tissue (C).

cancers demonstrate lower $\langle D \rangle$ values [6, 88]. This decrease in $\langle D \rangle$ is primarily due to the loss of normal ductal architecture that occurs with prostate cancer. The water in these ducts have T_2 's and $\langle D \rangle$ that approach that of free water. Instead of uniformly large acini with convolutions regularly distributed in a nodular pattern, and each gland surrounded by a delicate basement membrane (Figure 34A). In prostate cancer (Figure 34B), the disturbances in tissue architecture are manifested as small acini closely packed together, large acini without convolutions, large and small acini side by side, fused glands, or no glands [9, 93]. Gleason has correlated the degree of disturbance in tissue architecture from normal with cancer aggressiveness and patient outcomes [9]. It is for this reason, we hypothesize that $\langle D \rangle$ values will be inversely proportional with the pathologic grade of cancer with higher grade cancers having lower $\langle D \rangle$ values.

The first patient studies were focused on determining if there were significant differences in DTI values between normal peripheral zone tissues and histologically-confirmed cancers in untreated patients. In this study, 16 patients with biopsy-proven cancer were studied with MRI/MRSI and DTI-SSFSE.

b. MRI/MRSI/DTI protocol

All studies were performed on a 1.5 Tesla GE MR scanner using the body coil for radio-frequency transmission and a Medrad endorectal coil in combination with a pelvic phased array coil for signal reception. A diffusion tensor imaging sequence with six gradient directions was developed based on the single-shot fast-spin-echo method [30]. The DTI SSFSE imaging was acquired in 2.5 minutes in the axial plane with a FOV=24cm,

128x256 matrix, 1.8x0.9mm in-plane resolution, 4mm slices, rbw=62.5Khz, b-value=600, TE=67ms, with typically 7-9 slices covering the prostate. The DTI SSFSE was added to 32 MRI/MRSI prostate cancer exams consisting of FSE sagittal scouts, T1 axial SE images covering to the aortic bifurcation, fast spin echo T2 axial and coronal high resolution images, and 3D MRSI data acquired with a spatial resolution of 0.3cc (7mm per side). All data was analyzed off-line using software developed at our institution. Directionally averaged diffusion coefficient $\langle D \rangle$ and fractional anisotropy (FA) images were calculated and compared to the MRI/MRSI data. In 16 untreated patients with histologic-biopsy confirmation, DTI parameters were calculated for regions where the pathology findings, the MRI and MRSI data were all positive for cancer and for normal regions.

c. Data Analysis:

Using DTI processing software developed in-house, parametric maps will be generated for five rotationally invariant DTI parameters: the directionally-averaged diffusion coefficient ($\langle D \rangle$), fractional anisotropy (FA), and the maximum, intermediate, and minimum eigenvalues (λ_1 , λ_2 , and λ_3 , respectively) and their associated eigenvectors, based on the methods proposed by Basser and Pierpaoli [79]. The eigenvalues (or principal diffusivities) of the diffusion tensor characterize the magnitude or rate of water diffusion along each of the 3 principal axes of the diffusion tensor ellipsoid, given in mm^2/s . The direction of each of these 3 principal axes in 3D space is given by the eigenvectors. The mean diffusivity $\langle D \rangle$ (in mm^2/s), will be calculated using the formula:

$$D_{av} = \frac{\lambda_1 + \lambda_2 + \lambda_3}{3}$$

Fractional Anisotropy (FA), a dimensionless measure of anisotropy, expresses the fraction of the magnitude of the diffusion tensor attributable to anisotropic diffusion and will be calculated using the formula:

$$FA = \frac{\sqrt{\frac{3}{2} \frac{\sum_{i=1}^3 (\lambda_i - D_{av})^2}{\lambda_1^2 + \lambda_2^2 + \lambda_3^2}}}{\sqrt{2} \sqrt{\lambda_1^2 + \lambda_2^2 + \lambda_3^2}} = \frac{\sqrt{(\lambda_1 - \lambda_2)^2 + (\lambda_2 - \lambda_3)^2 + (\lambda_3 - \lambda_1)^2}}{\sqrt{2} \sqrt{\lambda_1^2 + \lambda_2^2 + \lambda_3^2}}$$

For isotropic diffusion ($\lambda_1 = \lambda_2 = \lambda_3$), FA is zero, and in the case where there is a strongly preferred direction of diffusion ($\lambda_1 \gg \lambda_2 \geq \lambda_3$), FA approaches one.

Paired measurements were obtained from healthy and cancer areas of the peripheral zone of the prostate for each patient. The t statistic for matched pairs was calculated to compare the mean difference in for $\langle D \rangle$, RA and the CC/C ratio between the two types of tissue.

d. Results and discussions

The DTI SSFSE sequence was incorporated into our research MRI/MRSI prostate cancer exam and provided $\langle D \rangle$ and anisotropy maps with minimal spatial distortions that could be easily referenced to the MRI and MRSI data. The $\langle D \rangle$ images showed image

intensity changes with both zonal anatomy and pathology (Figure 35). In the 16 pre-therapy prostate cancer patients with histologic biopsy confirmation (Table 2), the mean $\langle D \rangle$'s in the regions of cancer were $0.99 (x10^{-3} \text{mm}^2/\text{s})$, (sd = 0.28, range = 0.62-1.52)

Table 2. Diffusion and MRS data of Untreated Prostate Cancer Patients.

Patients	Gleason	PSA	<D>		FA		cc/c		<D>	FA
			C	H	C	H	C	H	C/H	C/H
1	3+3	15.9	1.24	1.51	0.12	0.1	4	0.4	0.82	1.27
2	3+4	5.2	1.15	2.22	0.3	0.09	0.8	0.2	0.52	3.55
3	3+3	7.3	1.06	1.81	0.23	0.18	0.9	0.3	0.58	1.28
4	3+3	3.3	1.03	1.25	0.12	0.12	0.7	0.3	0.82	1.03
5	3+3	4.8	0.82	1.11	0.18	0.15	1.1	0.2	0.74	1.24
6	3+3	6	0.85	1.34	0.18	0.14	2.2	0.3	0.63	1.28
7	3+2	6.4	1.36	1.64	0.18	0.14	1	0.3	0.83	1.33
8	3+3	11.7	1.52	1.94	0.29	0.17	0.8	0.1	0.79	1.7
9	3+3	1.9	0.62	0.84	0.17	0.14	0.9	0.2	0.74	1.18
10	3+3	6.4	0.93	1.08	0.24	0.16	1.5	0.2	0.86	1.5
11	3+3	4.4	0.72	1.16	0.22	0.15	1.2	0.3	0.62	1.48
12	3+3	6.3	0.66	0.91	0.32	0.17	0.8	0.1	0.73	1.87
13	3+3	2.1	1.08	1.56	0.23	0.17	1.6	0.3	0.69	1.33
14	3+3	11	1.38	1.58	0.18	0.18	5.5	0.3	0.88	0.98
15	3+3	4.6	0.71	0.85	0.25	0.12	0.8	0.3	0.83	2.12
16	3+3	3.8	0.75	0.88	0.26	0.24	1	0.3	0.85	1.1
Mean			0.99	1.35	0.217	0.15	1.55	0.26	0.75	1.52
sd			0.28	0.42	0.06	0.037	1.34	0.08	0.11	0.62
p =			0.00004		0.0004		0.0012			

and in healthy peripheral zone were 1.35 ± 0.42 (range = 0.85-2.22) ($\times 10^{-3} \text{mm}^2/\text{s}$). These values were significantly different ($p = 0.00004$). The mean fractional anisotropy (FA) values were 0.217 ± 0.06 in cancer regions and 0.150 ± 0.037 in normal peripheral zone and also were significantly different ($p = 0.0004$). Although between patients some

overlap in $\langle D \rangle$ and relative anisotropy values was observed in regions of cancer and normal tissues, within the same patient $\langle D \rangle$ values were always lower in cancer than in normal regions.

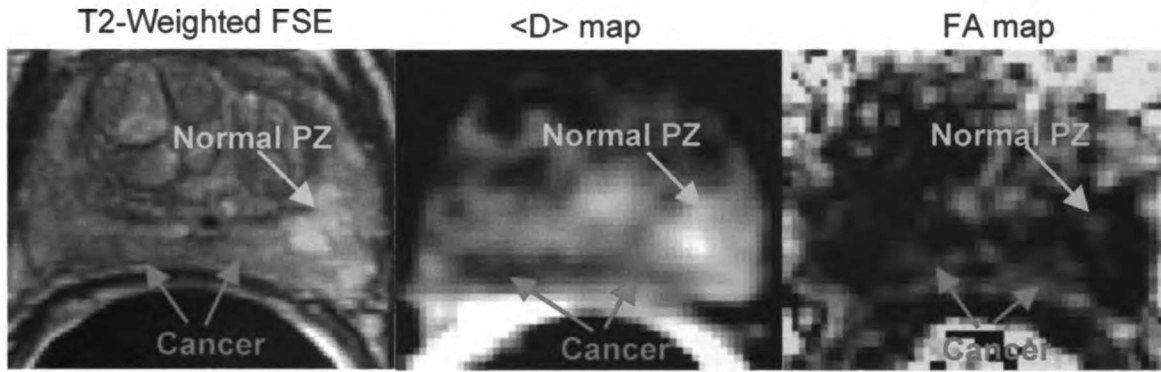


Figure 35. In this untreated patient, a large region of cancer was confirmed by biopsy and seen as an area of reduced $\langle D \rangle$ and elevated FA as compared to healthy peripheral zone. FA in stromal regions of the central gland was even higher than for the cancer.

A correlation was also observed between MRSI data and DTI data (figure 36). The reduction of $\langle D \rangle$ in region of prostate cancer relative to region of benign prostatic tissue corresponds to an increase in CC/C ratio. As expected, the lost of ductal morphology in the region of cancer not only cause the reduction of citrate (high CC/C ratio), but also the average diffusivity in that region. In the region of healthy prostate peripheral zone, the high level of citrate accumulated in the large prostatic ducts (low CC/C ratio) was observed along with the higher diffusion values.

The preliminary study described in this chapter demonstrated the value of DTI-SSFSE sequence to obtain $\langle D \rangle$ and anisotropy maps of human prostate. Significant differences in both $\langle D \rangle$ and anisotropy were observed between biopsy-confirmed cancer and normal peripheral zone. However, the anisotropy measurements are very low and near the noise

threshold and thus may not truly reflect differences in the orientation of restricted water diffusion. Better coil design or higher magnetic field may help increase the SNR of the prostate DTI to better measure the change in anisotropy between prostate cancer and normal prostatic tissues.

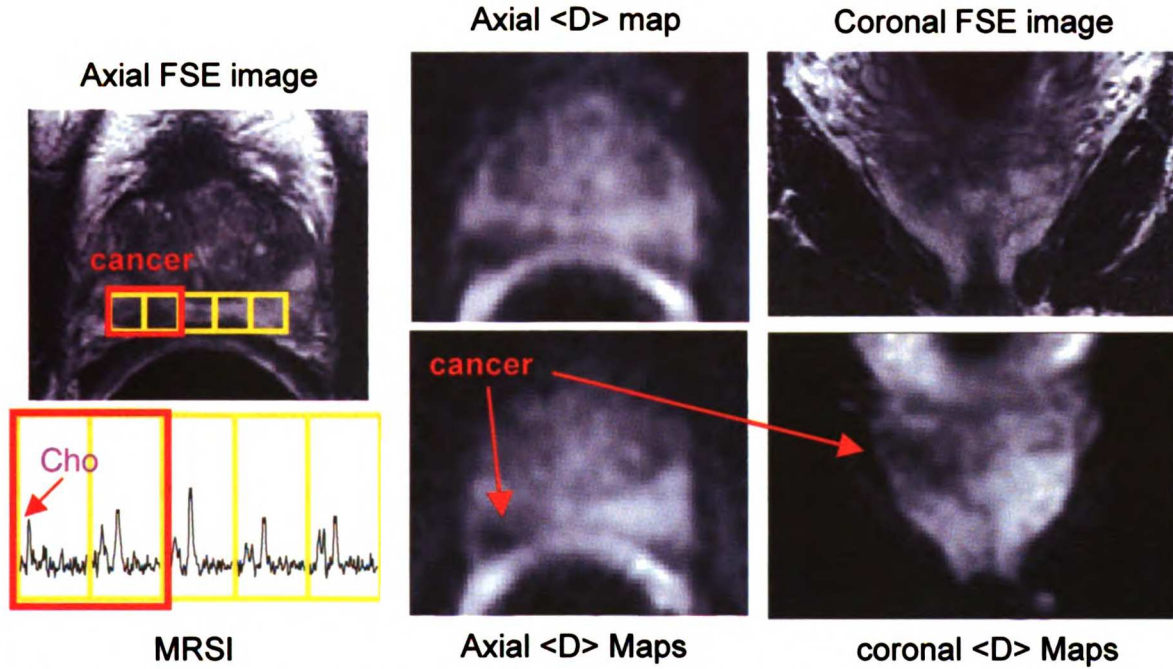


Figure 36. Detection of reduced $\langle D \rangle$ in the region of biopsy-confirmed cancer corresponded with reduced FSE-T2 signal intensity and elevated choline, reduced citrate on MRSI.

To truly assess the ability of DTI to characterize prostate cancer *in vivo*, it will be necessary to conduct DTI studies in pre-prostatectomy patient MR exams and subsequently correlate DTI parameters to step-section histology.

C) Diffusion tensor imaging studies of post-therapy prostate cancer patients

For post hormone/radiation therapy patients, residual/recurrent cancer is often poorly delineated on anatomic MRI. The studies described above have demonstrated the ability of diffusion MRI to detect difference in cell structure and organization between cancer and normal prostatic tissue. The initial findings using DTI-SSFSE showed significantly reduced $\langle D \rangle$ and a small yet significant increase in anisotropy in regions of cancer as compared to normal peripheral zone in patients with histologically confirmed cancer prior to therapy. In this section, the utility of DTI in post-therapy prostate cancer patients was investigated.

a. MRI/MRSI protocol

All studies were performed on a 1.5 Tesla MR scanner (Signa; GE Medical System) using the body coil for RF transmission and a disposable endorectal coil (Medrad, Pittsburgh, PA) in combination with a pelvic phased array coil for signal reception. A diffusion tensor imaging sequence with six gradient directions based on the single-shot fast-spin-echo method described by Alsop [30] was used. The DTI SSFSE imaging was acquired in 2.5 minutes in the axial plane with a FOV=24cm, 128x256 matrix, 1.8x0.9mm in-plane resolution, 4mm slices, rbw=62.5Khz, b-value=600, TE=67ms, with typically 7-9 slices covering the prostate. The DTI SSFSE acquisition was added to 33 MRI/MRSI exams of post-therapy prostate cancer patients. The total MR protocol consisted of FSE sagittal scouts, T1 axial SE images covering to the aortic bifurcation, fast spin echo T2 axial and coronal high resolution images, and 3D MRSI data acquired with a spatial resolution of 0.3cc (7mm per side).

All data was analyzed off-line using software developed at our institution. $\langle D \rangle$ and fractional anisotropy images were calculated and compared to the MRI/MRSI data. In 26 post hormone (n = 14) and radiation-therapy patients (n = 12), DTI parameters were calculated for regions where MRSI data were positive for recurrent/residual cancer and for benign prostatic tissues. In 15 post radiation-therapy patients with metabolic atrophy throughout the gland, DTI parameters were also calculated to investigate diffusion values in atrophic tissues post-therapy.

b. Results

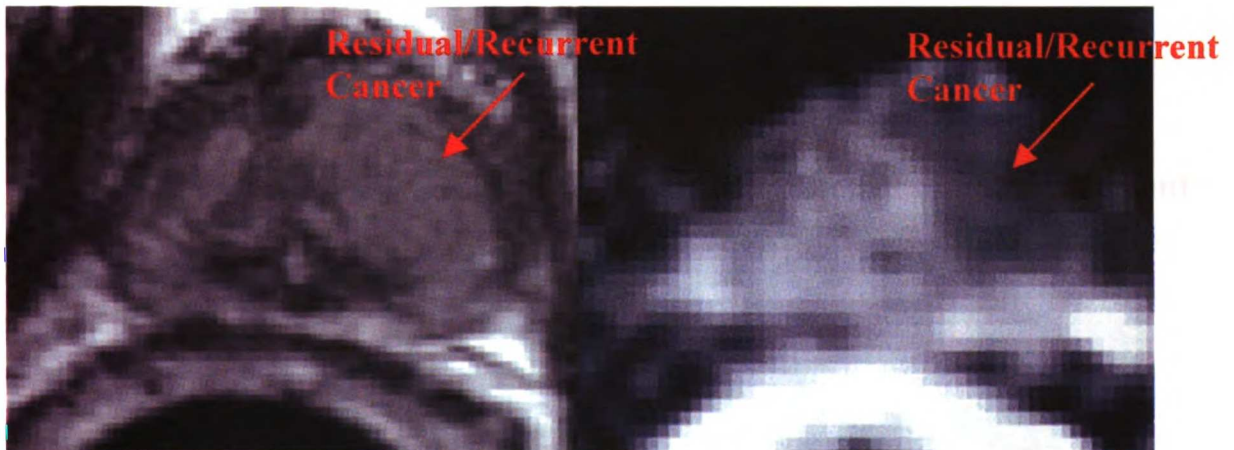


Figure 37. T2-weighted MRI (left) and $\langle D \rangle$ map (right) following hormone ablation therapy. Despite rather uniform T2 appearance, $\langle D \rangle$ is decreased in region of cancer.

Following hormone ablation or radiation therapy, it often becomes difficult on MRI to differentiate cancer from benign prostatic tissues. However, in this study, significant decreases in cancer $\langle D \rangle$ values were observed (Figures 37, 38). In 26 post-therapy patients with histology and/or MRSI data indicating recurrent/residual cancer in the peripheral zone, the mean $\langle D \rangle$'s in the regions of cancer were 1.29 ± 0.26 ($10^{-3} \text{mm}^2/\text{s}$), (range = 0.81-1.73), and in benign regions were 1.53 ± 0.25 (range = 0.91-1.83). They

were significantly different ($p=0.00003$). These $\langle D \rangle$ values were both substantially higher than were measured in our prior study of cancer and benign prostatic regions in untreated patients [88]. The mean fractional anisotropy values were 0.26 ± 0.08 in cancer region and 0.18 ± 0.05 in non-cancer region and were significantly different ($p = 0.0001$). However, these anisotropy measurements are very low and near the noise threshold and thus may not truly reflect differences in the orientation of restricted water diffusion.

In 15 post-therapy patients with metabolic atrophy throughout the prostate gland, the mean $\langle D \rangle$ in these atrophic regions was 1.48 ± 0.22 which was significantly higher ($p =$

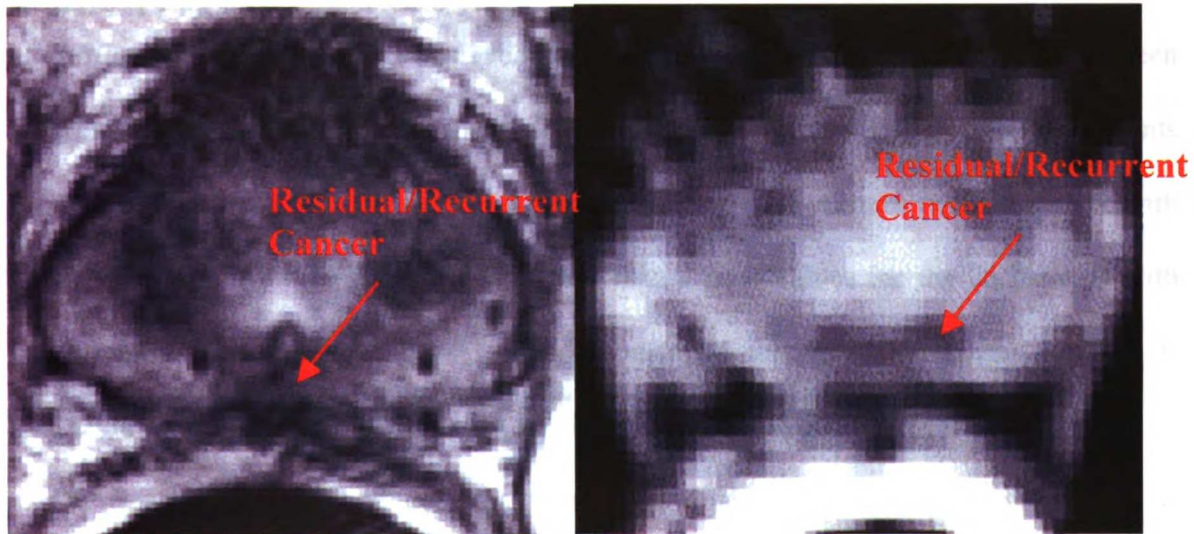


Figure 38. T2-weighted MRI (left) and $\langle D \rangle$ map (right) following brachy therapy. Cancer was poorly depicted in the anatomic MRI but was clearly delineated in the $\langle D \rangle$ image.

0.003) than the $\langle D \rangle$'s in the regions of cancer in the 26 post-therapy patients with recurrent/residual cancer.

c. Discussion

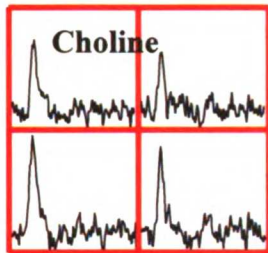


Figure 39. Post radiation therapy patient with residual/recurrent cancer. While the T2-weighted anatomical image did not show significant contrast between the residual/recurrent disease, MRSI and DTI demonstrated elevated choline and reduced $\langle D \rangle$. Note also that the DTI offered better much improved spatial resolution than MRSI.

Significant differences were observed in both $\langle D \rangle$ and fractional anisotropy between regions of residual/recurrent cancer and benign prostate peripheral zone in patients following hormone and/or radiation therapy. Also, $\langle D \rangle$ values in 15 patients with metabolic atrophy were significantly higher than cancer values for the 26 patients with recurrent/residual disease. This study demonstrated that diffusion tensor imaging is valuable in post-therapy patients where the cancers are typically clearly observable on ADC images but not well delineated on T2 weighted images (figure 37, 38). It is important to note that while MRSI has demonstrated a high specificity, the DTI offers much higher spatial resolution in characterization of cancer (figure 39) and thus a combined approach may be clinically beneficial to provide post-treatment follow-up in prostate cancer patients.

Chapter 7: T2 mapping of the prostate

The normal prostate peripheral zone demonstrates long transverse relaxation times (T2) due to free motion of the water inside the prostatic ducts. The reduced signal intensity in region of prostate cancer or other pathology observed in T2-weighted FSE anatomical MRI is primarily due to the reduction of transverse relaxation time resulting from the loss of ductal volume. By quantitatively measuring T2 relaxation time of the prostate gland, the change of the ductal morphology due to pathological processes may be better understood, and it may also increase the specificity of MR for prostate cancer. T2 mapping can be accomplished by acquiring T2 weighted anatomical images at various echo time then fitting the signal intensity to calculate T2 values (figure 11). Conventional single echo spin echo (SE) sequences suffer from different T1 weightings between echoes unless a long TR is used, which can be clinically unfeasible. Multi-echo spin echo sequences are less time consuming, but it is prone to error due to imperfection in RF pulses and lead to errors in T2-measurement [94]. A magnetization preparation sequence with spiral imaging has been developed to provide robust T2 relaxation measurement in vivo [95]. In this chapter, I describe the initial studies I conducted to apply this novel method to the study of prostate cancer for the first time.

A) Pulse sequence for accurate T2 mapping

The T2 preparation portion of the sequence (figure 40) is designed to store T2-weighted magnetization along Mz in a manner that is robust to presence of flow as well as B₀ and B₁ inhomogeneities [95, 96]. A 90°_x excitation is followed by a train of equally spaced

180°_y pulses utilizing an MLEV phase cycling scheme [56] to provide insensitivity to B1 inhomogeneities and mis-set transmit gain. A 90° tip-up pulse then returns the magnetization to the longitudinal axis. The length of the refocusing train determine amount of T2 weighting in the resultant image. Spoiler gradients are used after the tip-up and inversion pulses (figure 40) to dephase any remaining transverse magnetization before the imaging sequence.

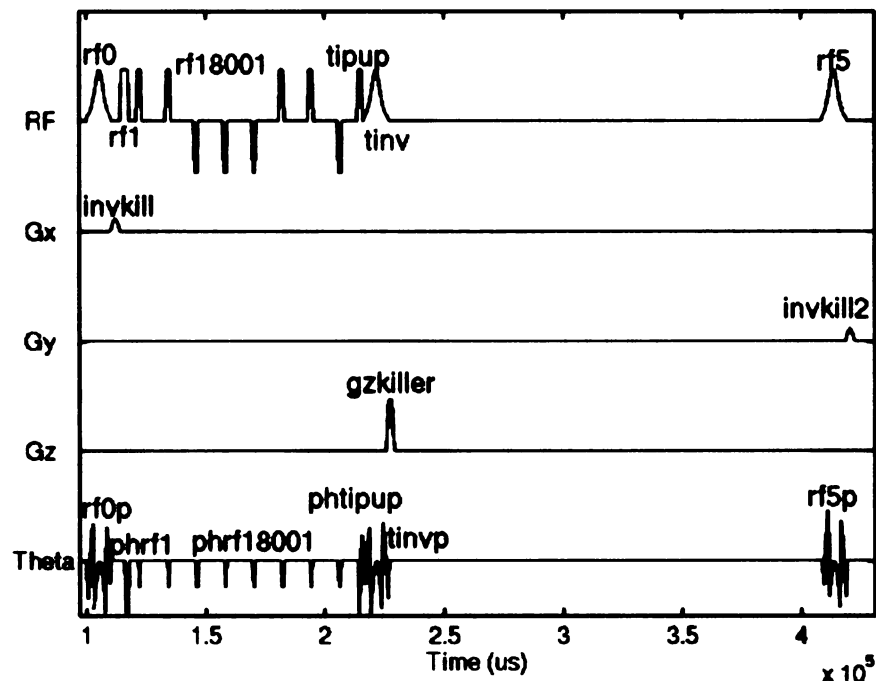


Figure 40. The T2 preparation portion of the pulse sequence. rf1 is the initial 90° excitation pulse, followed by a train of composite 180° pulses and a -270° ‘tip-up’ pulse that returns the T2-weighted magnetization to M_z . All the pulses in the T2 preparation portion are non-selective. Imaging sequence (not shown) is added after the tipup pulse to provide localization and to produce the desire image. The sequence is preceded and followed by an inversion pulse pair for rotation of magnetization into and out of the transverse plane to spoiled any residual magnetization.

The imaging acquisition includes a spectral-spatial pulse for slice selective excitation followed by 2D multi-slice spiral readout (figure 41). A RF cycling scheme was used to

mitigate the effects of T1 recovery between T2 preparation and the spiral readout. A

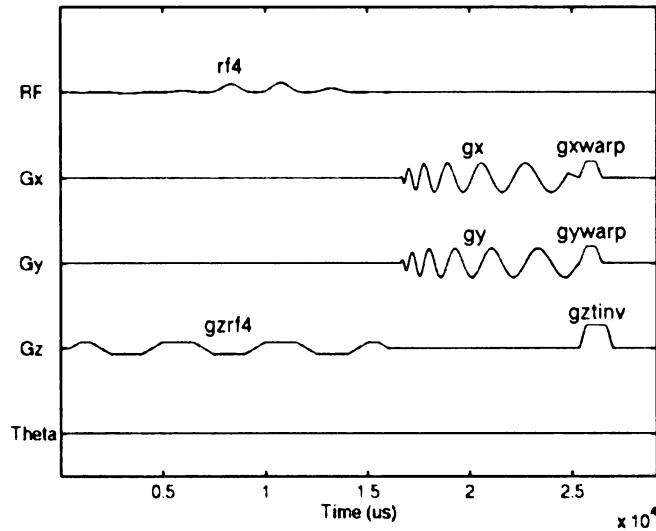


Figure 41. The spectral-spatial pulse (shown as rf4) and the 2D spiral readout implemented after the T2-preparation sequence.

chemical shift-selective saturation (CHESS) pulse was used to guarantee equal T1 recovery across all echoes acquired. A quantitative map of T2 relaxation time can be calculated once a sufficient number of data sets at appropriate echo times have been acquired.

B) Characterization of prostate cancer with T2 mapping

a. MRI/MRSI/DTI/T2-mapping protocol

All studies were performed on a GE 3T scanner (GE Healthcare, Waukesha, WI) using body coil for excitation and a Medrad inflatable endorectal coil (Medrad, Pittsburgh, PA) filled with Flutech_T14TM (F2 Chemicals, UK) in conjunction with a pelvic phase array coil for signal reception. Flutech_T14 is a fully fluorinated, colorless, odorless, non-toxic fluid with a magnetic permeability similar to tissue and thus is an ideal substitute for air to inflate the endorectal coil. 3T MRI and MRSI protocols have been described previously in Chapter 4. The MRI consisted of sagittal localizer, high-resolution T2-weighted FSE oblique axial and coronal images, and T1-weighted SE axial images.

MRSI data was acquired with an MLEV-PRESS sequence that allowed the acquisition of completely upright citrate resonance at TE of 85ms with a 0.157cc nominal spatial resolution. A DTI sequence based on EPI with 6 diffusion gradient directions was used. Oblique axial DTI-EPI images were acquired in 2.5 minutes with a FOV = 24 cm, 256 x 128 matrix, 4mm thick slices, and b-value of 600, with 8-10 slices typically to cover the prostate. A magnetization prepared sequence utilized non-selective composite 180 pulses and MLEV phase cycling followed by multi-slice spiral acquisition as described above was used for T2 quantification. Images at six different echo times were acquired (TE = 6, 25, 43, 81, 156, and 305 ms) with FOV = 24 cm, 128 x 128 effective matrix, TR = 2s, 4mm thick slices, at identical slice location as the DTI acquisition. Total acquisition time for all six sets of images was 4.5 minutes. Custom developed software was used for the processing of MRSI data, calculation of DTI parameters, and mono-exponential fitting of the six echo times data for calculation of quantitative maps of T2 relaxivity. Regions of prostate cancer were identified by concordance between biopsy results, T2-weighted MRI abnormality and elevated choline/reduced citrate on MRSI. Regions of benign prostatic tissue were identified by normal appearing prostatic tissue on T2-weighted MRI and normal prostatic metabolism (high level of citrate and low level of choline).

b. Results

Artifact free, high quality T2 and diffusivity maps were obtained from ten prostate cancer patient MRI/MRSI exams (figure 42). Reduced T2 and directionally invariant average diffusivity $\langle D \rangle$, as well as reduced citrate and elevated choline, were observed in regions of biopsy-proven prostate cancer as compared to regions of healthy prostate peripheral

zone (figure 42). The mean T2 value in region of prostate cancer for all ten patients was 79.8 ± 14.0 ms and the mean T2 value in region of normal prostatic tissue for all ten patients was 131 ± 30.1 ms. The difference in T2 value between regions of prostate cancer and normal prostatic tissue was significant ($p = 0.0001$). The mean $\langle D \rangle$ was 1.35

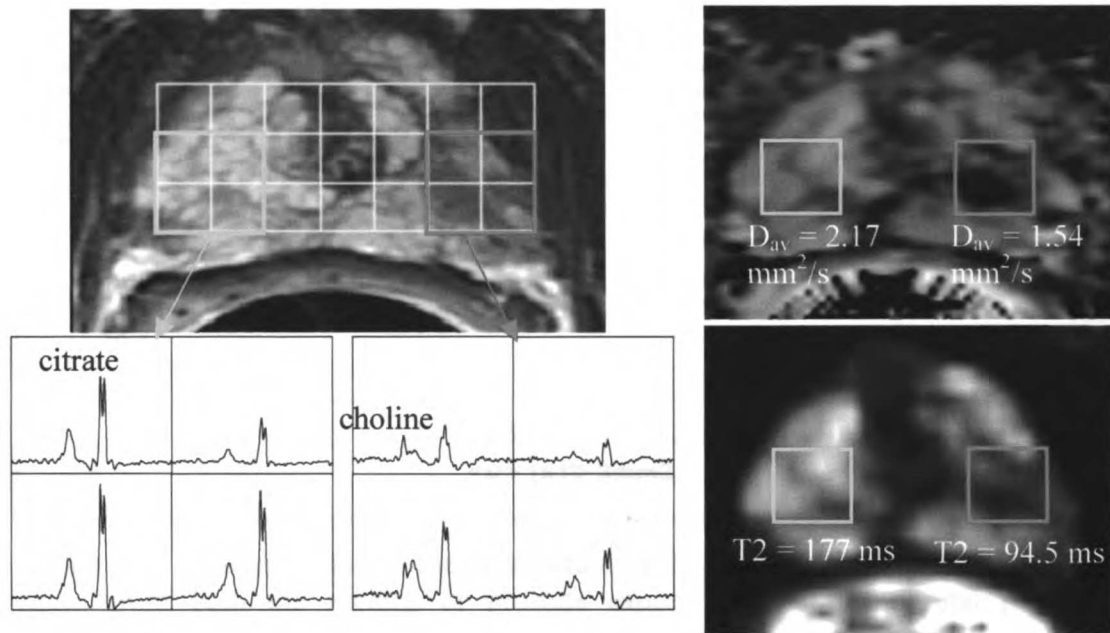


Figure 42. Sixty-one year old prostate cancer patient with biopsy proven cancer (G3+3, Left lobe). High-resolution T2-weighted FSE images (upper left) and MRSI (lower left) showed decrease signal intensity in the T2-weighted image and elevated choline and reduced citrate in region of prostate cancer. $\langle D \rangle$ maps (upper right) and T2 maps (lower right) also demonstrated decreased $\langle D \rangle$ (Cancer: .154 mm²/s vs Healthy: 2.17 mm²/s) and T2 (Cancer: 94.5 ms vs Healthy: 177 ms) relaxation time in region of cancer compared to region of healthy prostate peripheral zone.

$\pm 0.23 \times 10^3$ mm²/s in the regions of prostate cancer and $1.94 \pm 0.23 \times 10^{-3}$ mm²/s in regions of normal prostatic tissue, and the difference in $\langle D \rangle$ between cancer and normal regions was significant ($p = 0.00002$). The CC/C ratio was also significantly different ($p = 0.02$) between the regions of prostate cancer (1.6) and normal tissue (0.6).

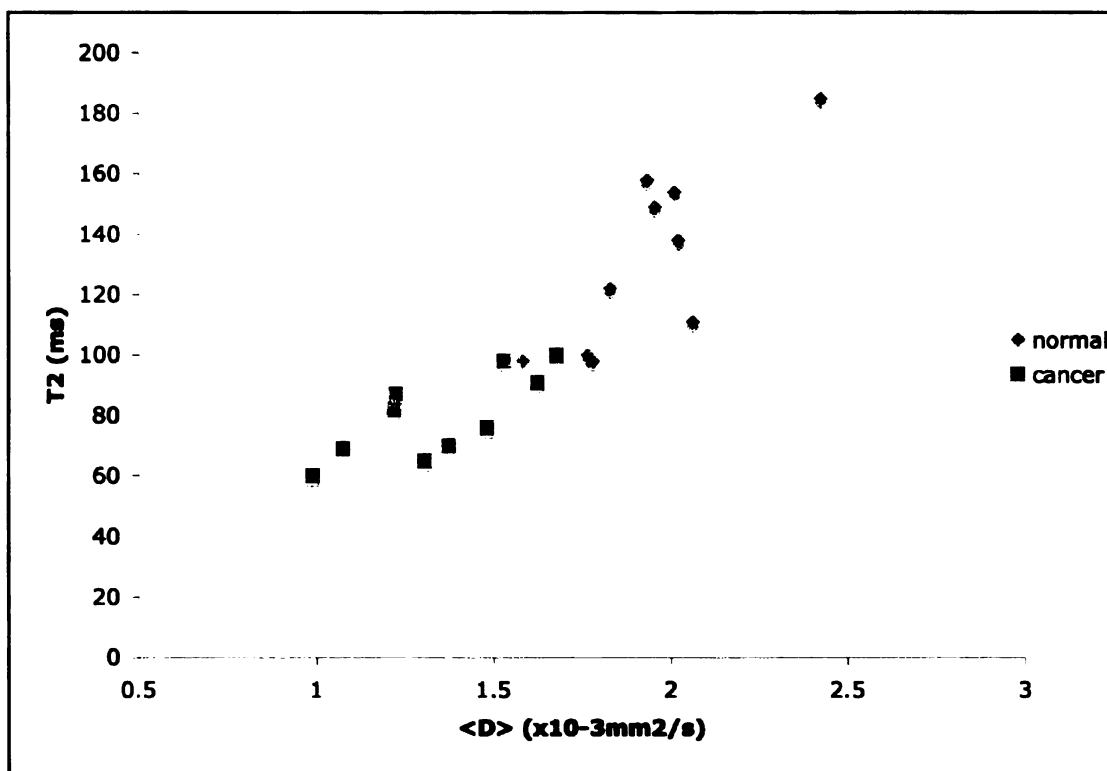


Figure 43. Scatterplot shows the distribution of the $\langle D \rangle$ values and T2 relaxation times from both the regions of prostate cancer and regions normal prostatic peripheral zone. A significant correlation was observed between $\langle D \rangle$ and T2 relaxation in the prostate.

c. Discussions

Acquisition of artifact free, multiple T2-weighted images for T2 mapping required considerable amount of time since relative long TR needed to reduced T1-weighting. Imaging artifacts for EPI based imaging sequence in area of high magnetic susceptibility are particularly undesirable for multi-parametric imaging. By filling the inflatable endorectal coil with a susceptibility matched fluid and utilizing a parallel imaging DTI-EPI sequence and a T2-prepared sequence with fast multi-slice spiral readout, it was

demonstrated that artifact free DTI data and high quality T2 maps can be acquired in the prostate at 3T in seven minutes.

The T2 values obtained in both normal prostatic peripheral zone and prostate cancer in this study were similar to that observed in prior study at 1.5T [82]. It has also been shown at 1.5T by our study (chapter 6) and others [6, 82] that significantly lower $\langle D \rangle$ can be observed in regions of prostate cancer compared to normal prostatic peripheral zone. In this study, the differences in both T2 and $\langle D \rangle$ between prostate cancer and normal prostatic peripheral zone were observed at 3T in the same patients for the first time. In addition, this study also demonstrated for the first time a significant correlation between T2 and $\langle D \rangle$ in both normal and cancerous prostate tissue (figure 43). Based on this correlation, it appears that T2 relaxation time and $\langle D \rangle$ offered similar information related to the presence of the ductal morphology. However, T2 relaxation time and $\langle D \rangle$ may offer different information depending on the differences in micro-structure and water environment. With the small b-values ($600 - 1000 \times 10^{-3} \text{ s/mm}^2$) used in prostate DTI studies, prostate DTI primarily investigates the changes in extracellular water diffusion. While T2 relaxation time may be sensitive to not only changes in extracellular space, but overall tissue environment. Thus with both T2 mapping and DTI, it may be possible to not only increase the specificity of anatomical T2-weighted MRI for localizing tumor, but also to differentiate prostate cancer of different type or grade (for example: solid tumor vs diffused disease). Further studies comparing DTI parameters and T2 to step-section histology from radical prostatectomy specimens will be necessary

to establish the utilities of these MR techniques for *in vivo* characterization of prostate cancer.

Chapter 8: Summary

With the availability of 3T whole body clinical MR scanners, the potential now exists for improving SNR, improving spatial resolution and/or reduction of scan-time using these higher field systems for MRI/MRSI exams as compared to those performed currently on 1.5T scanners. Prostate MRI/MRSI exams have become an important clinical tool for staging, treatment planning and monitoring of prostate cancer patients [36, 97-99]. Other MR modalities such as DTI, T2 mapping, and DCE have also been shown to provide useful information for *in vivo* characterization of prostate cancer [6, 7, 82]. This dissertation project sought to take advantage of the improvement possible at higher field (3T) and these new MR methods to develop a multi-parametric prostate MRI/MRSI exam to provide anatomic, metabolic, and morphological assessment of prostate cancer *in vivo*. Challenges such as the J-modulation changes for citrate resonance at higher field, more severe magnetic susceptibility induced magnetic field inhomogeneities, and increased chemical shift misregistration as compared to 1.5T make robust acquisition and analysis of prostate MRI/MRSI data challenging at 3T.

To reduce the effect of magnetic susceptibility, the use of a custom rigid endorectal coil or the prototype Medrad inflatable coil filled with Flutech_T14™ to obtain good quality high resolution prostate MRI was demonstrated. A MLEV-PRESS sequence incorporating phase-modulated frequency selective spectral-spatial refocusing pulses, a non-selective refocusing pulse train and VSS pulses was developed and tested for acquisition of high resolution (0.157 cc voxel resolution) prostate MRSI at 3T. The high

bandwidth SSRF pulses provided good spatial selection, reduction of chemical-shift misregistration, robust suppression of lipid and attenuated refocusing of water. The non-selective refocusing pulse train provided J-refocusing of the citrate resonance and allowed the acquisition of completely up-right citrate doublet of doublet at an echo time of 85 ms. In ten prostate cancer patients examined at both 3T and 1.5T, a 2-fold increase in SNR for prostate MRSI was demonstrated at 3T over 1.5T.

Another obstacle for MRI/MRSI exams at 3T is the prohibitively long acquisition time required to acquire large volume 3D spectral data sets using conventional phase-encoding in all three dimensions especially at the high spatial resolution possible at higher field. The increase in SAR and T1 relaxation time also can make the scan time required for MRSI even longer and prohibit the acquisition of other MR sequences. In this project, flyback echo-planar readout trajectories were designed and implemented in the MLEV-PRESS sequence to provide up to 16-fold reduction in scan time, robust data acquisition and reconstruction of prostate MRSI data. High-quality MRSI data acquired in 8.5 minutes were demonstrated in nine prostate cancer patients using the modified pulse sequence.

Diffusion tensor imaging and T2 mapping can provide morphological information based on the movement of water molecules and their tissue environment. Robust acquisition of DTI data and T2 mapping in the body has been difficult to achieve due to motion, magnetic susceptibility and obtaining accurate T2-weighting. DTI-SSFSE studies were included in this project to develop a method for the acquisition of non-distorted DTI

parameter maps. Studies with this technique demonstrated significant differences in DTI parameters between regions of prostate cancer and normal prostate peripheral zone. Initial T2 mapping study at 3T was performed on ten prostate cancer patients using a magnetization prepared sequence followed by 2D multi-slice spiral readout. DTI-EPI acquisitions utilizing parallel imaging technique (SENSE) were also included in this dissertation project. Both T2 maps and DTI parameter maps showed significant differences between regions of prostate cancer and normal prostatic tissues. A significant correlation was also observed between T2 and $\langle D \rangle$ in these patients.

With the developments presented in this work, a prostate MRI/MRSI/DTI/T2-mapping exam became feasible at 3T. The initial data presented indicates a dramatic improvement for prostate MR exams at 3T as compared to those currently routinely done at 1.5T. The multi-parametric approach of using different MR modalities during the same exam to acquire different and unique information to characterize prostate cancer may also help to increase the usefulness and significance of this exam for the clinical management of prostate cancer.

References:

1. http://seer.cancer.gov/csr/1975_2002/results_single/sect_01_table.01.pdf, N.C.I.
2. Han, M., et al., *Era specific biochemical recurrence-free survival following radical prostatectomy for clinically localized prostate cancer*. J Urol, 2001. **166**(2): p. 416-9.
3. McNeal, J.E., et al., *Patterns of Progression in Prostate Cancer*. Lancet, 1986. **1**: p. 60-63.
4. Stamey, T.A., *Cancer of the Prostate: An analysis of some important contributions and dilemmas*. Mono. Urol., 1982. **3**: p. 67-94.
5. Kurhanewicz, J., et al., *Magnetic resonance imaging and spectroscopic imaging: Improved patient selection and potential for metabolic intermediate endpoints in prostate cancer chemoprevention trials*. Urology, 2001. **57**(4 Suppl 1): p. 124-8.
6. Issa, B., *In vivo measurement of the apparent diffusion coefficient in normal and malignant prostatic tissues using echo-planar imaging*. J Magn Reson Imaging, 2002. **16**(2): p. 196-200.
7. Noworolski, S.M., et al., *Dynamic Contrast-Enhanced MRI in Normal and Abnormal Prostate Tissues as Defined by Biopsy, MRI, and 3D MRSI*. Magn Reson Med, 2005(53): p. 249-255.
8. www.rit.edu/~japfaa/prostate.jpg.
9. Gleason, D., *Histologic Grading of Prostate Cancer: a Perspective*. Human Pathology, 1992. **23**: p. 273-279.
10. Gleason, D., *The Veteran's Administration Cooperative Urologic Research Group: histologic grading and clinical staging of prostatic carcinoma*, in *Urologic Pathology: The Prostate*, M. Tannenbaum, Editor. 1977, Lea and Febiger: Philadelphia. p. 171-198.
11. Hennig, J., Nauerth, A., and Friedburg, H. , *RARE imaging: A fast imaging method for clinical MR*. Mag Res Med, 1986. **3**: p. 823-833.
12. Hricak, H., et al., *Carcinoma of the prostate gland: MR imaging with pelvic phased-array coils versus integrated endorectal--pelvic phased-array coils*. Radiology, 1994. **193**(3): p. 703-9.
13. Yu, K.K. and H. Hricak, *Imaging prostate cancer*. Radiol Clin North Am, 2000. **38**(1): p. 59-85, viii.
14. Yu, K.K., et al., *Prostate cancer: prediction of extracapsular extension with endorectal MR imaging and three-dimensional proton MR spectroscopic imaging*. Radiology, 1999. **213**(2): p. 481-8.
15. Star, L.J., et al., *Improved solvent suppression and increased spatial excitation bandwidths for three-dimensional PRESS CSI using phase-compensating spectral/spatial spin-echo pulses*. J Magn Reson Imaging, 1997. **7**(4): p. 745-57.
16. Schricker, A.A., Pauly, J M, Kurhanewicz, J, Swanson, M G, and Vigneron, D B, *Dualband spectral-spatial RF pulses for prostate MR spectroscopic imaging*. Magnetic Resonance in Medicine, 2001. **46**(6): p. 1079-1087.
17. Costello, L.C. and R.B. Franklin, *Concepts of citrate production and secretion by prostate. 1. Metabolic relationships*. Prostate, 1991. **18**(1): p. 25-46.

18. Costello, L.C. and R.B. Franklin, *Novel role of zinc in the regulation of prostate citrate metabolism and its implications in prostate cancer*. *Prostate*, 1998. **35**(4): p. 285-96.
19. Yu, K.K., et al., *Detection of extracapsular extension of prostate carcinoma with endorectal and phased-array coil MR imaging: multivariate feature analysis*. *Radiology*, 1997. **202**(3): p. 697-702.
20. Scheidler, J., et al., *Prostate cancer: localization with three-dimensional proton MR spectroscopic imaging--clinicopathologic study*. *Radiology*, 1999. **213**(2): p. 473-80.
21. Kurhanewicz, J., et al., *The prostate: MR imaging and spectroscopy. Present and future*. *Radiol Clin North Am*, 2000. **38**(1): p. 115-38, viii-ix.
22. Yu, K.K., et al., *Detection of extracapsular extension of prostate carcinoma by endorectal/phased array coil MR imaging: multivariate analysis*. *Radiology*, 1997. **202**: p. 697-702.
23. Coakley, F.V., et al., *Prostate cancer tumor volume: measurement with endorectal MR and MR spectroscopic imaging*. *Radiology*, 2002. **223**(1): p. 91-7.
24. Scheidler, J., et al., *3D ¹H-MR Spectroscopic Imaging in Localizing Prostate Cancer: Clinico-Pathologic Study*. *Radiology*, 1999. **213**: p. 473-480.
25. Coakley, F.V., et al., *Endorectal MR Imaging and MR Spectroscopic Imaging for Locally Recurrent Prostate Cancer after External Beam Radiation Therapy: Preliminary Experience*. *Radiology*, 2004.
26. Mueller-Lisse, U.G., et al., *Localized prostate cancer: Effect of hormone deprivation therapy measured by using combined three-dimensional H-1 MR spectroscopy and MR imaging: Clinicopathologic case-controlled study*. *Radiology*, 2001. **221**(2): p. 380-390.
27. Coakley, F.V., et al., *Brachytherapy for prostate cancer: endorectal MR imaging of local treatment-related changes*. *Radiology*, 2001. **219**(3): p. 817-21.
28. Kurhanewicz, J., et al., *³¹P magnetic resonance spectroscopy after combined hyperthermia and radiation*. *Curr Eye Res*, 1994. **13**(2): p. 151-6.
29. Mueller-Lisse, U.G., et al., *Time-dependent effects of hormone-deprivation therapy on prostate metabolism as detected by combined magnetic resonance imaging and 3D magnetic resonance spectroscopic imaging*. *Magnetic Resonance in Medicine*, 2001. **46**(1): p. 49-57.
30. Alsop, D.C., *Phase insensitive preparation of single-shot RARE: application to diffusion imaging in humans*. *Magn Reson Med*, 1997. **38**(4): p. 527-33.
31. Sodickson, D.K. and W.J. Manning, *Simultaneous acquisition of spatial harmonics (SMASH): fast imaging with radiofrequency coil arrays*. *Magn Reson Med*, 1997. **38**(4): p. 591-603.
32. deSouza, N.M., et al., *A solid reusable endorectal receiver coil for magnetic resonance imaging of the prostate: design, use, and comparison with an inflatable endorectal coil*. *J Magn Reson Imaging*, 1996. **6**(5): p. 801-4.
33. Kurhanewicz, J., et al., *³¹P spectroscopy of the human prostate gland in vivo using a transrectal probe*. *Magn Reson Med*, 1991. **22**(2): p. 404-13.
34. Ardenkjaer-Larsen, J.H., et al., *Increase in signal-to-noise ratio of > 10,000 times in liquid-state NMR*. *Proc Natl Acad Sci U S A*, 2003. **100**(18): p. 10158-63.

35. Kurhanewicz, J., et al., *Three-dimensional H-1 MR spectroscopic imaging of the in situ human prostate with high (0.24-0.7-cm³) spatial resolution*. Radiology, 1996. **198**(3): p. 795-805.
36. Kurhanewicz, J., et al., *Combined magnetic resonance imaging and spectroscopic imaging approach to molecular imaging of prostate cancer*. J Magn Reson Imaging, 2002. **16**(4): p. 451-63.
37. Vigneron, D., et al. *High resolution 3D MR spectroscopic imaging and J-resolved MRS of the prostate at 3 Tesla*. in ISMRM. 2004.
38. Kaji, Y., et al. *MR Imaging and MR Spectroscopy of Prostate at 3 Tesla*. in ISMRM. 2003.
39. Kuroda, K., et al. *MR Observation of Prostate Metabolites at 3 Tesla*. in ISMRM. 2002.
40. Trabesinger, A.H., et al., *Optimizing PRESS localized citrate detection at 3 Tesla*. Magn Reson Med, 2005. **54**(1): p. 51-8.
41. Kim, D.-H.M., D. Xing, L. Speilman, D., *In vivo prostatesmagnetic resonance spectroscopic imaging using two-dimensional J-resolved PRESS at 3T*. Mag Res Med, 2005. **53**: p. 1177-1182.
42. Kim, H.B., DL. Peterson, DM. Duensing, GR. Caserta, J. Fitzsimmons, J. Blackband, SJ., *In vivo prostate magnetic resonance imaging and magnetic Resonance spectroscopy at 3 Tesla using a transceive pelvic phased array coil: preliminary Results*. Invest Radiol, 2003(38): p. 443-451.
43. Futterer, J.S., TW. Huisman, HJ. Klomp, DW. van Dorsten, FA. Hulsbergen-van de Kaa, CA. Witjes, JA. Heerschap, A. Barentsz, JO. , *Initial experience of 3 tesla endorectal coil magnetic resonance imaging and 1H-spectroscopic imaging of the prostate*. . Invest Radiol, 2004. **39**: p. 671-680.
44. Scheenen, T.W., et al., *Optimal timing for in vivo 1H-MR spectroscopic imaging of the human prostate at 3T*. Magn Reson Med, 2005. **53**(6): p. 1268-74.
45. van der Graaf, M., G.J. Jager, and A. Heerschap, *Removal of the outer lines of the citrate multiplet in proton magnetic resonance spectra of the prostatic gland by accurate timing of a point-resolved spectroscopy pulse sequence*. Magma, 1997. **5**(1): p. 65-9.
46. Wilman, A.A., PS., *The response of the strongly coupled AB system of citrate to typical 1H MRS localization sequences*. J Magn Reson B 1995. **107**(1): p. 25-33.
47. BaX, A., *Two dimensional nuclear magnetic resonance in liquids*. . 1982, Boston: Reidel.
48. Allerhand, A., *Analysis of Carr-Purcell spin-echo NMR experiments on multiple-spin systems. I. The effect of homonuclear coupling*. J Chem Phys, 1966. **44**: p. 1-9.
49. Hennig, J., T. Thiel, and O. Speck, *Imporved sensitiviey to overlapping multiplet signals in in vivo proton spectroscopy using a multiecho volume selective (CPRESS) experiment*. . Mag Res Med, 1997. **37**: p. 816-820.
50. Cunningham, C.H., et al. *Sequence design incorporating the LASER technique for prostate MRSI at high field*. . in ISMRM. 2004.
51. Van Der Graaf, M.a.H., A., *Effect of cation binding on the proton chemical shifts and the spin-spin coupling constant of citrate*. Journal of Magnetic Resonance, Series B, 1996. **112**: p. 58-62.

52. Pauly, J.M., et al., *Parameter Relations for the Shinnar-LeRoux RF Pulse Design Algorithm*. IEEE Transactions on Medical Imaging, 1991. **10**(1): p. 53-65.
53. Shinnar, M., *Reduced power selective excitation radio frequency pulses*. Magn Reson Med, 1994. **32**(5): p. 658-60.
54. Pickup, S. and X. Ding, *Pulses with fixed magnitude and variable phase response profiles*. Magn Reson Med, 1995. **33**(5): p. 648-55.
55. Pauly, J., D. Spielman, and A. Macovski, *Echo-planar spin-echo and inversion pulses*. Magn Reson Med, 1993. **29**(6): p. 776-82.
56. Levitt, M., *Composite pulse decoupling*. J Mag Reson, 1981. **43**: p. 502-507.
57. Coakley, F.V., A. Qayyum, and J. Kurhanewicz, *Magnetic resonance imaging and spectroscopic imaging of prostate cancer*. J Urol, 2003. **170**(6 Pt 2): p. S69-75; discussion S75-6.
58. Nelson, S., *Analysis of volume MRI and MR Spectroscopic imaging data for the evaluation of patients with brain tumors*. Mag Res Med, 2003. **46**(2): p. 228-239.
59. Nelson, S., *Multivoxel magnetic resonance spectroscopy of brain tumors*. Mol Cancer Ther, 2003. **2**(5): p. 497-507.
60. Marquardt, D., *An algorithm for least-squares estimation of nonlinear parameters*. J. Soc. Indust. Appl. Math., 1963. **11**: p. 431-441.
61. Press, W., et al., *Numerical Recipes*. 1998, New York: Cambridge University Press.
62. Hoult, D.I. and D. Phil, *Sensitivity and power deposition in a high-field imaging experiment*. J Magn Reson Imaging, 2000. **12**(1): p. 46-67.
63. Vaughan, J.T., et al., *7T vs. 4T: RF power, homogeneity, and signal-to-noise comparison in head images*. Magn Reson Med, 2001. **46**(1): p. 24-30.
64. Le Roux, P., et al., *Optimized outer volume suppression for single-shot fast spin-echo cardiac imaging*. J Magn Reson Imaging, 1998. **8**(5): p. 1022-32.
65. Pauly, J.M., et al., *A three-dimensional spin-echo or inversion pulse*. Magn Reson Med, 1993. **29**(1): p. 2-6.
66. Pauly, J.M., D.G. Nishimura, and A. Macovski, *A Linear Class of Large-Tip-Angle Selective Excitation Pulses*. J. Magn. Reson., 1989. **82**(May): p. 571-587.
67. Pauly, J.M., D.G. Nishimura, and A. Macovski, *A k-Space Analysis for Small Tip Excitation*. J. Magn. Reson., 1989. **81**(Jan.): p. 43-56.
68. Meyer, C.H., et al., *Simultaneous spatial and spectral selective excitation*. Magn Reson Med, 1990. **15**(2): p. 287-304.
69. Star-Lack, J., et al., *Improved solvent suppression and increased spatial excitation bandwidths for three-dimensional PRESS CSI using phase-compensating spectral/spatial spin-echo pulses*. J Magn Reson Imaging, 1997. **7**(4): p. 745-57.
70. Posse, S., et al., *High speed 1H spectroscopic imaging in human brain by echo planar spatial-spectral encoding*. Magn Reson Med, 1995. **33**(1): p. 34-40.
71. Webb, P., D. Spielman, and A. Macovski, *A fast spectroscopic imaging method using a blipped phase encode gradient*. Magn Reson Med, 1989. **12**(3): p. 306-15.
72. Mulkern, R.P., LP. , *Echo planar spectroscopic imaging*. Concept Magn Reson 2001. **13**: p. 213-237.
73. Adalsteinsson, E., et al., *Three-dimensional spectroscopic imaging with time-varying gradients*. Magn Reson Med, 1995. **33**(4): p. 461-6.

74. Jung, J.A., et al., *Prostate Depiction at Endorectal MR Spectroscopic Imaging: Investigation of a Standardized Evaluation System*. Radiology, 2004. **233**(3): p. 701-8.
75. Cheng, L.L., et al., *Non-destructive quantitation of spermine in human prostate tissue samples using HRMAS 1H NMR spectroscopy at 9.4 T*. FEBS Lett, 2001. **494**(1-2): p. 112-6.
76. Cunningham, C., et al., *Design of flyback echo-planar readout gradients for magnetic resonance spectroscopic imaging*. Mag Res Med, 2005. **54**: p. 1286-1289.
77. Kim, D., et al., *Importance of k-space trajectory in echo-planar myocardial tagging at rest and during dobutamine stress*. Mag Res Med, 2003. **50**(4): p. 813-20.
78. Chen, A., et al., *High-Resolution 3D MR Spectroscopic Imaging of the Prostate at 3 Tesla with the MLEV-PRESS sequence*. MRI, 2006(In press).
79. Pierpaoli, C. and P.J. Basser, *Toward a quantitative assessment of diffusion anisotropy*. Magn Reson Med, 1996. **36**(6): p. 893-906.
80. Oh, J., et al., *Survival analysis in patients with glioblastoma multiforme: predictive value of choline-to-N-acetylaspartate index, apparent diffusion coefficient, and relative cerebral blood volume*. J Magn Reson Imaging, 2004. **19**(5): p. 546-54.
81. Basser, P.J. and C. Pierpaoli, *A simplified method to measure the diffusion tensor from seven MR images*. Magn Reson Med, 1998. **39**(6): p. 928-34.
82. Gibbs, P., et al., *Comparison of quantitative T2 mapping and diffusion-weighted imaging in the normal and pathologic prostate*. Magn Reson Med, 2001. **46**(6): p. 1054-8.
83. Chenevert, T.L., et al., *Diffusion magnetic resonance imaging: an early surrogate marker of therapeutic efficacy in brain tumors*. J. Natl. Cancer Inst., 2000. **92**(92): p. 2029-2036.
84. Kremser, C., et al., *Preliminary results on the influence of chemoradiation on apparent diffusion coefficients of primary rectal carcinoma measured by magnetic resonance imaging*. Strahlenther. Onkol., 2003. **179**: p. 641-649.
85. Mardor, Y., et al., *Monitoring response to convection-enhanced taxol delivery in brain tumor patients using diffusion-weighted magnetic resonance imaging*. Cancer Res, 2001. **61**: p. 4971-4973.
86. Mardor, Y., et al., *Early detection of response to radiation therapy in patients with brain malignancies using conventional and high b-value diffusion-weighted magnetic resonance imaging*. J. Clininical Oncol., 2003. **21**: p. 1094-1100.
87. Xu, D., et al., *Diffusion Tensor Imaging of the Brain and Cervical Spine using a Single-Shot Fast Spin-Echo Sequence*. Magn Reson Imag, 2004. **22**: p. 751-759.
88. Vigneron, D., et al. *Diffusion Tensor Imaging of the Prostate using Single-Shot Fast Spin Echo MRI*. in Proc. Intl. Soc. Mag. Reson. Med. 2002. Honolulu.
89. Bastin, M.E. and P. Le Roux, *On the application of a non-CPMG single-shot fast spin-echo sequence to diffusion tensor MRI of the human brain*. Magn Reson Med, 2002. **48**(1): p. 6-14.
90. Pruessmann, K.P., et al., *SENSE: sensitivity encoding for fast MRI*. Magn Reson Med, 1999. **42**(5): p. 952-62.

91. Ra, J.B. and C.Y. Rim, *Fast imaging using subencoding data sets from multiple detectors*. Magn Reson Med, 1993. **30**(1): p. 142-5.
92. Carlson, J.W. and T. Minemura, *Imaging time reduction through multiple receiver coil data acquisition and image reconstruction*. Magn Reson Med, 1993. **29**(5): p. 681-7.
93. Brawn, P., *Histologic Features of Metastatic Prostate Cancer*. Human Pathology, 1992. **23**: p. 267-262.
94. Poon, C.S. and R.M. Henkelman, *Practical T2 quantitation for clinical applications*. J Magn Reson Imaging, 1992. **2**(5): p. 541-53.
95. Foltz, W.D., et al., *Optimized spiral imaging for measurement of myocardial T2 relaxation*. Magn Reson Med, 2003. **49**(6): p. 1089-97.
96. Brittain, J.H., et al., *Coronary angiography with magnetization-prepared T2 contrast*. Magn Reson Med, 1995. **33**(5): p. 689-96.
97. Hricak, H., et al., *The role of preoperative endorectal magnetic resonance imaging in the decision regarding whether to preserve or resect neurovascular bundles during radical retropubic prostatectomy*. Cancer, 2004. **100**(12): p. 2655-63.
98. Mueller-Lisse, U.G., et al., " *Hormone Ablation of Localized Prostate Cancer: Time-Dependent Therapy Effects on Prostate Metabolism Detected by 3D 1H MR Spectroscopy*". Magnetic Resonance In Medicine, 2000: p. In Press.
99. Coakley, F.V., et al., *Endorectal MR Imaging and MR Spectroscopic Imaging for Locally Recurrent Prostate Cancer after External Beam Radiation Therapy: Preliminary Experience*. Radiology, 2004. **233**(2): p. 441-8.

Handwritten text, likely bleed-through from the reverse side of the page. The text is extremely faint and illegible due to the quality of the scan. It appears to be a list or series of entries, possibly containing names and dates, but the characters are too light to transcribe accurately.

7537296



3 1378 00753 7296

For reference

Not to be taken
from the room.

